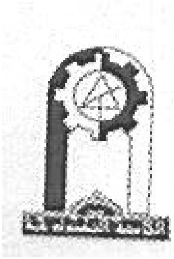

جمهورية العراق
وزارة التعليم العالي والبحث العلمي
الجامعة التكنولوجية
قسم هندسة الليزر والبصريات الألكترونية

تحليل عمل ليزر الآبار الكمية في ليزرات الحالة الصلبة المضخة بالليزر الثنائي

أطروحة مقدمة الى قسم هندسة الليزر والبصريات الألكترونية-الجامعة التكنولوجية
وهي جزء من متطلبات نيل درجة الدكتوراة في فلسفة هندسة الليزر

من قبل

هدى محمود حكمت

(ماجستير علوم 2003)

أشراف

أ.م.د. عدوية جمعة حيدر

1428هـ **2008م**

Abstract:

The Quantum well laser structure has become the leading candidate for applications in optoelectronics and diode pumping because of its potential for high speed low threshold and less pronounced temperature sensitivity of the laser threshold current.

In this work, a mathematical model was built to analyze the structure, performance of quantum well (QW) lasers, which can be hired in pumping solid-state disc used in solid-state lasers having the highest optical efficiency, peak output power, and ultra high beam optical quality. The application of such treatment is industrial which requires high-quality beams.

In this study, a theoretical structure for bulk and Quantum well laser of type GaAs/AlGaAs has been reported. For these structures a typical feature of the double heterostructure had been chosen in terms of Al mole fraction.

Results show that for bulk diode laser the bandwidth of the emitted radiation will be reduced when operating at a temperature of 200°K instead of 300°K. The differential gain is increased by a factor of approximately 70% when the temperature is reduced, and the transparency density at temperatures of 300°K and 200°K are found to be equals to $0.03*10^{19}cm^{-3}$ and $0.5*10^{17}cm^{-3}$, respectively, which means higher relaxation oscillation resonance frequency.

With different stripe widths of (20, 40, 60, 80, 100)µm and two different reflectivities (0.32, 0.8), the optical output power was found to be (78, 65, 58, 47, 39)mW, and (44, 42, 40.5, 38, 37)mW, respectively at room temperature, while at an operating temperature of 200 ^{o}K the optical output power was found to be (82, 73, 68, 62, 55)mW, and (45, 44, 43, 41.5, 40)mW, respectively.

At stripe width of 20µm and operating Temperature of 200°K, the lower threshold current equals to 6.5 mA, 3.6 mA at facet reflectivity of 0.32, and 0.08, respectively, and the optimum value for the stripe width, active region thickness and the facet reflectivity were found to be 20 µm, 0.01 µm , and 0.8, respectively.

Solution of the Schrödinger equation was solved numerically using the linear shooting method, and the Matlab package had performed all the numerical calculations.

For QW laser results shows that using the QW thickness (50, 75, 150, 200 A^o) there is a critical value for increasing the injected carrier density results in an increase in the

radiative current density , beyond this value the radiative current density will be degraded, and the transparency density increases with reducing the QW thickness.

Higher gain values can be obtained for lower injected carrier density, by increasing the QW thickness this will result in an increase in the spontaneous emission rate, also the transverse electric (TE) modes were found to exhibit lower lasing threshold, and higher gain profile for lower QW thickness.

In experimental work as an application 808 nm (2Watt) bulk and 810 nm (1Watt) QW laser used as pumping sources to a $Nd:YVO_4$ Disk crystal with dimensions of (4*5*1 mm) with an output coupler with 90% reflectivity, and radius of curvature (ROC=400mm). Two pumping schemes direct face pumping and V-shape with internal and external triggering were implemented.

For the bulk diode laser (internal triggering) the repetition rate (PRF) used was 1.3kHz. For direct face pumping the maximum emitted peak power was found to be nearly (100 mW, 82 mW, and 66 mW) for resonator lengths of L (10cm, 13.5cm, and 17.5cm) respectively, while the threshold power was found to be $P_{th,}$= 41mW. When using external triggering, the repetition rate can be lowered to reach 3Hz, using L=10cm the emitted peak power obtained was 300 mW.

The second pumping scheme was the V-shape face pumping. A comparison was made between the bulk and the QW laser when used as pumping sources, in CW mode the output power obtained for the bulk diode laser was 29 mW, and using the QW diode laser the maximum output power obtained was 58 mW.

In pulsed mode, using internally triggered bulk diode laser with PRF=1.3kHz, the maximum emitted peak power was found to be 40 mW, with a resonator length L=13cm, while for external triggering with PRF=11Hz, the maximum output peak power was found to be 155 mW, using L=13cm.

Acknowledgement:

I am pleased to have this opportunity to acknowledge the assistance and support of the many people who contributed to the completion of this work.

First I would like to express my gratitude to my supervisor ***Dr.Adawiya J. Haider***, "thanks you for the suggestion of the idea of this work, thanks for your support and patience".

Thanks to ***Dr.Mohammed H. Ali***, the Head of the department of laser and optoelectronics engineering, and to ***Dr.Ali. H. Al-Hamadani***, the Head of Optoelectronics Engineering Department.

Special thanks to Institute of Laser for Postgraduate Studies, University of Baghdad, especially ***Dr. Mohammed K. Al-Ani***, ***Dr. Sheelan Kh. Tawfiq***, ***Dr. Zainab F. Mahdi,*** for their valuable support in the accomplishment of the experimental study.

Also I can't forget the kind help and support of the following persons, ***Dr. Anwar A. Al-Dergasally,*** the Head of the Laser and Optoelectronics Engineering Department, Al-Nahrain University, ***Dr.Riyadh A. Mirza***, and ***Mr.Auday A.Hummadi***.

Special thanks to ***My Father, Brother, and Sisters*** for their encouragement, support, and being my inspiration.

Huda

Laser diode driver:

1.1 Front Panel display and control knobs description:

Fig.(1) shows the front panel with the LCD (Liquid Crystal Display) and the control knobs and potentiometers.

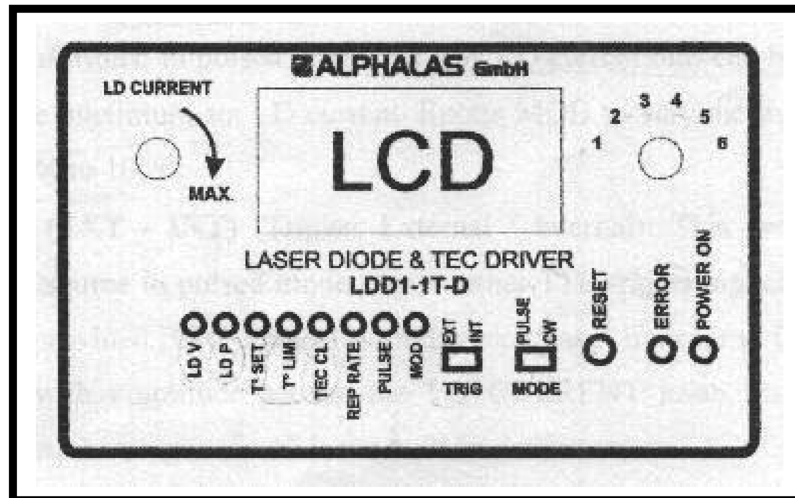

Fig.(1) the laser diode driver "control panel", [50].

By rotating the multiturn potentiometers, the following parameters can be adjusted:

1. LD CL (Laser diode current Limit): used to adjust the desired value of the current limit.
2. LD Current*(Laser Diode Current): used to adjust the desired value of the operating current.
3. LD V (Laser Diode Voltage): used to adjust the desired value of the operating voltage.
4. LD P (Laser Diode Power): Shall regulate the laser diode power if a signal feedback is provided from a photo diode.
5. T^{o} SET*(Temperature Set): used to adjust the desired temperature of the laser diode in the range 0°- 50°C. There are LD safe limits: lower limit 12°C, factory adjusted, and an upper temperature limit (user adjustable).
6. T^{o} LIM (temperature limit): user- adjustable limit to protect the laser diode from overheating. Factory adjusted at 35°.
7. TEC CL*(TEC Current Limit): the maximum current of the TEC (Peltier) module can be set to the desired value in the range 0-6 A.
8. REP RATE*(Repetition Rate): in the pulsed mode will adjust the frequency of the built-in signal generator in the range 1 kHz-20 kHz.

9. Pulse (Pulse Duration): in the pulsed mode, the pulse duration can be adjusted in the range 10μs-250μs.
10. TRIG (EXT-INT) (Trigger External / Internal): the trigger source in pulsed mode is selected by this switch. An external TTL rigger signal can be applied to the provided BNC connector on the back panel in order to initiate a current pulse with amplitude set by the LD current knob. In INT (internal) position, the trigger source is the built-in generator.
11. MODE (PULSE-CW). The mode of operation is selected by this switch, pulsed or CW.
12. RESET: this switch will resume the laser diode operation after the error reason is removed.
13. MOD (Modulation): in pulsed mode, the CW LD current bias can be adjusted from 0 to the maximum set LD current, so that the modulation depth is varied from 0% to 100%.
14. Display Switch Selection: (position 1-6): Selects the value to be displayed as follows:
    1. LD Current (Ampere)
    2. Frequency (repetition rate), kHz
    3. TEC Current (Ampere). Shows the actual TEC current. The value is between 0 and TEC current limit and depends on the momentary needed cooling power.
    4. TEC CURRENT LIMIT (Ampere). Shows the set TEC current limit. The value can be adjusted between 0 and 6 A.
    5. T^o MEASURED (^oC): Displays the actual temperature measured by the thermistor.
    6. T^o SET (^oC): Displays the temperature set by the potentiometer T^o SET.

The LCD shows the adjusted parameters of the control potentiometers marked by (*)

1.2 Back Panel Description:

Fig.(2) shows the back side of LDD1-1T-D.

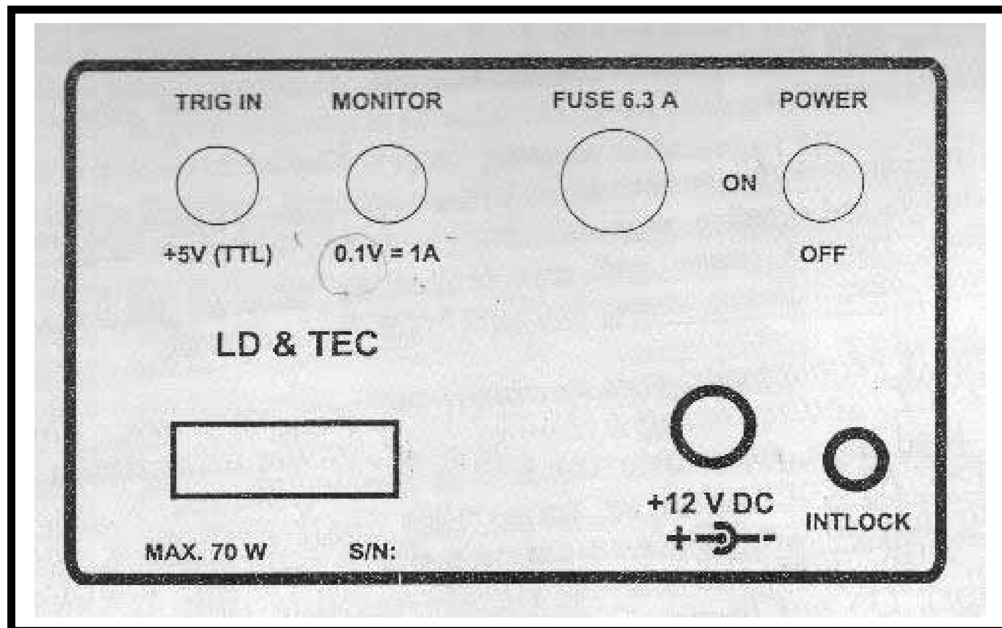

Fig.(2) the laser diode driver "back panel", [50].

The following connectors and controls are situated on the back panel:

1. +12 V DC is the plug- in for external power supply.
2. INTERLOCK is the plug- in for interlock.
3. LD & TEC is a sub-D15 connector for the laser diode, TEC module, photo diode feedback and thermistor.
4. TRIG IN: a BNC connector provides voltage signal proportional to the laser diode current with conversion factor: 0.1=1A.

The POWER switch turns the device ON and OFF. A replaceable FUSE 6.3 A is on the left hand side of the main power supply. For the bulk laser diode Table (1) illustrates the general specifications of the laser diode driver see Fig.(3), while The electrical and optical characteristics for the QW laser diode are illustrated in table (2) with the mechanical dimensions, see table (2).

Table (1) illustrates the general specifications of the laser diode driver

Parameter	***Value***
Laser diode driver	
Laser diode current limit LD CL	*0.1-6.0A*
Laser diode current (CW or Pulsed)	*0.1-6.0A*
Laser diode voltage Factory set at	*1.0-5.0V 4.0V*
CW bias in pulsed mode	*0 to LD Current*
Optical feedback	*Available*
Soft start	*Approx. 10 seconds*
TEC Driver	
TEC current	*0.0-5.0A*
TEC current limit	*0.0-5.0A*
TEC voltage	*1.0-8.0V*
Temp. stability	*0.1°C*
Thermistor	*NTC, 10kOhm*
Temperature	*5-50°C*
Temperature limit (lower)	*12°C*
Temperature limit (upper)	*50°C*
Frequency Generator	
Repetition rate	*1-20kHz standard*
Pulse width	*10-250μs*
External modulation	*Max.50kHz*

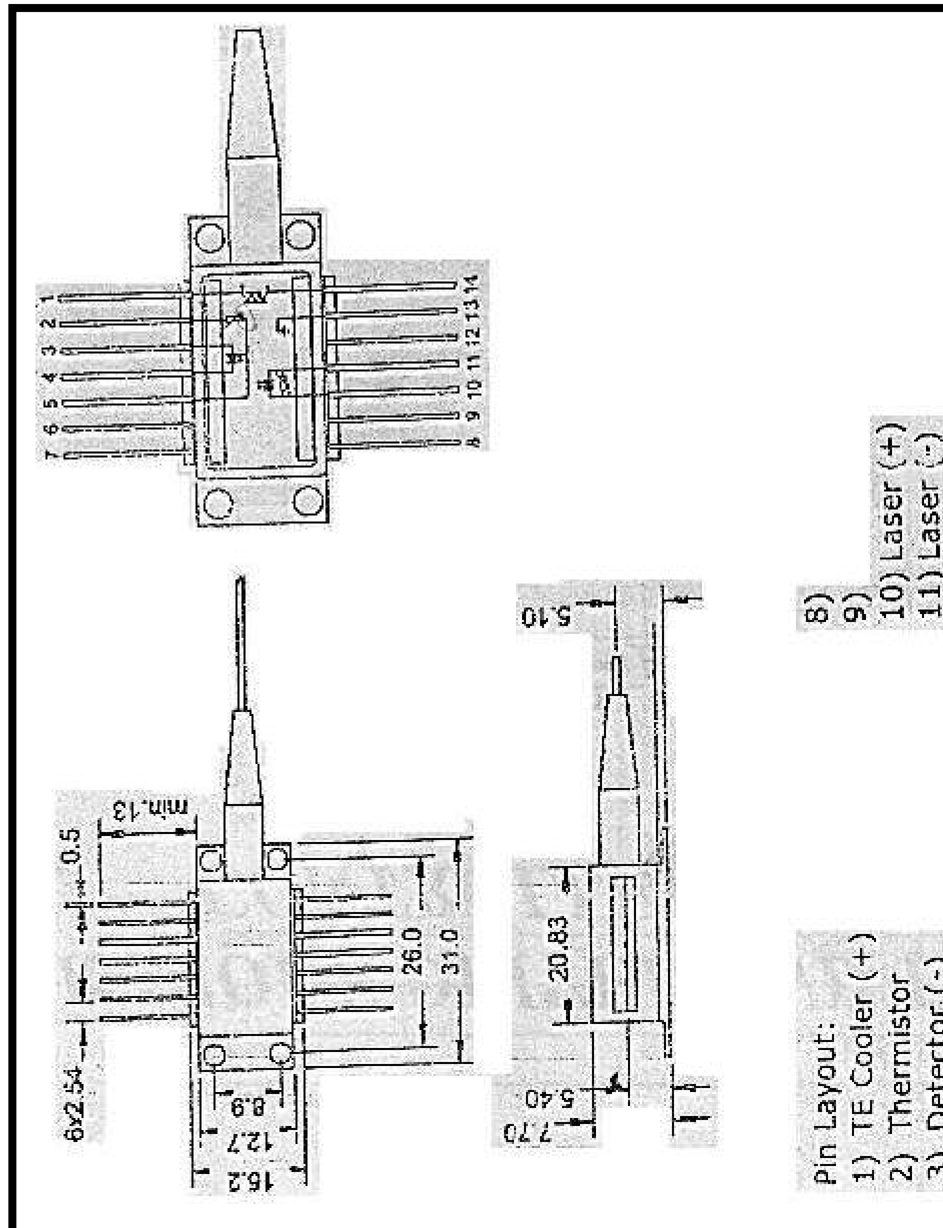

Fig.(3) the mechanical dimensions of the laser diode unit, [50].

Table (2) the electrical and optical characteristics at T_c=25°C, [47].

Item		Symbol	Conditions	Min.	Typ.	Max.	Unit
Threshold current		Ith			60	80	mA
Operating current		Iop	Po=1.0W		1.4	2.0	A
Operating voltage		Vop	Po=1.0W		2.1	3.0	V
Wavelength		λ_p	Po=1.0W	800	810	820	nm
Monitor current		Imon	Po=1.0W V_R=10V	0.3	1.5	6.0	mA
Radiation angle (F.W.H.M)	Perpendicular	$\theta\perp$	Po=1.0W	20	30	40	degree
	Parallel	$\theta_\parallel$		4	9	17	degree
Positional accuracy	Position	ΔX, ΔY	Po=1.0W			±50	μm
	Angle	$\Delta\Phi\perp$				±3	degree
Differential efficiency		η_D	Po=1.0W	0.5	0.75		W/A

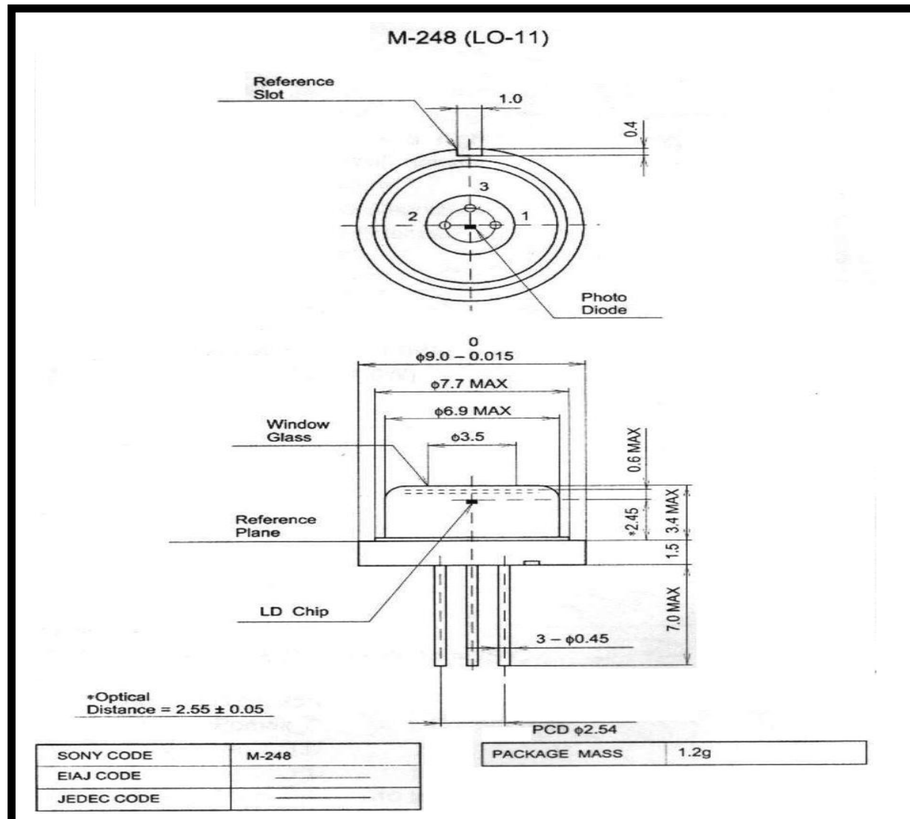

Fig.(4) the mechanical dimensions of the QW laser diode, units mm, [47].

Supervisor Certification

I certify that this thesis entitled **(Analysis of Quantum Well Laser Operation in Diode-Pumped Solid State Lasers)** was prepared under my supervision at the Department of Laser and Optoelectronics/ University of Technology**,** in partial Fulfillment of the requirements for the Degree of Doctor of Philosophy in **(Laser Engineering)**.

Signature:
Name: Dr. Adawiya J. Haider
Title: Assistant Professor
Address: Applied Science Department
University of Technology
Date: / /2008

In view of the available recommendation, I forward this thesis for debate the examination committee.

Signature:
Name: Dr. Sabah A. Dhahir
Title: Lecturer
Date: / /2008

Quantum Well Lasers:

It is similar in most respects to the conventional double heterostructure laser except for the thickness of the active layer. In the quantum well it is ~50 -100 A. while in the conventional lasers it is ~1.000 A. the main advantage to derive from the thinning of the active region is almost too obvious to state- a decrease in the threshold current that is nearly proportional to the thinning . The carrier density in the active region needed to render the active region transparent is ~10^{18} cm^{-3}.[1]

Carriers in Quantum Wells:

The essential difference between the gain of a pumped quantum well semiconductor medium and that of a bulk semiconductor laser has to do with the densities of states in both media.

We consider the electron in the conduction band of a QW to be free (with an effective mass mc) to move in the x and y directions, but to be confined in the z (normal to the junction planes) as shown in the figure( ).[1]

The Density of states

Since the electron is free in the 'x' and 'y' directions, we apply two- dimensional quantization by assuming the electrons are confined to a rectangle L_xL_y. this leads to quantization of the components of the **k** vectors

$k_x = n\,\pi/L_x$ n=1,2,…. , $k_x = m\,\pi/L_y$ m=1,2,……

the area in **k**⊥ space per one eignstate is thus $A_k = \pi^2/ L_x L_y = \pi^2/ A_\perp$. the number of states with transverse values of $k^{'}$ less than some given k is obtained by dividing the area $\pi k^2/4$ by A_k (the factor ¼ is due to the fact that **k**⊥ and - **k**⊥ describes the same state). the result is where a factor of two for the two spin orientations of each electron was included.

The number of states between k and k+dk is

$$\rho(k)dk = \frac{dN(k)}{dk}dk = A_\perp \frac{k}{pi}dk \qquad (1.1)$$

And is the same for the conduction or valance band. The total number of states with total energies between E and E+dE is

$$\frac{dN(E)}{dE}dE = \frac{dN(k)}{dk}\frac{dk}{dE}dE \qquad (1.2)$$

The number of states per unit area is thus

$$\frac{1}{A_\perp}\frac{dN(E)}{dE} = \frac{k}{\pi}\frac{dk}{dE} \qquad (1.3)$$

With **k**⊥ [1]

The first injection lasers consisted of chips of GaAS of rectangular shape into which a planar p-n junction was diffused. The external appearance of such a laser is shown in Fig.(   ). The threshold current density in simple p-n junction semiconductor laser described above is very high, particularly if it is not cooled below room temperature, lying in the range 35-100 kA/cm^2. the heterostructure layers in a semiconductor laser confine the light and the injected carriers in the direction perpendicular to the junction, in many laser applications an optical source is needed whose width in the plane of the junction is not a great deal larger than its thickness perpendicular to the junction. In some cases it may be required that the width be most comparable with the thickness, although more frequently an appreciably wider source is preferred to provide a higher limiting output power. We refer to the confinement of both carriers and light in the junction plane as 'lateral confinement'. [2]

All diode lasers currently used employ a double heterostructure. This structure can reduce the threshold current density by two orders of magnitude (to approximately 103 A/cm^2) owing to:
_ Photon confinement: The active layer is surrounded by layers of a higher refractive index. As such the structure acts as a waveguide, and prevents the laser radiation from extending into regions of high loss.
_ Carrier confinement: The surrounding layers also have large band gaps which confines the current carriers to the active region. The resulting increase in carrier density increases the gain.
_ Reduced absorption: The large energy gap of the surrounding layers ensures that any laser radiation which does extend beyond the active region experiences much lower absorption than it would if the band gap were the same as that in the active layer.
Figure 8.1 shows schematically the structure of heterostructure diode lasers made from (a) AlGaAs and (b) InGaAsP. In each case the active layer (0:15-0.35 μm) is surrounded by thicker layers of n- and p-doped material with a higher band gap. Figure 8.2 shows the variation of the refractive index, laser intensity, and band gap along a line perpendicular to the p-n junction under conditions of forward bias. It is clear that the higher band gap of the surrounding material prevents current carriers from moving beyond the active layer. Further, the diode laser radiation is surrounded by layers of higher refractive index and hence the mode is guided.

The selection of materials from which to make the cladding layers is a crucial one; not only must their band gap be larger than that of the intrinsic layer, but they must also be capable of being deposited via epitaxial growth techniques on the active region to form crystals free from defects without grain boundaries or regions of dislocation. This means that the alloy used for cladding must have a lattice constant very closely matched to that of the intrinsic material.

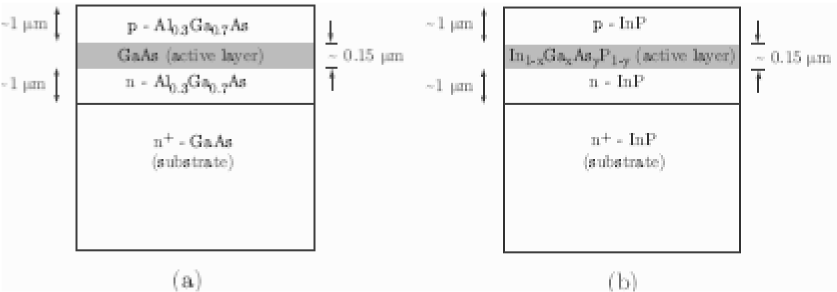

Fig (8-1)

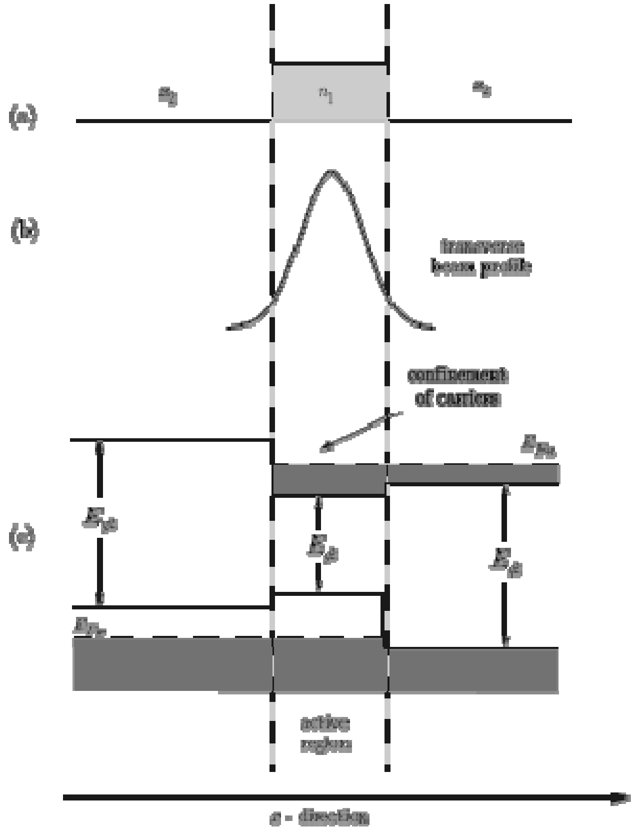

Fig.(8-2)

As shown in Figure 8.3, if we start with pure GaAs, by adding increasing atomic proportions x of aluminium to form the ternary alloy Ga1-xAlxAs the lattice spacing is virtually the same whatever the proportion of added Al, even to the extent of replacing all of the Ga by Al to form AlAs since the lattice spacing of GaAs and AlAs are almost identical: 0.564 and 0.566 nm respectively. This is however a happy circumstance unique to the GaAs system. In general quarternary compoundsmust be employed. For example, in In1-xGaxAsyP1-y the lattice spacing can be matched to the III-V semiconductor InP if y = 2:2x. With this ratio fixed, adjusting x then varies the band gap energy, allowing the output of the diode laser to be adjusted between 1150 nm and 1670 nm. This range is particularly useful since it covers the second (1300 nm) and third (1550 nm) transparency windows of silica _bres. InGaAsP diode lasers therefore find widespread application in telecommunications.

Refrencres:

1. optical electronics in modern communication, Yariv.
2. physics of semiconductor laser devices, Thompson.
3. Laser science and quantum information processing-laser physics, 2005 (internet source.

Contents

Abstract *I*

List of Symbols and Abbreviations *V*

Contents *VIII*

Chapter One: Introduction

1.1 Historical Background **1**

1.2 Motivation **4**

1.3 Quantum Well Laser **8**

1.4 Diode-Pumped Solid-State Lasers **14**

1.4.1 Compact Active Mirror Laser (CAMIL) **20**

1.4.2 Face Pumping and its Limitations **21**

1.4.3 Side Pumped CAMIL **22**

1.5 Literature Survey **24**

1.5 Aim of the Work **28**

1.6 Thesis Layout **29**

Chapter Two: Theoretical Concepts

2.1 Introduction **30**

2.2 Some Semiconductor Background **30**

2.3 Quantum Well Lasers **34**

2.3.1 In-Plane Dispersion **34**

2.3.2 The Density of States **37**

2.3.3 Gain in QW lasers **38**

2.3.4 Current Equilibrium Radiative and Non-Radiative **43**

2.3.5 Power Output of Injection Lasers **44**

2.4 Diode Pumping Techniques **46**

2.4.1 Input versus Output Characteristics **46**

2.4.2 Conversion of input to output energy **48**

Chapter Three: Proposal of GaAs/AlGaAs QW Structure

3.1 Introduction 53
3.2 GaAs/AlGaAs Laser 53
3.3 GaAs/AlGaAs with Different Al Concentration 54
3.4 Why GaAs/AlGaAs Lasers 56
3.5 Proposal or Prototype Structure 56
3.6 Flow Chart of the Analysis 59

Chapter Four: Experimental Work and Improvements

4.1 Introduction 62
4.2 Face Pumping 62
4.3.1 The Laser Diode Driver 64
4.3.2 The Laser Diode Unit 65
4.4 The Laser Cavity 68
4.5 The Setup Performance Procedure and Operation 69
4.6 The Alignment Procedure 70

Chapter Five: Results and Discussion

5.1 Introduction 73
5.2 Theoretical Model Results 73
5.2.1 Characterization of GaAs/AlGaAs Bulk Diode Laser 73
5.2.2 Characterization of GaAs/AlGaAs QW Laser 82
5.2.2.1 Spectral Gain- Carrier Density Distribution 82
5.2.2.2 Spontaneous Emission Rate 87
5.2.2.3 Peak Modal Gain and Transparency Density 90
5.2.2.4 Nonradiative Transitions and Carrier Leakage 91
5.2.2.5 Radiative QW Current 94
5.3 Heat Treatment of QW Laser 97
5.4 Experimental Results 98
5.4.1 L-I Characteristics of the Pumping Source 98

5.4.2 The Spatial Profile **100**
5.4.3 Laser Output Performance and Measurements **103**
5.4.3.1 Direct Face Pumping (Pulsed Operation) **103**
5.4.3.2 V-Shape Face Pumping **110**

Chapter Six: Conclusions and Suggestions for Future Work

5.1 Conclusions **117**
5.2 Future Work **118**
References **119**
Appendix

Chapter one

Introduction

Chapter Two

Theoretical Concepts

Chapter Three

Proposal of GaAs/AlGaAs QW Structure

Chapter Five

Results and Discussion

Chapter Six

Conclusions and Future Work

Chapter Four

Experimental Work and Improvements

Appendix A

2.1 Introduction:

Semiconductor lasers are attractive for research because they are both physically very interesting and technologically important. This is especially true for quantum well lasers. In the last decade, the importance of the quantum well laser had steadily grown until today; it is preferred for most semiconductor laser applications.

This growing popularity is because, in almost every respect, the quantum well is somewhat better than conventional lasers with bulk active layers.

This chapter deals with the difference in two most important features which are the Schrödinger's wave equation and density of states of the bulk and QW lasers besides the dynamics.

2.2 Some Semiconductor Background:

The outer electrons of the atoms of a semiconductor material are delocalized over the whole crystal; the corresponding wave functions can then be written as Bloch wave functions, [3]:

$$\Psi(\mathbf{r})=u_k(\mathbf{r})\exp[j(\mathbf{k}\bullet\mathbf{r})] \qquad (2.1)$$

Where $u_k(\mathbf{r})$ has the periodicity of the crystalline lattice.

Within the parabolic band approximation, E versus k relation can be approximated as a parabola. This leads to the view in Fig.(2.1) for valence and conduction bands.

The energy E_c in the conduction band, measured from the bottom of the band upwards, can be written as:

$$E_c = \frac{\hbar^2 k^2}{2 m_c} \qquad (2.2)$$

where m_c is the effective mass of the electron at the bottom of the conduction band. Likewise, energy in the valence band, measured from the top of the band downward, can be written as:

$$E_v = \frac{\hbar^2 k^2}{2 m_v} \qquad (2.3)$$

where m_v is the effective mass of the electron at the top of the valence band.

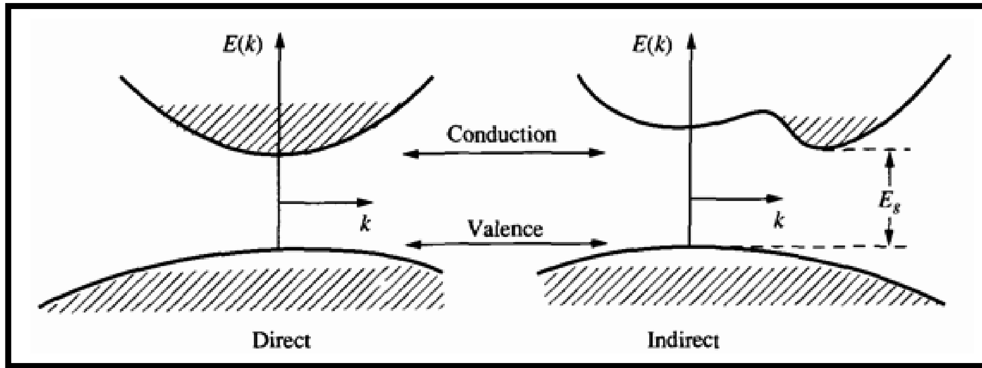

Fig.(2.1) E(k) vs. k (momentum) for direct and indirect semiconductors. The shaded areas are intended to imply states filled with an electron, and the white areas are empty, [16].

This simple one-dimensional model is generalized to the three- dimensional case by letting k_x, k_y, and k_z be the components of the electron's **k** vector, where $k^2 = k_x^2 + k_y^2 + k_z^2$.

It is often needed to perform electron counting, not in **k** space but as a function of the energy. The density of states function ρ(E) (the number of the electronic states per unit energy interval per unit crystal volume) is determined from the conservation of state relation, [3]:

$$\rho(E)dE = \frac{1}{V}\rho(k)dk \quad \text{...(2.4)}$$

With the use of eq.(2.2) leads to, [1, 45]:

$$\rho_c(E) = \frac{1}{2\pi^2}\left(\frac{2m_c}{\hbar^2}\right)^{3/2} E^{1/2} \quad \text{...(2.5)}$$

or $\rho_c(\omega) = \hbar\rho_c(E) = \dfrac{1}{2\pi^2}\left(\dfrac{2m_c}{\hbar}\right)^{3/2} \omega^{1/2}$ ....(2.6)

where $\hbar\omega$=E. a similar expression but with m_c replaced by m_v, the effective mass in the valence band, applies to the valence band.

The probability that an electron state at energy E is occupied by an electron is given by the Fermi-Dirac law, [4]:

$$f(E) = \frac{1}{e^{(E-E_F)/kT} + 1} \quad \text{...(2.7)}$$

Where**:**

E_F is the Fermi energy,

T is the temperature.

Let an optical beam at a (radian) frequency ω_o travel through the crystal. This beam will induce downward b→ a.

Only transitions in which the upper and lower states have the same **k** vector are allowed, as shown in Fig.(2.2):

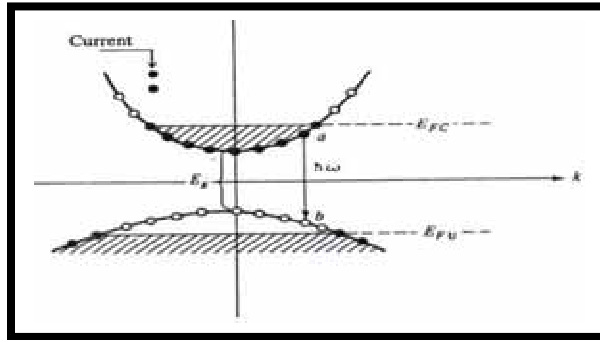

Fig.(2.2) Semiconductor medium characterized by quasi-Fermi E_{Fc} and E_{Fv}. A single level pair a-b with the same **k** value is shown. The induced a → b contributes one photon to the beam, [74].

As observed above, the quasi-Fermi levels indicate, in each band, the boundaries between occupied and empty states between occupied and empty sates. Consequently, the values of E_{Fc} and E_{Fv} in eq.(2.7) must depend on the number of electrons raised to the conduction band. To obtain this dependence, the electron density in the conduction band N_e and the hole density in the valence band N_h can be calculated as:

$$N_e = \int_0^\infty \rho_c(E_c)\, f_c(E_c)\, dE_c \text{ , } \qquad (2.8)$$

$$N_h = \int_0^\infty \rho_v(E_v)(1 - f_v(E_v))\, dE_v \text{ , } \qquad (2.9)$$

Let us consider a group of such levels with nearly **k** value and hence with nearly the same transition energy, [76]:

$$\hbar\omega(\mathbf{k}) = E_g + \frac{\hbar^2 k^2}{2m_c} + \frac{\hbar^2 k^2}{2m_v} = E_a - E_b \qquad (2.10)$$

and the expression for the gain constant is, [5]:

$$\gamma(\omega_o)=\frac{\lambda_o^{\ 2}}{8\pi^2 n^2\tau}\left(\frac{2m_c m_v}{\hbar(m_c+m_v)}\right)^{3/2}\left(\omega_o-\frac{E_g}{\hbar}\right)^{1/2}[f_c(\omega_o)-f_v(\omega_o)] \quad \text{.........................(2.11)}$$

The condition for the net gain $\gamma(\omega_o)>0$ is thus, [72]:

$$f_c(\omega_o)>f_v(\omega_o) \quad \text{.........................(2.12)}$$

Which is equivalent, in semiconductor, of the conventional inversion condition $N_2>N_1$, using eq.(2.7) , the gain condition (2.12) becomes:

$$\frac{1}{e^{(E_a-E_{Fc})/kT}+1}>\frac{1}{e^{(E_b-E_{Fv})/kT}+1} \quad \text{.........................(2.13)}$$

Recalling that E_a-E_b=$\hbar\omega_o$, eq.(2.11) is satisfied provided

$$\hbar\omega_o<E_{Ec}-E_{Fv} \quad \text{.........................(2.14)}$$

So that only frequencies whose photon energies $\hbar\omega_o$ are smaller than the quasi-Fermi levels separation are amplified. It follows from figure (2.3) that the semiconductor media is capable of achieving very large gain ranging up to a few hundred cm^{-1}. In a laser the amount of gain that actually prevails is clamped by the phenomenon of saturation to a value equal to the loss. In this region the plot of Fig.(2.3) can approximated by a linear relationship, [58, 48]

$$\gamma_{\max}=B(N-N_{tr}) \quad \text{.........................(2.15)}$$

where:

γ_{max} is the peak gain,

N_{tr} is the carrier density at transparency,

N is the injected carrier density,

B is differential gain coefficient of the semiconductor.

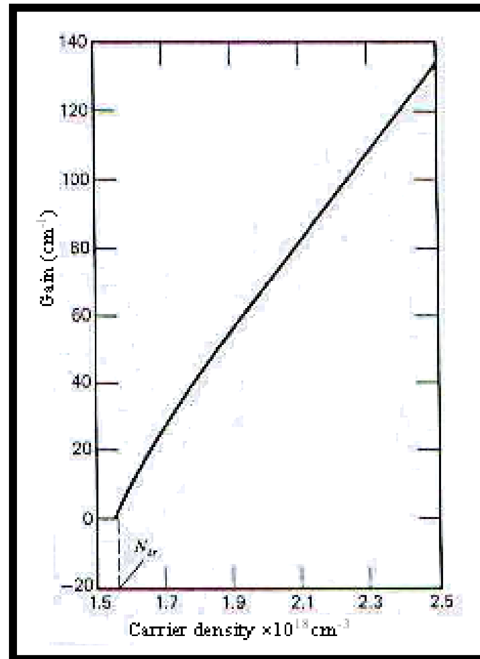

Fig.(2.3) A plot of the peak gain γ_{max} as a function of the injected carriers density at T=300°K, [7].

2.3 Quantum Well Lasers:

2.3.1 In-Plane Dispersion:

The time-independent Schrödinger equation summarises the wave mechanics analogy to Hamilton's formulation of classical mechanics, for time- independent potentials. In essence this states that the kinetic and potential energy components sum to the total energy; in wave mechanics, these quantities are the eignvalues of linear operators, i.e., [6]:

$$\hat{T}\psi + v\psi = E\psi \quad \text{.......(2.16)}$$

Where the eignfunction Ψ describes the state of the system. Again in analogy with classical mechanics the kinetic energy operator for a particle of constant mass is given by the following:

$$\hat{T} = \frac{P^2}{2m} \quad \text{.......(2.17)}$$

where P is the usual quantum mechanical linear momentum operator, [72]:

$$P = -i\hbar\nabla = -i\hbar\left(\frac{\partial}{\partial x}\mathbf{i} + \frac{\partial}{\partial y}\mathbf{j} + \frac{\partial}{\partial z}\mathbf{k}\right) \quad \text{.......(2.18)}$$

By using this form for the kinetic energy operator T, the Schrödinger equation then becomes [73]:

$$-\frac{\hbar^2}{2m}\left(\frac{\partial^2}{\partial x^2}+\frac{\partial^2}{\partial y^2}+\frac{\partial^2}{\partial z^2}\right)\psi+V(x,y,z)\psi=E\psi \quad \text{.....................................(2.19)}$$

Where the function V(x,y,z) represents the potential energy of the system as a function of the spatial coordinates.

If the one- dimensional potential V(z) is constructed from alternating thin layers of dissimilar semiconductors, then the particle, whether it be an electron or a hole, can move in the plane of the layers as shown in Fig.(2.4)

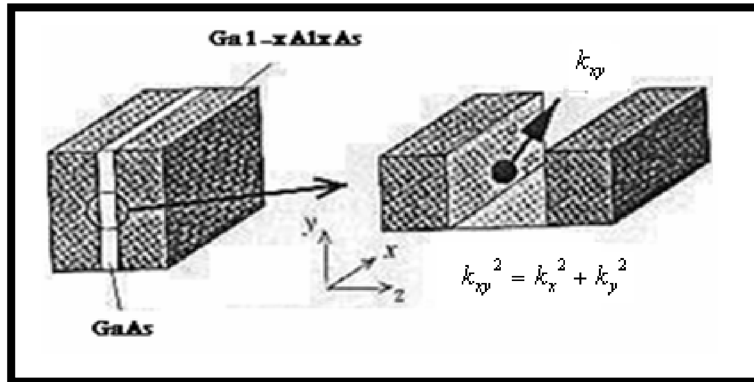

Fig.(2.4) a GaAs/$Ga_{1-x}Al_xAs$ layered structure and the in-plane motion of a charge carrier, [74].

As the potential can be written as a sum of independent functions, i.e. V=V(x)+V(y)+V(z), where it just happens in this case that V(x)=V(y)=0, the eignfunction of the system be written as a product:

$$\Psi(x,y,z)=\Psi_x(x)\,\Psi_y(y)\,\Psi_z(z) \quad \text{.. (2.20)}$$

Substituting eq.(22) into eq(21) gives, [73]:

$$-\frac{\hbar^2}{2m}\frac{\partial^2\psi_x}{\partial x^2}=E_x\psi_x \quad \text{...(2.21)}$$

$$-\frac{\hbar^2}{2m}\frac{\partial^2\psi_y}{\partial y^2}=E_y\psi_y \quad \text{...(2.22)}$$

$$-\frac{\hbar^2}{2m}\frac{\partial^2\psi_z}{\partial z^2}+V(z)\psi_z=E_z\psi_z \quad \text{...(2.23)}$$

In this case it must be remembered that the solution will represent a moving particle. Thus the eignfunction must reflect a current flow and have complex components, so the standard traveling wave is considered, $\exp(ik_x x)$, then:

$$-\frac{\hbar^2}{2m}\frac{\partial^2}{\partial x^2}\exp(ik_x x) = E_x \exp(ik_x x) \quad \text{.........(2.24)}$$

So $$\frac{\hbar^2 k_x^{\ 2}}{2m} = E_x \quad \text{.........(2.25)}$$

Which is clearly just the kinetic energy of a wave traveling along the x-axis, a similar equation follows for the y-axis, and hence the in-plane motion of a particle in a one-dimensional confining potential, but of infinite extent in the x-y plane can be summarized as, [60]:

$$\psi_{x,y}(x,y) = \frac{1}{A}\exp[i(k_x x + k_y y)] \quad \text{and} \quad E_{x,y} = \frac{\hbar^2 |\mathbf{k}_{x,y}|^2}{2m} \quad \text{.........(2.26)}$$

Therefore, while solutions of Schrödinger's equation along the axis of the one-dimensional potential produce discrete states of energy E_z=E_n, in the plane of a semiconductor quantum well there is a continuous range of allowed energies, as illustrated in Fig.(2.5):

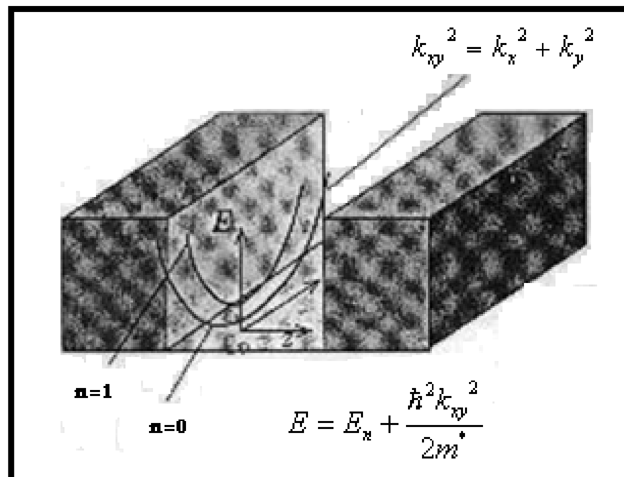

Fig.(2.5) Schematic showing the in-plane ($\mathbf{k}_{x,y}$) dispersion curves and the subband structure, [74].

Summarizing then, within a semiconductor quantum well system the total energy of an electron or hole, of a mass m^*, with in-plane momentum $\mathbf{k}_{x,y}$ is equal to E_z+$E_{x,y}$, which is given by, [76]:

$$E = E_n + \frac{\hbar^2 |\mathbf{k}_{x,y}|^2}{2m} \quad \ldots\ldots\ldots\ldots\ldots\ldots\ldots\ldots\ldots\ldots\ldots\ldots\ldots(2.27)$$

2.3.2 The Density of States:

Since the electron is free in the 'x' and 'y' directions, applying two-dimensional quantization is by assuming the electrons are confined to a rectangle L_xL_y. This leads to quantization of the components of the **k** vectors

$k_x = n\ \pi/L_x$ n =1,2,…. , $k_x = m\ \pi/L_y$ m =1,2,……

The area in **k**⊥ space per one eignstate is thus $A_k = \pi^2/ L_x L_y = \pi^2/ A_\perp$. The number of states with transverse values of k less than some given k is obtained by dividing the area $\pi k^2/4$ by A_k (the factor ¼ is due to the fact that **k**⊥ and **-k**⊥ describes the same state). The result is where a factor of two for the two spin orientations of each electron was included.

The number of states between k and k+dk is, [3]:

$$\rho(k)dk = \frac{dN(k)}{dk}\, dk = A_\perp \frac{k}{\pi} dk\ , \ldots\ldots\ldots\ldots\ldots\ldots\ldots\ldots\ldots\ldots\ldots\ldots\ldots (2.28)$$

And is the same for the conduction or valance band. The total number of states with total energies between E and E+dE is

$$\frac{dN(E)}{dE} dE = \frac{dN(k)}{dk}\frac{dk}{dE} dE\ , \ldots\ldots\ldots\ldots\ldots\ldots\ldots\ldots\ldots\ldots\ldots\ldots\ldots (2.29)$$

The number of states per unit area is thus

$$\frac{1}{A_\perp}\frac{dN(E)}{dE} = \frac{k}{\pi}\frac{dk}{dE}\ , \ldots\ldots\ldots\ldots\ldots\ldots\ldots\ldots\ldots\ldots\ldots\ldots\ldots (2.30)$$

With **k**⊥ → **k** , n=1, and by limiting the discussion to the conduction band, the relation between the electron energy at the lowest state n=1 and its **k** value is:

$$k = \sqrt{\frac{2m_c}{\hbar^2}}\left(E - E_{1c}\right)^{1/2} \quad \ldots\ldots\ldots\ldots\ldots\ldots\ldots\ldots\ldots\ldots\ldots\ldots\ldots(2.31)$$

So that the two dimensional density of states (per unit energy and unit area) is:

$$\rho_{QW}(E) \equiv \frac{1}{A_\perp}\frac{dN(E)}{dE} = \frac{m_c}{\pi\hbar^2}\ , \ldots\ldots\ldots\ldots\ldots\ldots\ldots\ldots\ldots\ldots\ldots\ldots\ldots(2.32)$$

Once $E>E_{2c}$, an electron of a given total energy E can be found in either n=1 or n=2 state so that the density of states at $E=E_{2c}$ doubles. At $E=E_{3c}$ it triples, and so on. This leads to the staircase density of states function. The total density of states can be expressed mathematically, [6]:

$$\rho_{QW}(E) = \sum_{n=1}^{all\ states} \frac{m_c}{\pi\hbar^2} H(E - E_{nc}) \quad \text{.....(2.33)}$$

Since ρ_{QW} is constant in each subband, the density of electrons N_e and holes N_h can be calculated analytically and the result will be, [17]:

$$N_e = kT\sum_n \left(\frac{m_c}{\pi\hbar^2 L_z}\right)\ln\left[1+\exp\left(\frac{E_{Fc}-E_{nc}}{kT}\right)\right], \quad \text{.....(2.34)}$$

$$N_h = kT\sum_n \left(\frac{m_v}{\pi\hbar^2 L_z}\right)\ln\left[1+\exp\left(\frac{E_{Fv}+E_{nv}}{kT}\right)\right], \quad \text{.....(2.35)}$$

2.3.3 Gain in QW Lasers:

To obtain an expression for the gain of an optical wave confined (completely) within a quantum well medium. An amplifying transition at some frequency $\hbar\omega_o$ is shown in Fig.(2.6). The upper electron state and the hole state (the unoccupied electron state in the valence band) have the same n and **k** values, so that the transition energy is, [72]:

$$\hbar\omega = E_c - E_v = E_g + E_c(\mathbf{k},n) + E_v(\mathbf{k},n)$$

$$= E_g + \left(\frac{1}{m_c}+\frac{1}{m_v}\right)\frac{\hbar^2}{2}\left(k^2 + n^2\frac{\pi^2}{L_z^2}\right)$$

$$= E_g + \frac{\hbar^2}{2m_r^*}\left(k^2 + n^2\frac{\pi^2}{L_z^2}\right) \quad \text{.....(2.36)}$$

where:

$$m_r^* = \frac{m_c m_v}{m_c + m_v} \quad \text{.....(2.37)}$$

n=1, 2, …… is the quantum number.

The effective inversion population density due to carriers between k and k+dk is thus, [3]:

$$N_2 - N_1 \rightarrow \frac{kdk}{\pi L_z}\left[f_c(E_c) - f_v(E_v)\right] \quad \ldots\ldots(2.38)$$

Where:

$$N_1(m^{-3}) \rightarrow \frac{\rho_{QW}(\mathbf{k})}{L_z} dkf_v(E_v)\left[1 - f_c(E_c)\right] = \frac{k}{\pi L_z}\left(f_v - f_v f_c\right)dk ,$$

$$N_2(m^{-3}) \rightarrow \frac{\rho_{QW}(\mathbf{k})}{L_z} dkf_c(E_c)\left[1 - f_v(E_v)\right] = \frac{k}{\pi L_z}\left(f_c - f_c f_v\right)dk ,$$

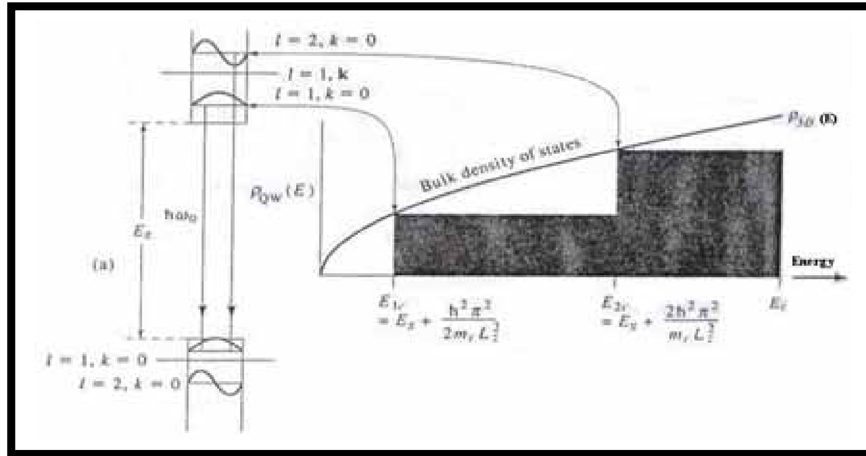

Fig.(2.6) (a) The first two l=1,l=2 quantized electron and hole states and their eignfunction in an infinite potential well. (b) a plot of the volumetric density of states $(1/AL_z)/[dN(E)/dE]$ (i.e. the number of states per unit area (A) per unit energy divided by the thickness z of the active region) of electrons in a quantum well and of a bulk semiconductor, [3].

The contribution to the gain due to electrons within dk and in a single, say n=1 sub-band as, [3]:

$$d\gamma(\omega_o) = \frac{kdk}{\pi L_z}\left[f_c(E_c) - f_v(E_v)\right]\frac{\lambda_o^{\;2}}{4n^2\tau}\frac{T_2}{\pi\left(1 + (\omega - \omega_o)^2 T_2^{\;2}\right)} \quad \ldots\ldots(2.39)$$

Where T_2 is the coherence collision time of the electrons and τ is the electron-hole recombination lifetime assumed to be constant. It is more convenient to transform from the k variable to the transition frequency ω from eq.(2.36) it follows that, [3]:

$$dk = \frac{m_r^{\;*}}{\hbar k}d\omega \quad \ldots\ldots(2.40)$$

So that eq.(2.37) becomes:

$$\gamma(\omega_o)_{n=1} = \frac{m_r^{*}\lambda_o^{2}}{4\pi\hbar L_z n_1^{2}\tau}\int_0^{\infty}\left[f_c(\hbar\omega) - f_v(\hbar\omega)\right]\frac{T_2 d\omega}{\pi\left[1+(\omega-\omega_o)^2 T_2^{2}\right]} \qquad \text{.............................(2.41)}$$

Where we used the convention that f_c(ħω) is the Fermi function at the upper transition (electron) energy E_c, while f_v(ħω) is the valence band Fermi function at the lower transition energy. To include, as it should be, the contributions from all other sub-bands (n=2,3,….) we replace, using eq.(2.33):

$$\frac{m_r^{*}}{\pi\hbar^2} \rightarrow \frac{m_r^{*}}{\pi\hbar^2}\sum_{n=1}^{\infty} H(\omega-\omega_n) \qquad \text{.............................(2.42)}$$

Where ħω_n is the energy difference between the bottom of the n=1 sub-band in the conduction band and the n sub-band in the valence band:

$$\hbar\omega_n = E_g + n^2\frac{\hbar^2\pi^2}{2m_r^{*}L_z^{2}} \qquad \text{.............................(2.43)}$$

To get an analytic form for eq.(2.39) we will assume that the phase coherence "collision" time T_2 is long enough so that:

$$\frac{T_2}{\pi\left[1+(\omega-\omega_o)^2 T_2^{2}\right]} \rightarrow \delta(\omega-\omega_o) \qquad \text{.............................(2.44)}$$

Which simplifies eq.(2.41) to

$$\gamma(\omega_o) = \frac{m_r\lambda_o^{2}}{4\pi\hbar L_z n_1^{2}\tau}\left[f_c(\hbar\omega_o) - f_v(\hbar\omega_o)\right]\sum_{n=1}^{\infty} H(\hbar\omega_o - \hbar\omega_n) \qquad \text{.............................(2.45)}$$

The basic expression for the modal gain, [69]:

$$g = \frac{power\ generated\ per\ unit\ length\ (in\ x)}{power\ carried\ by\ beam}$$

$$= \frac{-\int_{-\infty}^{-d/2}\alpha_n|E|^2 dz + \int_{-d/2}^{d/2}\gamma|E|^2 dz - \int_{d/2}^{\infty}\alpha_p|E|^2 dz}{\int_{-\infty}^{\infty}|E|^2 dz} \qquad \text{.............................(2.46)}$$

where:

γ is the gain constant experienced by a plane wave in a medium whose inversion density is equal to that of the active medium,

α_n is the loss constant of the unpumped n-$Ga_{1-x}Al_xAs$ and is due mostly to free electron absorption,

α_p is the loss (by free holes) in the bonding p-$Ga_{1-}xAl_xAs$ region. Note that as d→∞, g→γ.

It is convenient to rewrite eq.(46) as, [69, 72]:

$$g = \gamma\Gamma_a - \alpha_n\Gamma_n - \alpha_p\Gamma_p \quad \text{....(2.47)}$$

$$\Gamma_a = \frac{\int_{-d/2}^{d/2} |E|^2 dz}{\int_{-\infty}^{\infty} |E|^2 dz} \quad \text{....(2.48)}$$

$$\Gamma_n = \frac{\int_{-\infty}^{-d/2} |E|^2 dz}{\int_{-\infty}^{\infty} |E|^2 dz} \quad \text{....(2.49)}$$

$$\Gamma_p = \frac{\int_{d/2}^{\infty} |E|^2 dz}{\int_{-\infty}^{\infty} |E|^2 dz} \quad \text{....(2.50)}$$

$$\Gamma_a + \Gamma_n + \Gamma_p = 1 \quad \text{....(2.51)}$$

where:

Γ_a is very nearly the fraction of the mode power carried within the active GaAs layer,

Γ_n and Γ_p are, respectively, the fraction of the power in the n and p regions.

The threshold gain condition is, [53]:

$$\gamma\Gamma_a = \alpha_n\Gamma_n + \alpha_p\Gamma_p - \frac{1}{L}\ln R + \alpha_s \quad \text{....(2.52)}$$

Under steady- state conditions the rate at which carriers are injected into the active region must equal the electron-hole recombination rate, [7]:

$$\frac{J}{q} = \frac{NL_z}{\tau} \quad \text{....(2.53)}$$

where:

J is the injected carrier density,

τ is the electron-hole recombination time.

The optical gain is calculated using standard perturbation theory Fermi's Golden Rule, (neglecting the effect of intraband scattering). Since the gain anisotropy favors lasing in TE modes, we calculate the gain only for this polarization. The spectrally dependent gain coefficient for the quantum well region is, [62, 49]:

$$g(E)=\frac{q^2|M|^2}{E\varepsilon_o m^2 c_o \hbar L_z}\sum_{i,j} m_r C_{ij} A_{ij}\left[f_c-(1-f_v)\right]H\left(E-E_{ij}\right) \qquad (2.54)$$

where:

$|M|^2$=bulk momentum transition matrix element,

ε_o =free-space permittivity,

m=free electron mass,

c_o=vacuum speed pf light,

N=effective refractive index,

i,j= conduction, valence quantum numbers (at Γ),

m_r=spatially weighted reduced mass,

C_{ij}=spatial overlap factor between states i and j,

A_{ij}=anisotropy factor for transition i, j,

f_c=Fermi population factor for conduction electrons,

f_v=Fermi population factor for valence holes,

H= Heaviside step function,

E_{ij}=transition energy between states i and j.

For TE transition, with the electric field vector in the plane of the QW, its values are, [64]

$$\begin{aligned} A_{ij} &= \left(3/4\right)\left(1+\cos^2\theta_{ij}\right) && (heavy\ hole) \\ &= \left(1/4\right)\left(5-3\cos^2\theta_{ij}\right) && (light\ hole) \end{aligned} \qquad (2.55)$$

And for TM transitions, with the electric field normal to the QW, its values are, [53]:

$$A_{ij} = \left(\frac{3}{2}\right)\left(\sin^2 \theta_{ij}\right) \quad (heavy\,hole)$$
$$= \left(\frac{1}{2}\right)\left(4 - 3\sin^2 \theta i_{ij}\right) \quad (light\,hole) \qquad \text{.....................(2.56)}$$

The angular factor is

$\cos^2 \theta_{ij} = E_{ij}/E$

and shows decreasing anisotropy between nearby heavy and light hole transitions as the photon energy increases deeper into the band.

The bulk averaged momentum matrix element between conduction and valence states is, [67]:

$$|M|^2 = \frac{m^2 E_g \left(E_g + \Delta\right)}{6m_c\left(E_g + 2\Delta/3\right)} \qquad \text{.....................(2.57)}$$

where:

$$E_g = \left[E_o - \frac{5.405\times10^{-4}\times T^2}{T+204}\right], \qquad \text{.....................(2.58)}$$

E_g = direct bandgap,

E_o = bandgap constant,

T = operating temperature,

$\Delta_{s\text{-}o}$ = split-off band separation,

m_c = conduction band effective mass.

2.3.4 Current equilibrium- radiative and non-radiative:

The radiative component of carrier recombination is found from the spectrally dependent spontaneous emission rate, [49]:

$$R(E) = \frac{16\pi^2 N q^2 E|M|^2}{\varepsilon_o m^2 c_o{}^3 h^4 L_z}\sum_{i,j} m_r C_{ij}\left[f_c . f_v\right] H\left(E - E_{ij}\right) \qquad \text{.....................(2.59)}$$

Equation (2.59) is an expression for the total spontaneous emission density into all angles and at all polarizations, and therefore does not contain the polarization anisotropy, which has removed by angular integration.

The radiative QW component of the current is calculated from the integral over the spontaneous emission spectrum of the QW, is given by, [58]:

$$J_r = L_z\, q \int_{E_{g,h1}}^{E_{g,b}} R_{sp}(E)\, dE \,, \qquad (2.60)$$

Where:

$E_{g,h1}$ = transitions at the lower cutoff at the effective bandgap of the QW,

$E_{g,b}$ = transitions at the upper cutoff at the bandgap of the barrier.

The more important nonradiative contributions to the current come from thermal leakage of the carriers over the confining potential barriers, and from Auger recombination. For interface recombination assuming identical interfaces in all of the structure for SQW, [6]:

$$J_s = 2\, q\, N\, v_s \,, \qquad (2.61)$$

where:

N = QW carrier density,

v_s = interface recombination velocity.

The Auger current density is given by:

$$J_A = L_z q\, C_A N^3 \,, \qquad (2.62)$$

where C_A = Auger coefficient.

and the leakage current density is given by:

$$J_{lk} = e d_g N_b / t_b \,, \qquad (2.63)$$

where:

$N_b = 2(m_b\, kT / 2\pi \hbar^2)^{3/2}$ is the leakage carrier concentration at the barrier,

d_g is the guided thickness,

t_b is the lifetime for the electrons into the guiding region above the barrier potential.

2.3.5 Power output of injection lasers:

As the injection current is increased above the threshold value the laser oscillation intensity builds up. The resulting stimulated emission shortens the lifetime of the inverted carriers to the point where the magnitude of the inversion is clamped at its threshold value. Taking the

probability that an injected carrier recombines radiatively within the active region as η_i, the following expression for the power emitted by stimulated emission can be written as, [71, 72]:

$$P_e = \frac{(I - I_t)\eta_i}{q} h\upsilon \quad \text{..........(2.64)}$$

Part of this power is dissipated inside the laser resonator, and the rest is coupled out through the end reflectors.

These two powers are according to eq.(2.52) proportional to the effective internal loss $\alpha = \alpha_n \Gamma_n + \alpha_p \Gamma_p + \alpha_s$ and $-L^{-1} \ln R$, respectively. We can write the output power as

$$P_o = \frac{(I - I_t)\eta_i h\upsilon}{q} \frac{\left(1/L\right)\ln\left(1/R\right)}{\alpha + \left(1/L\right)\ln\left(1/R\right)} \quad \text{..........(2.65)}$$

The external differential quantum efficiency η_{ex} is defined as the ratio of the photon output rate that results from an increase in the injection rate (carriers per second) to the increase in the injection rate:

$$\eta_{ex} = \frac{d\left(P_o / h\upsilon\right)}{d\left[(I - I_t)/e\right]} \quad \text{..........(2.66)}$$

Using eq.(55) we obtain:

$$\eta_{ex}^{-1} = \eta_i^{-1}\left(\frac{\alpha L}{\ln\left(1/R\right)} + 1\right) \quad \text{..........(2.67)}$$

By plotting the dependence of η_{ex} on L we can determine η_i, which in GaAs is around 0.9-1.0. Since the incremental efficiency of converting electrons into useful output photons is η_{ex}, the main remaining loss mechanisms degrading the conversion of electrical to optical power is the small discrepancy between the energy qV_{appl} supplied to each injected carrier and the photon energy hv. This discrepancy is due mostly to the series resistance of the laser diode. The efficiency of the laser in converting the electrical power input to optical power is thus, [17]:

$$\eta = \frac{P_o}{VI} = \eta_i \frac{I - I_t}{I} \frac{h\upsilon}{qV_{appl}} \frac{\ln\left(1/R\right)}{\alpha L + \ln\left(1/R\right)} \quad \text{..........(2.68)}$$

2.4 Diode Pumping Technique:

2.4.1 Input versus Output Characteristics:

The optical losses in the diode structure determine the threshold current I_{th} that has to be extended before amplification can take place. A diode laser that is operating above threshold will exhibit a linear relationship between output power and electrical current as shown in Fig.(2.7). The optical output power as a function of current input can be expressed by, [75]:

$$P_{out} = \eta_d(\Delta E/q)(I - I_{th}), \qquad (2.69)$$

Where:

η_d is the differential quantum efficiency characterized by the number of photons emitted per injected electrons,

ΔE is the bandgap of the recombination region,

q is the charge of the electron.

The slope efficiency σ_s, determined from the slope of the output power versus input current, follows from (2.69):

$$\sigma_s = \eta_d(\Delta E/q), \qquad (2.70)$$

The applied forward voltage for diode laser is:

$$V_o = (\Delta E/q) + iR_d, \qquad (2.71)$$

Where:

R_d is the series resistance of the diode due to the resistivity of the epilayers and the resisitivity of the metal contacts.

For typical devices the drop voltage across the junction is 1.5V and one obtains V_o=1.5V+iR_d.

The energy conversion efficiency of the diode laser, defined as the ratio of the optical output power to electrical input power, which we call the pump efficiency η_p, follows the form of the above equations, [75]:

$$\eta_p = \frac{\sigma_s(i - i_{th})}{i[(\Delta E/q) + iR_d]}, \qquad (2.72)$$

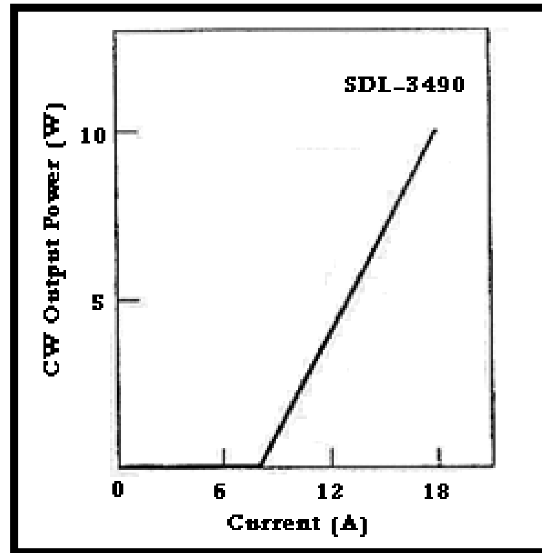

Fig.(2.7) the CW output power versus input current for a 1-cm bar, [75]

To involve the thermal effects, the heat conduction equation is given by, [78]:

$$\rho_m c_p \frac{\partial T}{\partial t} = k_z \frac{\partial^2 T}{\partial z^2} + Q(n,T) \, , \quad ......(2.73)$$

where:

ρ_m is the mass density o the active region,

c_p is the specific heat capacitance of the active region,

k_z is the thermal conductivity of the active region,

Q(n,T) is process involved in the generation of heat and the thermal exchange that occurs between laser and heat sink.

$$Q(n,T) = h(n,T) - \zeta \times (T - T_{hs}) \, , \quad ......(2.74)$$

where:

h(n,T) is the function describes the power density of the heat production within the active region,

ζ is the term which shows the thermal interaction of the laser and the heat sink.

$$\zeta = -0.054 \times \left(1 + \exp\left[\frac{-(VP-15)}{4.2}\right]\right)^{-1} + 0.055 \, , \quad ......(2.75)$$

2.4.2 Conversion of Input to Output Energy:

The flow of energy from electrical input to laser output radiation is illustrated schematically in Fig.(2.8). Also listed are the principal factors and design issues that influence the energy conversion process. There are different ways of partitioning this chain of transfer processes. This approach was chosen from an engineering point of view, which divides the conversion process into steps related to individual system components. As shown in Fig.(2.8), the energy transfer from electrical input to laser output can conveniently be expressed as a four- step process, [71]:

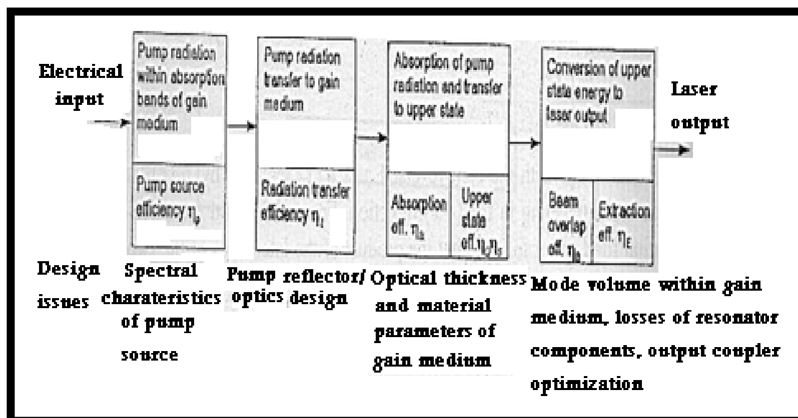

Fig.(2.8) Energy flow in a solid- state laser system, [71].

a. Conversion of electrical input delivered to the pump source to useful pump radiation:

We define as useful radiation the emission from the pump source that falls within the absorption bands of the laser medium. The pump source efficiency η_p is therefore the fraction of electrical input power that is emitted as optical radiation within the absorption region of the gain medium. The output of a lser diode or a diode array represents all useful pump radiation, provided the spectral output is matched to the absorption band of the gain medium. Typical values for η_p for commercially available cw and quasi-cw diode arrays are 0.3-0.5, [71].

The magnitude of η_p is dependent on the thickness of the active material because as the thickness increases, radiation at the wings of the absorption band will start to contribute more to the pumping action.

b. Transfer of the useful pump radiation emitted by the pump source to the gain medium:

In diode- pumped lasers the radiation transfer is very simple. In so- called end-pumped lasers, the transfer system usually consists of lenses for the collection and focusing of diode radiation into the laser crystal. Furthermore, in side pumped systems, the laser diodes are mounted in close proximity to the laser crystal without the use of any intervening optics. If we express reflection losses and spill-over losses at the optics at the optics or active medium by the parameter r, we can write, [75]:

$\eta_t = (1 - r)$, ……………………..………………………………..……….(2.76)

Since the laser crystal and optical components are all antireflection coated, the radiation transfer losses are very small in these systems. Values for the radiation transfer efficiency are typically η_t=0.85-0.98.

c. Absorption of pump radiation by the gain medium and transfer of energy to the upper laser level:

This energy transfer can be divided into two processes. The first is the absorption of the pump radiation into pump bands of the gain medium expressed by η_a, and the second is the transfer of energy from the pump band to the upper laser level expressed by $\eta_Q \eta_S$.

The absorption efficiency is the ratio of power P_a absorbed to power P_c entering the laser medium,[71]:

$\eta_a = P_a / P_c$, ………………………………………………………...……………(2.77)

The quantity η_a is a function of the path length and the spectral absorption coefficient of the laser medium integrated over the emission spectrum of the pump source. For diode pumped lasers, the absorption efficiency can be approximated by:

$\eta_a = 1 - \exp(-\alpha_o l)$, …………………………………………...…………………(2.78)

where:

α_o is the absorption coefficient of the laser crystal at the wavelength emitted by the diode and l is the path length in the crystal.

The upper state efficiency may be defined as the ratio of the power emitted at the laser transition to the power absorbed into the pump bands. This efficiency is the product of two contributing factors, the quantum efficiency η_Q, which is defined as the number of photons contributing to laser emission divided by the number of pump photons, and η_S, the quantum defect efficiency. The latter is sometimes referred to as the Stokes factor, which represents the ration of the photon energy emitted at the laser transition $h\upsilon_L$ to the energy of a pump photon $h\upsilon_p$, that is:

$$\eta_S = \left(\frac{h\upsilon_L}{h\upsilon_p}\right) = \frac{\lambda_p}{\lambda_L} \quad , \ldots\ldots(2..79)$$

where λ_p and λ_L are the wavelength of the pump transition and the laser wavelength, respectively.

d. Conversion of the Upper-State Energy to Laser Output:

The efficiency of this process can be divided into the fractional spatial overlap of the resonator mode with the pumped region of the laser medium and the fraction of the energy stored in the upper laser level which can be extracted as output.

The beam overlap efficiency η_B is defined as the resonator mode volume divided by the pumped volume of the active material. A value of η_B less than 1 indicates that the part of the inversion will decay by spontaneous, rather than stimulated emission. In an oscillator η_B expresses the mode- matching efficiency, that is, the spatial overlap between the resonator modes and the gain distribution. In an amplifier η_B is a measure of the spatial overlap between the input beam and the gain distribution in the laser material.

This subject usually does not receive a lot of attention in laser literature, but a poor overlap of the gain region of the laser with the laser- beam profile is often the main reason that a particular laser performs below expectations. The low overall efficiency of lasers with a TEMoo mode output is the result of a mode volume that occupies only a small fraction of the gain region of the laser rod. On the other hand, so-called end- pumped lasers, where the output from a laser diode pup is focused into the gain medium, achieve near- perfect overlap.

Values of η_B can range from as low as 0.1, for a laser rod of 5-mm diameter operated inside a large radius mirror resonator containing a 1.5-mm aperture for fundamental mode control, to

0.95 for an end- pumped laser operating at TEMoo. Multimode lasers typically achieve η_B=0.8-0.9.

The circulating power in an optical resonator is diminished by internal losses described by the round- trip loss δ and by radiation coupled out of the resonator. We will define an extraction efficiency η_E which describes the fraction of total available upper state energy or power which appears at the output of the laser:

$$\eta_E = P_{out} / P_{avail}, \quad (2.80)$$

An indication of the reduction of available output power due to losses in resonator can be obtained from the coupling efficiency:

$$\eta_E = T_1 / (T + \delta), \quad (2.81)$$

In a four- level system the laser output power can be obtained from the following equation, [71]:

$$P_{out} = \sigma_s (P_{in} - P_{th}), \quad (2.82)$$

Where σ_s is the slope efficiency of the output versus input curve, as shown in Fig(2.9)

$$\sigma_s = \left(\frac{-\ln R}{\delta - \ln R} \right) \eta \approx \frac{T_1}{T_1 + \delta} \eta, \quad (2.83)$$

The electrical input power at threshold is:

$$P_{th} = \left(\frac{\delta - \ln R}{2} \right) \frac{Ah\upsilon_L}{\eta \sigma \tau_f} \approx \left(\frac{T_1 + \delta}{2} \right) \frac{Ah\upsilon_L}{\eta \sigma \tau_f}, \quad (2.84)$$

$$\eta_o = \eta_p \eta_t \eta_a \eta_Q \eta_S \eta_B, \quad (2.85)$$

where:

τ_f is the florescence lifetime,

A is the cross section of the laser medium,

R is the reflectivity of the output coupler,

σ is the stimulated emission cross section,

T_1 is the transmission of the output coupler T=1-R,

η_o is the overall efficiency.

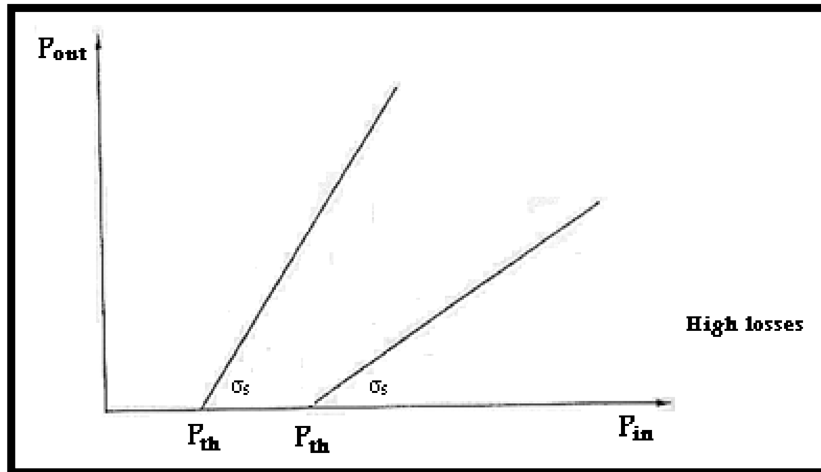

Fig.(2.9) Laser output versus pump input characterized by a threshold input power P_{th} and a slope efficiency σ_s, [75].

4.1 Introduction:

In this chapter the experimental work will be examined which includes the setup and performance of diode pumped disk laser using bulk and QW sources in different modes (CW, pulsed) with different pumping schemes, the details for each part used was given and presented.

4.2 Face Pumping:

The setup and performance of the diode pumped disk laser under CW pulsed (internal + external triggering) modes using bulk and QW pumping sources has been examined experimentally. In addition the details for each part of this arrangement were given, and explained briefly, Fig.(4.1) shows the schematic experimental arrangement of direct face pumping using bulk diode laser work.

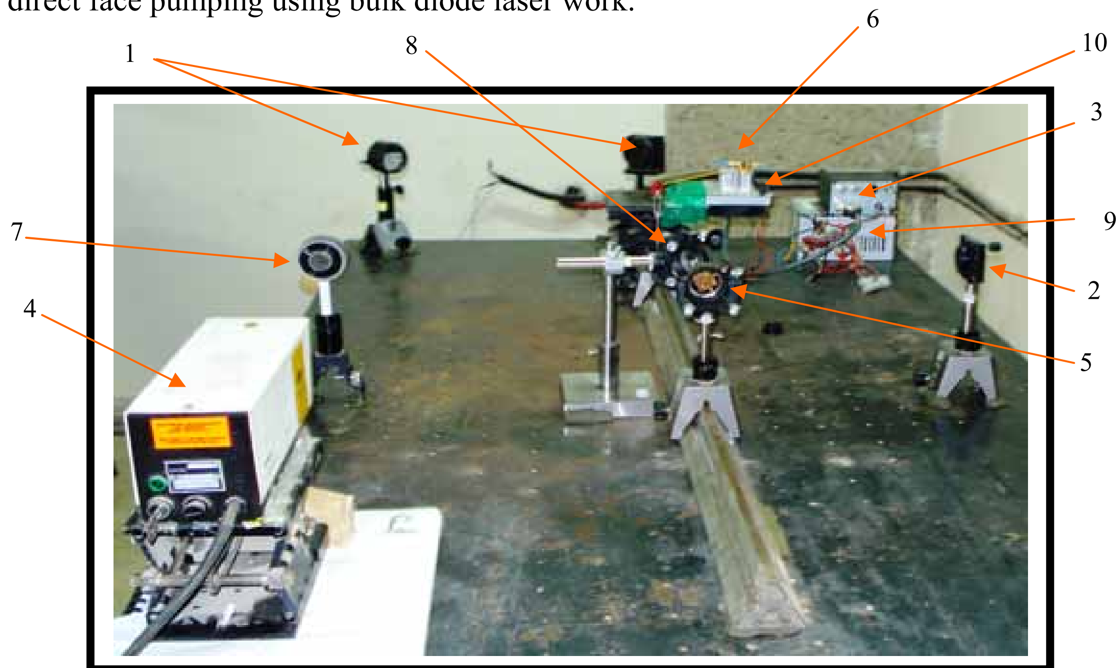

Fig.(4.1) Schematic experimental arrangement of direct face pumping using bulk diode laser.

The numbers in the Fig.(4.1) point to:

1. Alignment mirrors,
2. Output coupler mirror,
3. LD driver unit,
4. He-Ne laser,
5. Disk laser crystal,
6. LD+ optical fiber,
7. Pin hole,
8. BS,
9. DC power supply,
10. TEC+ heat sink.

The setup involves:

1. the laser diode driver +external power supply.
2. the laser diode unit
    a. laser diode,
    b. thermistor,
    c. TEC,
    d. Optical fiber.
3. two lenses
4. the cavity
    a. highly transmissive mirror,
    b. active medium (Nd:YVO_4) +rear mirror,
    c. output coupler mirror.

4.3.1 The Laser Diode Driver:

The laser diode driver "model (DD1-1T-D)" which is supplied from "Alphalas GmbH company (Germany)" shown in Fig.(4.2) consists of a controller to control the operating temperature and current of the laser diode so as not to exceed their limits, a built in frequency generator with a wide range of frequencies and pulse durations that can be varied using the control knobs (REP. rate, pulse) and a LCD used to monitor the values of the operating laser diode current (in CW and pulsed mode), the TEC current, Repetition rate, LD temperature.

An external DC power supply with two different voltages (5, 12) volts was used to operate the laser diode driver, the outer TEC element with 5 volts and the fan with 12 volts. More details about the laser diode driver are found in appendix (A).

Fig.(4.2) the laser diode driver with its external power supply.

4.3.2 The Laser Diode Unit:

A bulk 808 nm with single longitudinal mode laser diode was supplied from "Alphalas company", with a maximum CW power of 2 Watts (in CW mode) at λ typical =808 nm achieved at 2 volts, 1.9 A, and with a threshold current of 450 mA, an optical fiber of a diameter of 100µm is coupled to the laser diode so that the radiation emerges out of the fiber is circular in shape, while in pulsed mode (internal triggering) the laser diode gives an peak power of (1050 mW) with t_p= 0.16ms at an operating current of 3.2A with Prf=1.3 kHz, when using external triggering the laser diode gives a peak power of (2760 mW) with t_p=0.15 ms, at an operating current of 3.2A with Prf=3Hz.

For more information, the general specifications are illustrated in table (1), and the mechanical dimensions of the bulk laser diode, can be seen in appendix (A).

An outer TEC is placed on a heat sink and a fan used to prevent heating the laser diode, i.e. damaging it during its operation. Fig.(4.3) illustrates the laser diode placed on its cooling unit.

The second laser diode used in this experimental work was GaAlAs QW-SCH laser diode type (SDL 323V) in CW mode, manufactured by Sony with 1W maximum output power at λ (typical)=808 nm and operating lifetime of 10,000 H.

The maximum power of 873mW has been obtained at an operating voltage of 2.1 volts and a current of 1.4 A, the typical threshold value was (I_{th}=60 mA). The electrical and optical characteristics are illustrated in table (2) with the mechanical dimensions that are given in appendix (A).

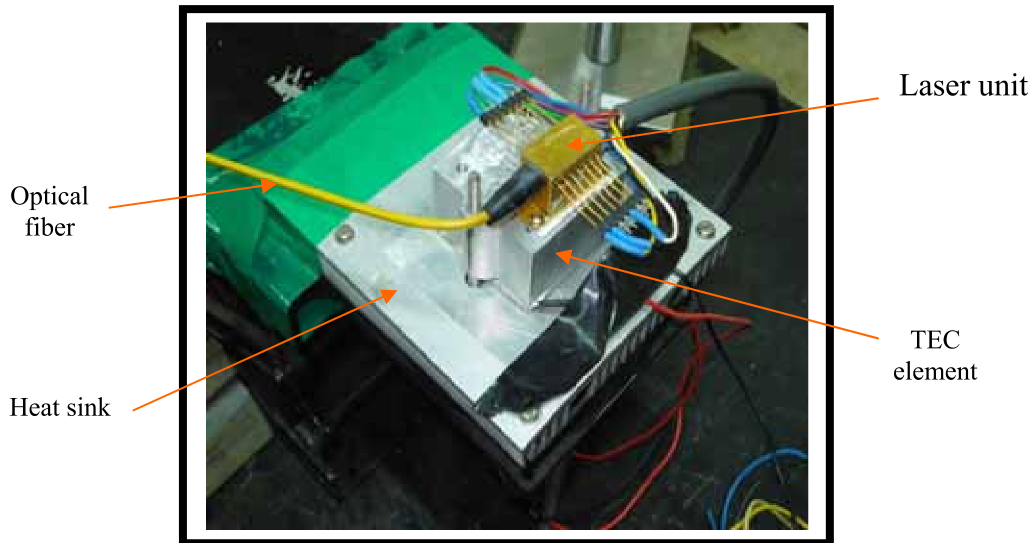

Fig.(4.3) The laser diode with the cooling unit.

The cooling system used for this laser diode was a CPU fan and a number of fins (as the heat sink) to provide sufficient cooling for the laser diode. The whole unit (laser diode, heat sink) are shown in Fig.(4.4)

Fig.(4.4) QW CW 810 nm GaAlAs laser diode.

As expected, it was found during the operation of the laser diode that this unit needs a powerful cooling during operation in CW mode (i.e. the TEC element and the fan), while in pulsed mode the laser diode unit needs less cooling (i.e. TEC alone when operating at high repetition rate), and there is no need for the fan due to the fact that in pulsed mode there exists a time the laser diode is on, else there it is off.

Fig.(4.5a,b) shows the shape of the spot emerging from the QW and the bulk diode laser respectively. As it is obvious from the two pictures the spots are highly divergent and need to be focused in order to reduce such divergence, so two lenses with focal lengths of

(f=5cm), (f=4.5cm) were used to focus the divergent beam of the laser diode on to the disk medium.

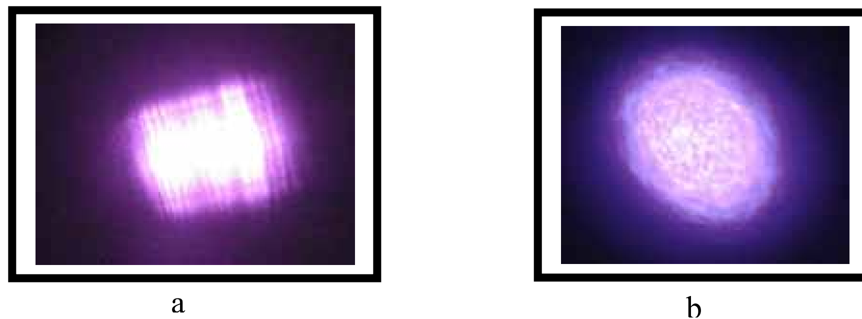

Fig.(4.5) the shape of (a)the QW laser diode spot, (b) the bulk laser diode spot.

4.4 The Laser Cavity:

The laser cavity that has been used in this work consists of:

1. Highly Transmissive Mirror:

This mirror was tilted by 45° so that no radiation at 1064 nm is transmitted from its face; the first face is HT at 808 nm, while the second face is AR coated at 808 nm and HR coated for 1064 nm at 45°. Fig.(4.6) shows the shape of this mirror supplied from "Alphalas company".

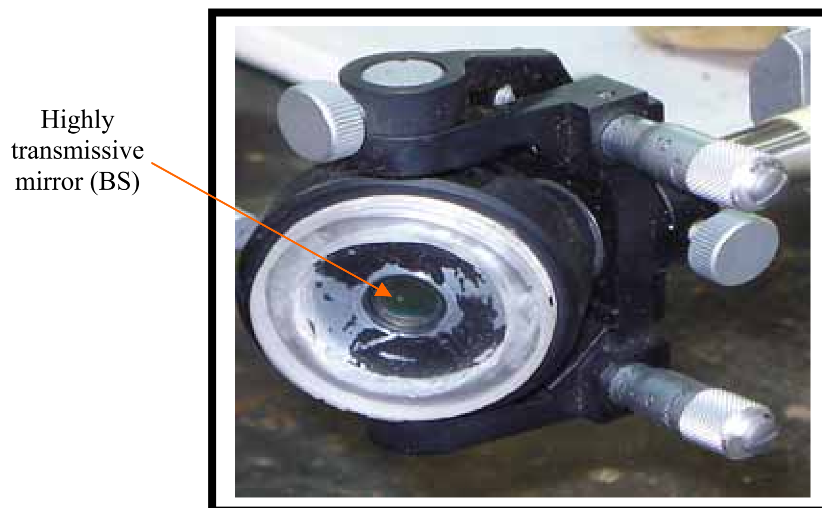

Fig.(4.6) Transmissive mirror placed at angle 45°.

2. The laser crystal:

A 4×5×1 mm^3 Nd:YVO_4 laser crystal with 0.3 at.% concentration has been used as an active medium, and located after the transmissive mirror. The rear mirror was deposited on the back face of the crystal with HR coating (R>99.8%) at 808 nm. The crystal was coated with an anti-reflection coating with high damage threshold for high power laser operation and reflectivity R<0.25% at 1064 nm. This crystal was placed on Al plate from its front surface and this plate contains a hole of diameter of 4 mm at its centre to permit the radiation comes from the pumping source to be incident on the crystal. This hole makes the crystal acts like a disk; also a Cu plate is on its back surface with indium material of 0.1 mm thickness as a thermal adhesive. Those plates serve as heat sink. Fig.(4.7) shows the laser crystal placed in its mount, this crystal was supplied from "Alphalas company".

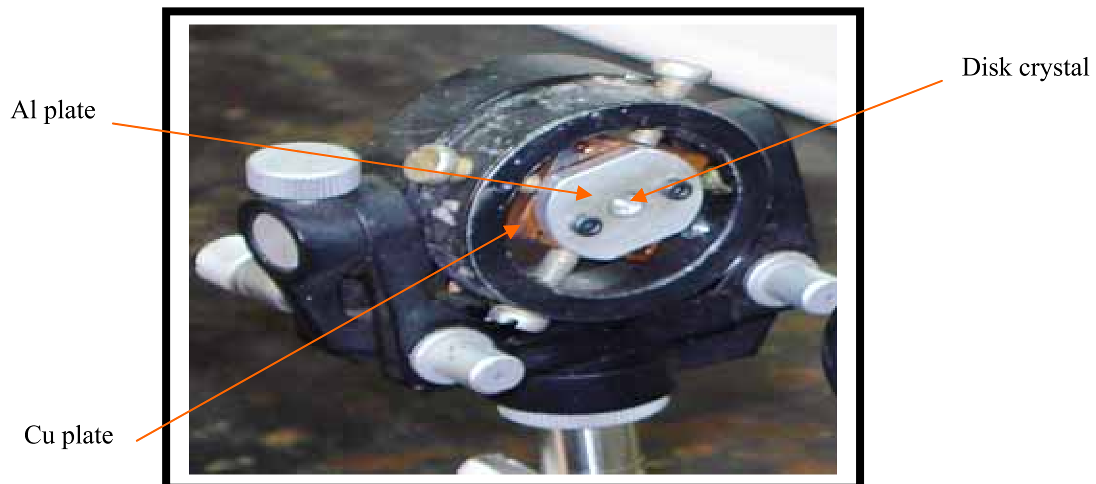

Fig.(4.7) Disk crystal in its mount.

3. The Output Coupler:

The output coupler supplied from "Alphalas company" has a (ROC=400 mm) and a reflectivity of 90% at 1064nm. So when the beam radiated from the laser diode at (λ=808 nm) it emerges the transmissive mirror after passing through the two lenses and fall upon the crystal, so the radiation emitted at 1064 nm from the crystal will be reflected at an angle of 45° towards the output coupler.

4.5 The Setup Performance Procedure and Operation:

The optical alignment was achieved using a He-Ne laser of an output power of (1.3 mW) manufactured by "PHYWE", which was placed on a jag. Two alignment mirrors were placed on the two holders to redirect the radiation comes from the He-Ne which passes through a pin-hole to fall upon the DPSSL system. An IR to visible converter was used to track the laser spot at each point of the system.

In CW operation the power was measured using a power meter from "genetec" which measures up to 10kW. A picture for this power meter is shown below in Fig.(4.8), while in pulsed (internal and external triggering) operation the output was measured using a joule meter, model "RJ-7610 Energy Radiometer" which measures the average energy for a number of pulses equals to (1, 10, 100), a picture of this joule meter is shown in Fig.(4.9).

Fig.(4.8) the genetic power meter.

Fig.(4.9) the energy joule meter.

The resonator length L of the two pumping schemes, and the two operating modes was varied to investigate its influence on the measured output power both in (external and internal triggering).

Also the reflectivity of the output coupler was varied and the output power was measured.

In external triggering the repetition rate was varied from f=3Hz to f=500Hz. The peak power from the bulk laser diode was measured due to this change, and the influence of changing the repetition rate on the peak laser output power using the direct and the V-shape face pumping was measured.

As the operating temperature of the bulk diode laser was controlled by the cooling unit, it affects the laser output power from the system. This effect was noticed and measured.

Varying the operating current of the diode laser will result in a change in its power, so the L-I characteristics was investigated in both pulsed and CW modes.

The spatial profile of the two diode lasers (QW, Bulk) is measured with varying the operating current, i.e. power from the diode laser, so the beam divergence (F.W.H.M) was measured in both the parallel and perpendicular directions.

4.6 The Alignment Procedure:

The ray direction for the direct face pumping of the disk medium using a highly transmissive mirror, bulk diode laser is shown in Fig.(4.10), where the ray emerging from the bulk diode laser was focused using two focusing lenses of (f=5,4.5 cm) in order to converge the highly diverging beam from it. Then the ray is incident on the disk crystal after passing through the highly transmissive mirror which was placed at an angle of 45° that will allow the 1.064μm wavelength reflected back from the highly reflective rear surface of the disk crystal to pass through it towards the output coupler mirror.

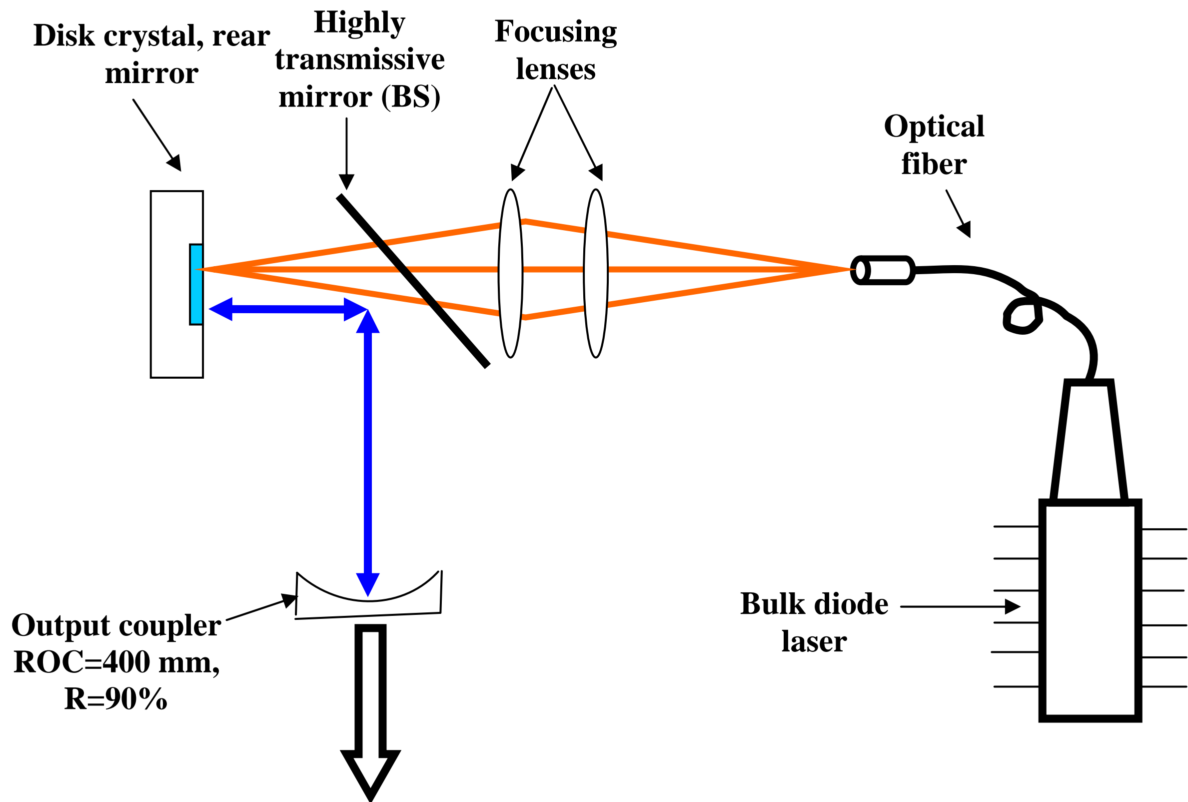

Fig.(4.10) Ray direction of the direct face pumping.

The ray direction for V-shape face pumping, was illustrated in Fig.(4.11), where the disk crystal and the output coupler mirror are placed at 45°, and the bulk diode laser are used as a pumping source once in CW mode and once in pulsed mode with internal and external triggering, while the QW diode laser is used as a pumping source in CW mode. Proper focusing lenses are used with the two pumping sources to focus the highly diverging beam from these sources.

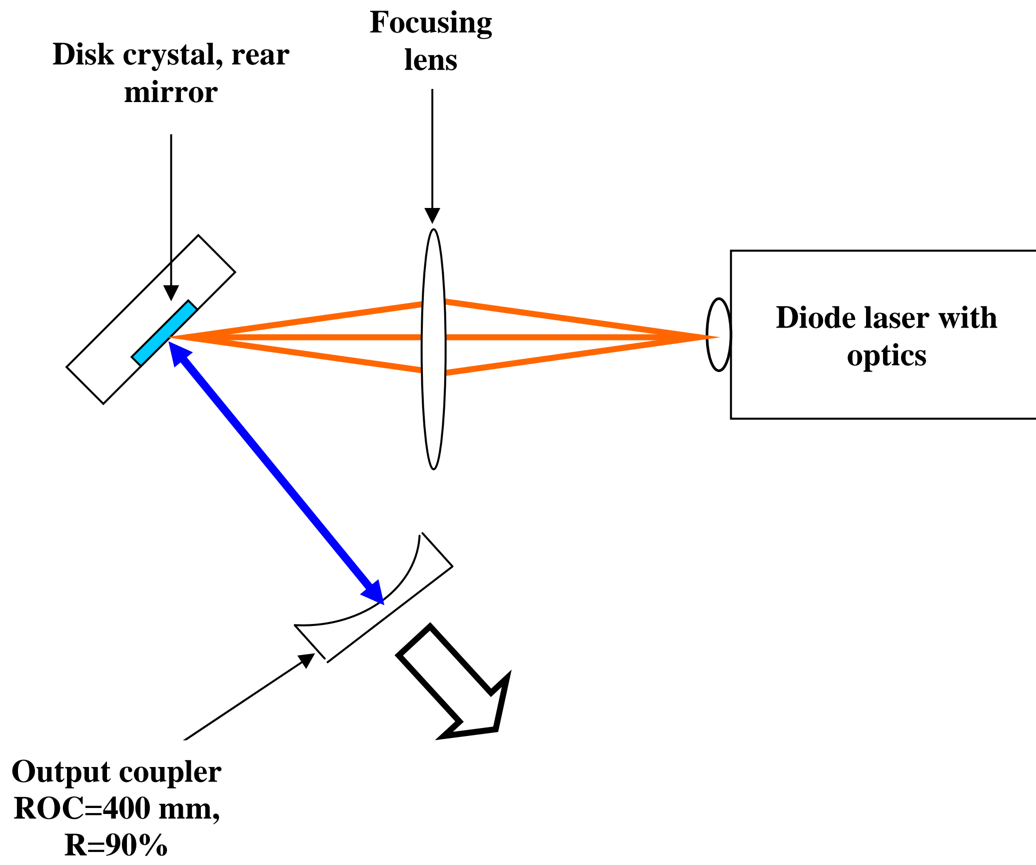

Fig.(4.11) Ray direction of the V-shape face pumping.

5.4 Experimental results

In this section, the results obtained from the experimental work were illustrated and investigated with the use of different pumping schemes and different types of laser diodes.

5.4.1 L-I Characteristics of the Pumping Source:

When the bulk laser diode is operated in pulsed mode the energy emitted from it was measured to be 95μJ at a repetition rate of 1.3 kHz at an operating current of 1.5A with pulse duration of 0.16 ms. Fig.(5.34) shows the relation between the driving current of diode laser and the peak power at repetition rates of 1.3,1.4,1.5 and 2 kHz. From this figure below it is obvious as it was expected the increasing the repetition rate will decrease the value of the emitted energy and hence the peak power, and the value of the threshold current was found to be Ith=0.45A which matches the value given by that of the company.

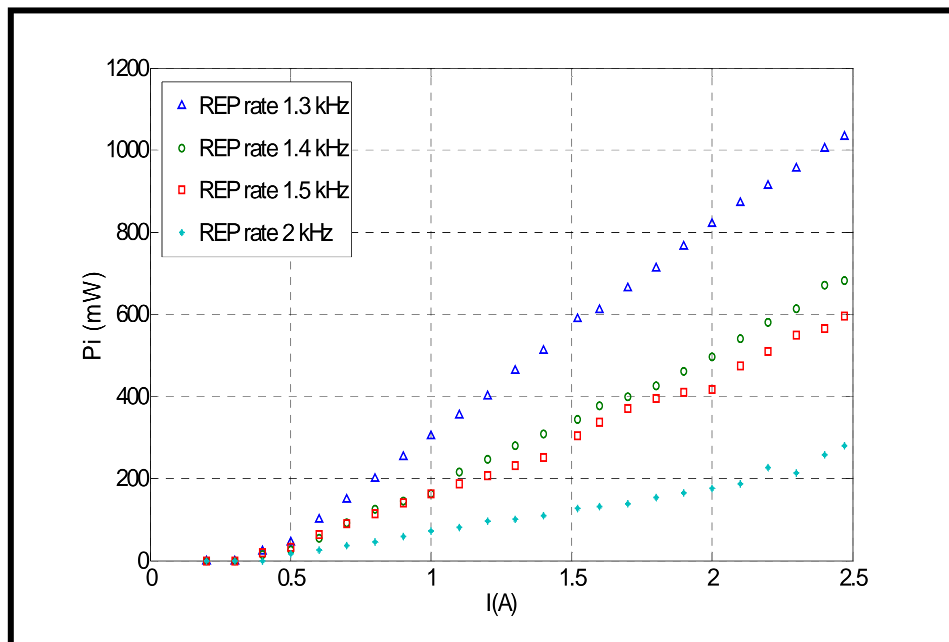

Fig.(5.34) The biasing current vs. the emitted peak power of the bulk diode laser at different repetition rates.

Fig.(5.35) shows the relation between the operating current and the CW power emitted from the bulk diode laser, where the measured differential efficiency was found to be η_D=0.87 W/A.

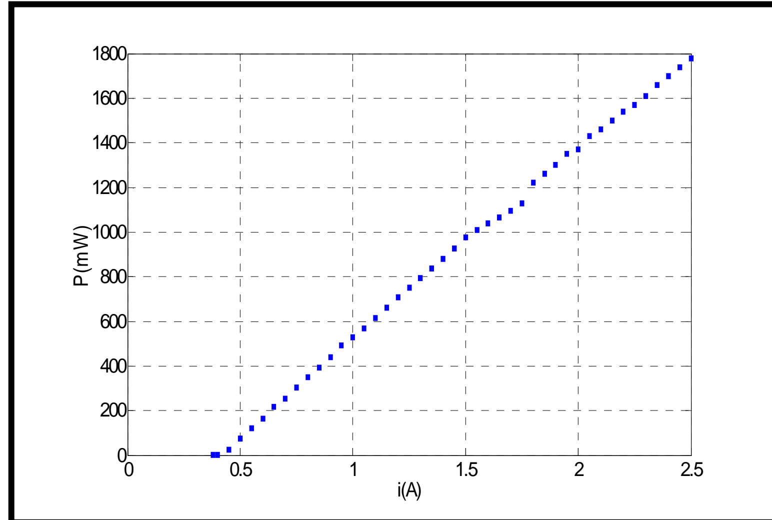

Fig.(5.35) L-I characteristics of the bulk diode laser operating in CW mode

For QW diode laser the threshold current was found to be Ith=70mA and the differential efficiency was found to be $\eta_D \approx 0.66$ W/A which is lower than the typical value given by the company (0.75W/A) due to the fact that the maximum power attained from the QW was 873mW instead of 1000mW. Fig.(5.36) shows the relation between the driving current of the QW diode laser and the CW output power.

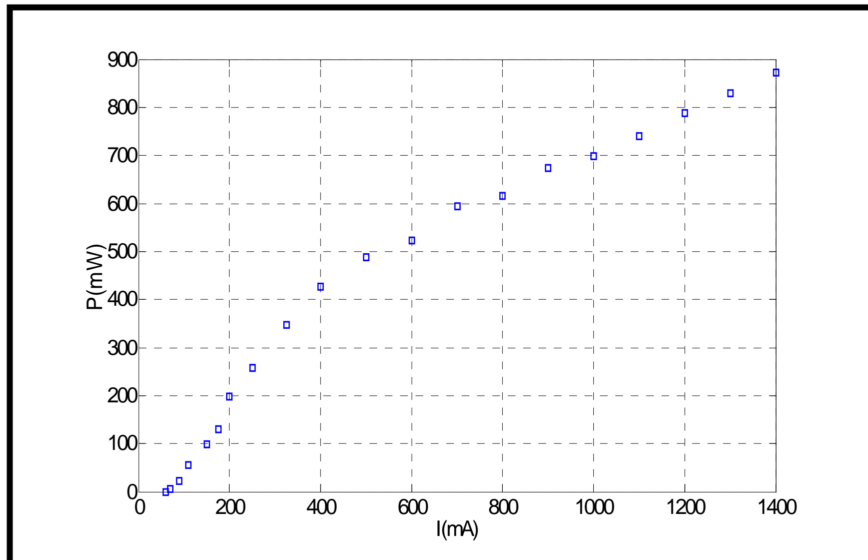

Fig.(5.36) L-I characteristics of the CW QW GaAlAs.

5.4.2 The spatial profile:

Fig.(5.37) shows the spatial profile of the bulk diode laser spot, the measured perpendicular angle of divergence was found to be 15.8° which is close to that given by the company. From this figure we can see that the intensity was measured for different laser powers and that increasing the power of the diode laser increases the intensity of the laser beam, the beam divergence is determined from the multilayer structure.

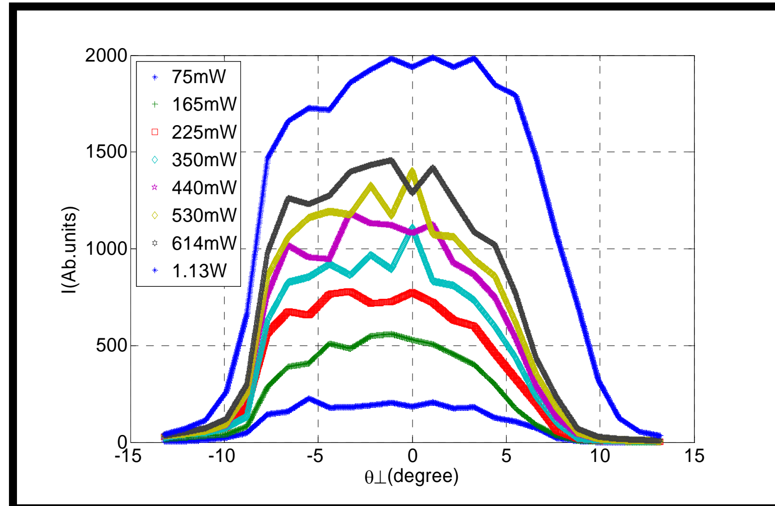

Fig.(5.37) Tthe intensity vs. the vertical divergence angle at different powers.

Fig.(5.38) shows the measured parallel beam divergence angle of the bulk diode laser which was found to be 9.1 at P=1.13W which is close to the value given by the company. From these two figures it is obvious that at low values of the power emitted from the diode laser the intensity profile is smooth and has no spikes but with increasing the power the fluctuations in the profile begin to appear. The beam divergence depends on the stripe width, and cavity length.

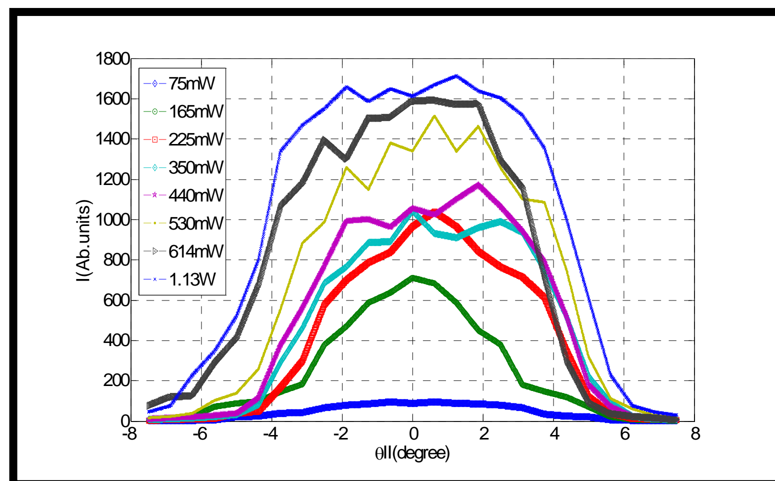

Fig.(5.38) The intensity vs. the parallel divergence angle at different powers.

Fig.(5.39a, b) shows the area under curve for the perpendicular and horizontal beam divergence for the bulk diode laser respectively. The fitted values show that the data has a cubic dependence on the operating current.

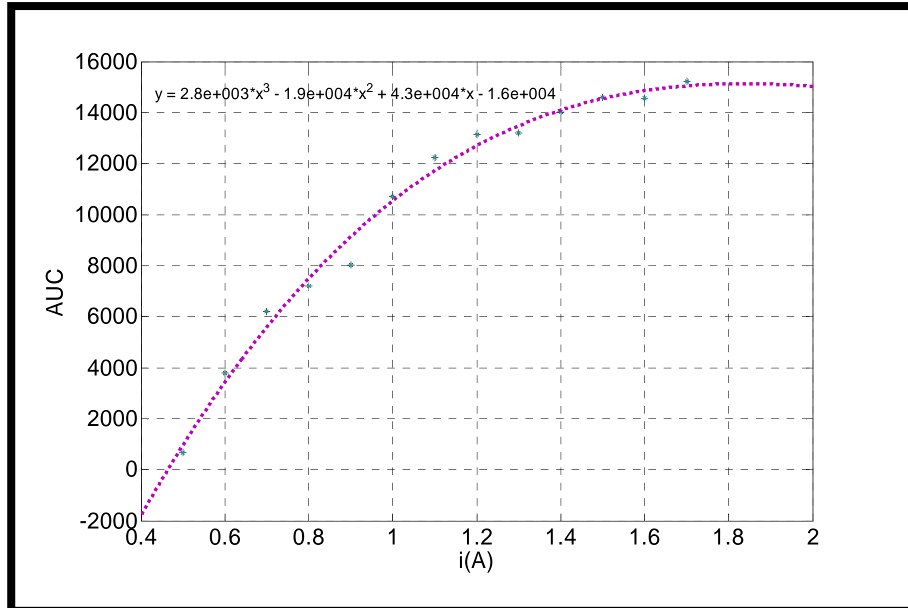

(a)

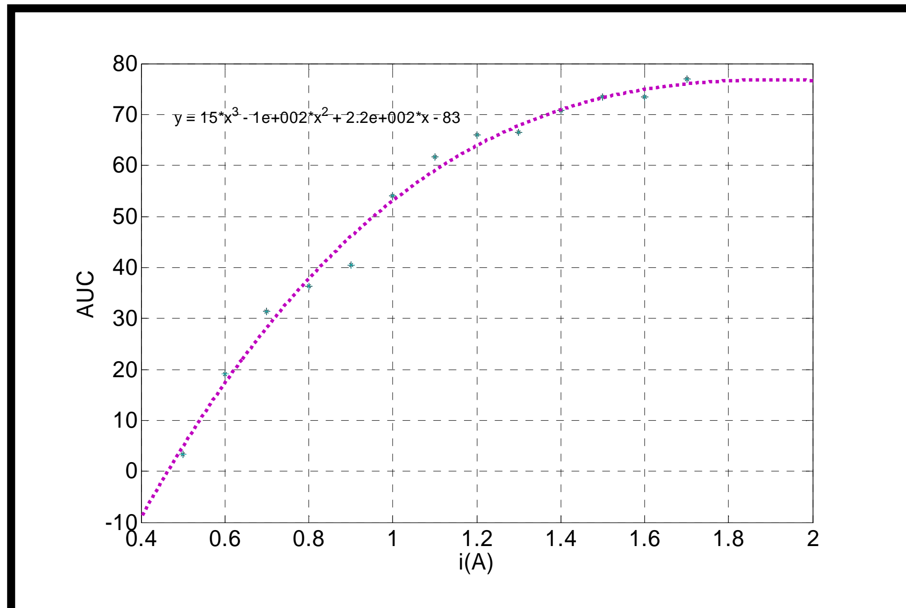

(b)

Fig.(5.39) The area under the curve for (a) the perpendicular, and (b) horizontal beam divergence

For the QW laser, Fig.(5.40) below shows the vertical beam divergence of the QW diode laser which was measured to be 25° at an emitting power of 873mW, which is between the minimum and typical value given by the company.

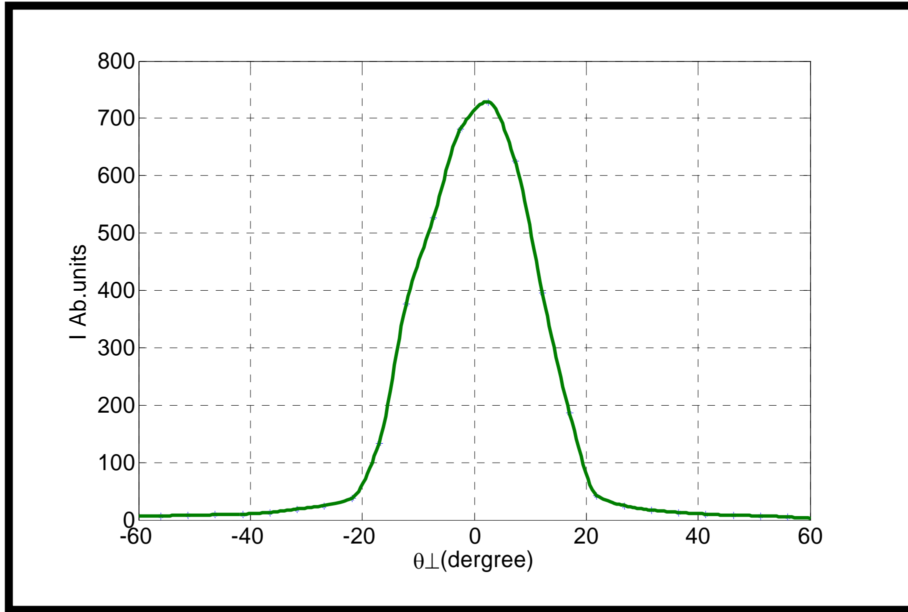

Fig.(5.40) The intensity profile vs. vertical beam divergence at a maximum power of 873 mW.

Fig.(5.41) shows the horizontal beam divergence and from this fitted figure the beam divergence was measured to be approximately equal to 8° at an emitting power of 873 mW, which is very close to that given by the company. Examining the spatial profiles of the QW diode laser in comparing to that of the bulk diode laser it can be seen that the spatial profile of the QW laser is smoother than that of the bulk and contains no spikes.

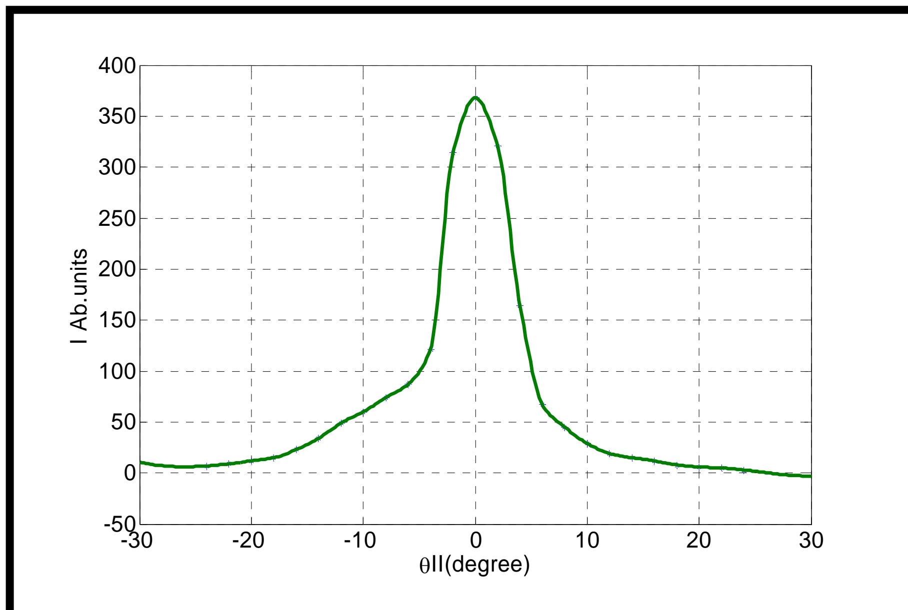

Fig.(5.41) The intensity profile vs. the horizontal beam divergence at a maximum power of 873mW

5.4.3 Laser Output Performance and Measurements:

In this section the laser output performance is investigated using the two pumping schemes of direct face- pumping (pulsed operation), and V-shape pumping in both CW and pulsed modes.

5.4.3.1 Direct Face Pumping (Pulsed Operation):

Using the pumping configuration proposed in chapter three for direct face pumping see Fig.(4.12) using internally triggered bulk diode laser at a repetition rate of 1.3kHz which gives the maximum emitted power see Fig.(5.34). Fig.(5.42) shows the relation between the driving current and the power emitted from the disk medium with and without the output coupler on R=90% and ROC=400mm at a fixed repetition rate of 1.3kHz (internal triggering) and resonator length of L=10cm. The first curve (circles) represents the fluorescence output from the Nd:YVO_4 disk medium while the second curve (squares) represents the 1064nm output laser from the system using the mirror with R=90%.

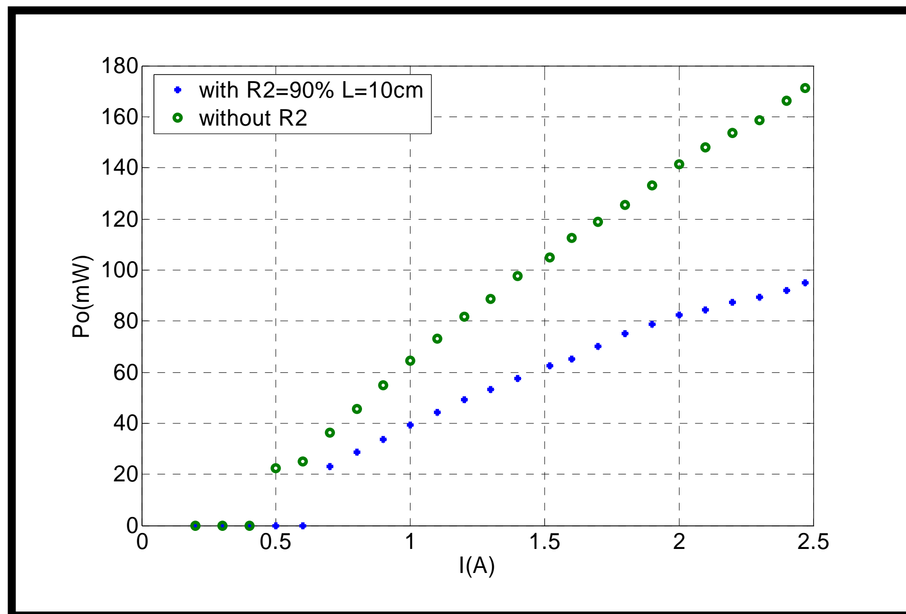

Fig.(5.42) Pumping current vs. the power at prf=1.3kHz

Fig.(5.43) is a relation between the peak pumping power (Pin)emitted from the bulk diode laser and the power emitted from the disk medium with and without the output coupler. From these two curves figures it can be seen that the maximum peak power gained from this system (with output coupler) was found to be ≈100mW at a fixed peak pumping power of 1030mw and the value of the threshold peak power was found to be Pth ≈41mW.

The reason for the decrease in the power due to the extraction efficiency of system which is related to the mirror reflectivity and the resonator loss.

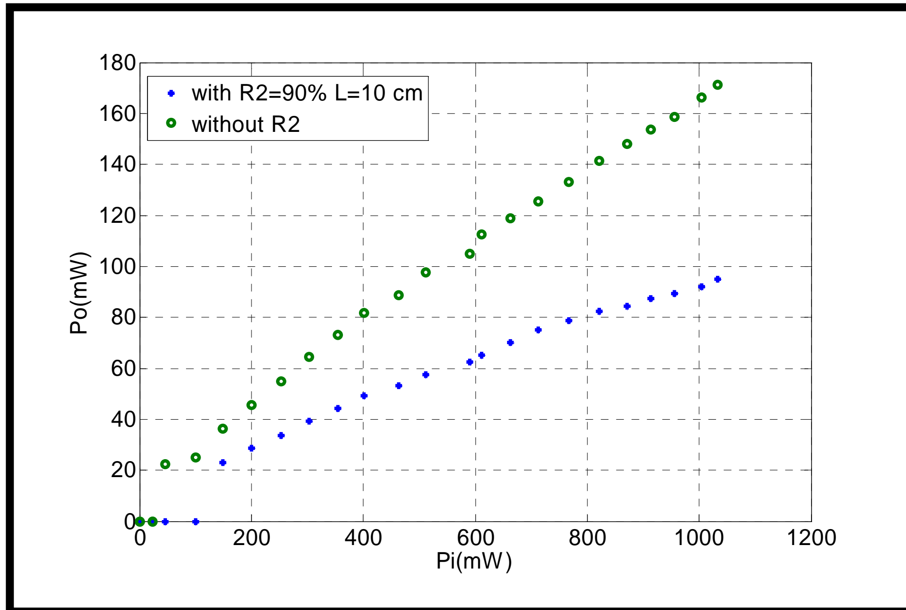

Fig.(5.43) Pumping power vs. the output power at prf=1.3kHz.

With varying the resonator length L between (10, 13.5, and 17.5 cm), the output laser power of wavelength 1064nm is recorded and a graph between the driving current of the internally triggered bulk diode laser at prf=1.3kHz and the laser output peak power is shown in Fig.(5.44) below

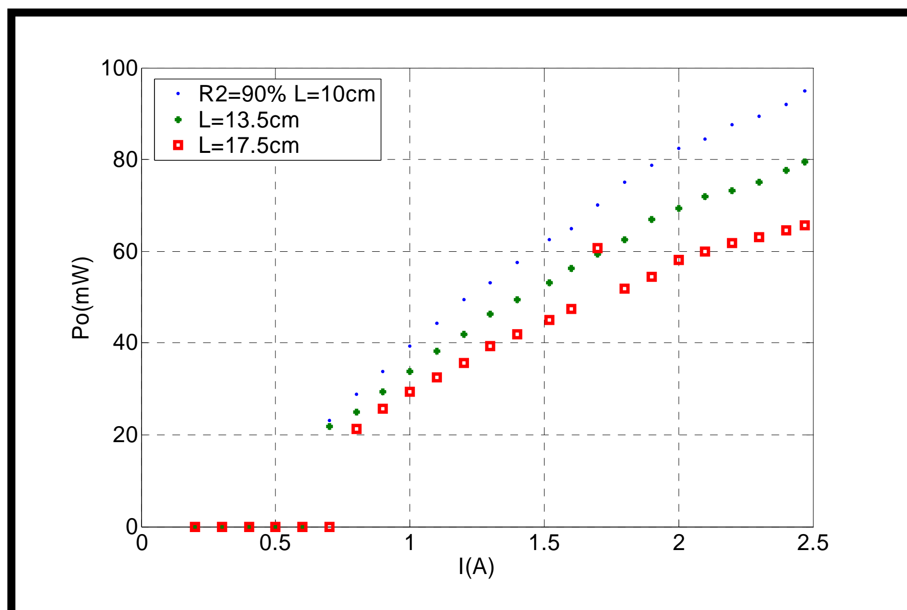

Fig.(5.44) Driving current vs. the laser output peak power at different resonator lengths.

Fig.(5.45) shows the relation between the peak pumping power and the peak output laser power using internal triggering of repetition rate 1.3kHz using an output coupler of R=90% with different resonator lengths. From the curves it was found that Pth is increased with increased resonator length.

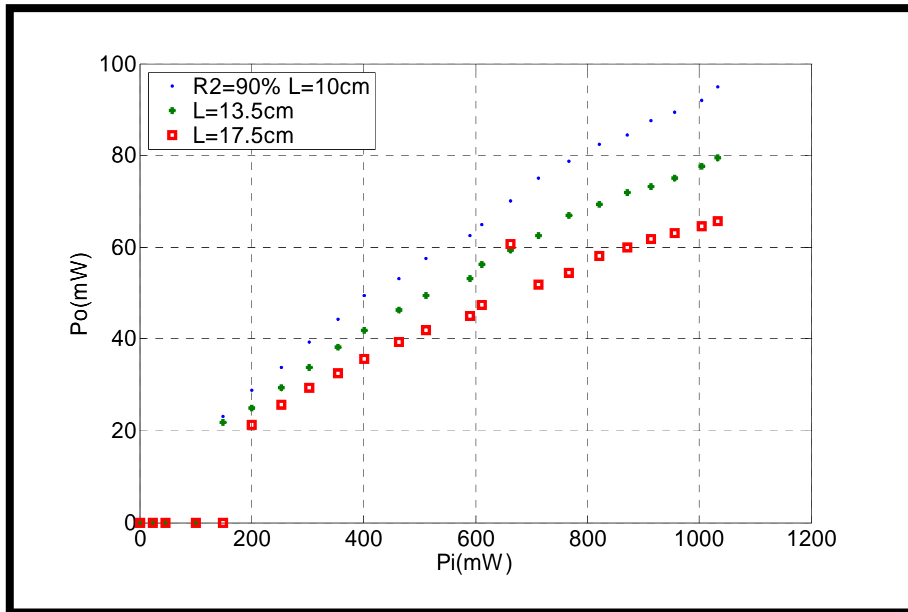

Fig.(5.45) The peak pumping power vs. the laser output peak power at different resonator lengths

The relation between the operating current and the laser output peak power at a resonator length of L=13.5cm, as it is known there is an optimum value for the output coupler reflectivity which maximizes the obtained output power, so using different mirror reflectivities (R=99%,90%,30%) will give different output powers at the same pumping power. It was found from the curves that the maximum output peak power is obtained at R=90%, as shown in Fig.(5.46)

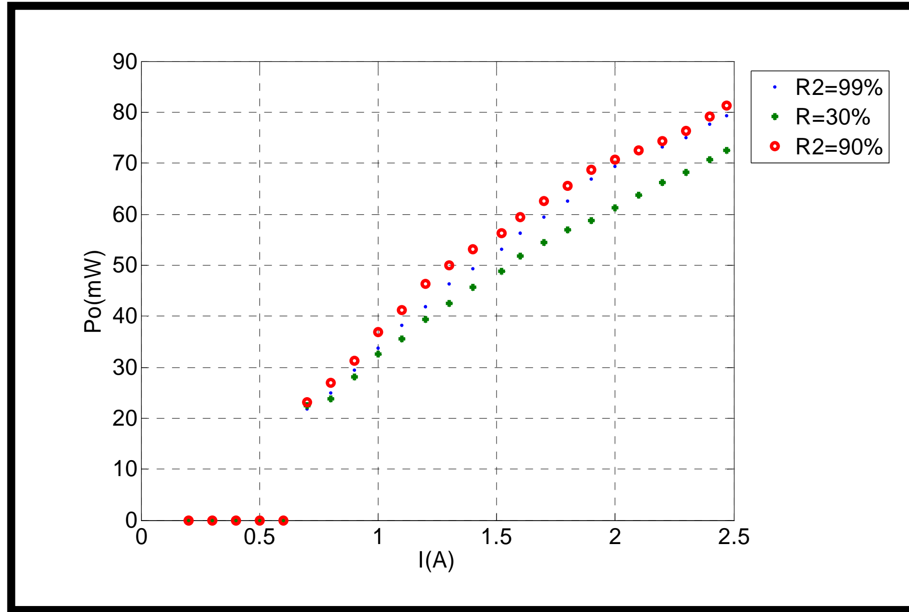

Fig.(5.46) The driving current vs. the peak laser output power at different reflectivities, L=13.5 cm.

Fig.(5.47) is the graph between the peak pumping power from the bulk diode laser and the output gained laser peak power. From this figure the maxium peak output power obtained was approximately 82 mW at R=90% and L=13.5 cm.

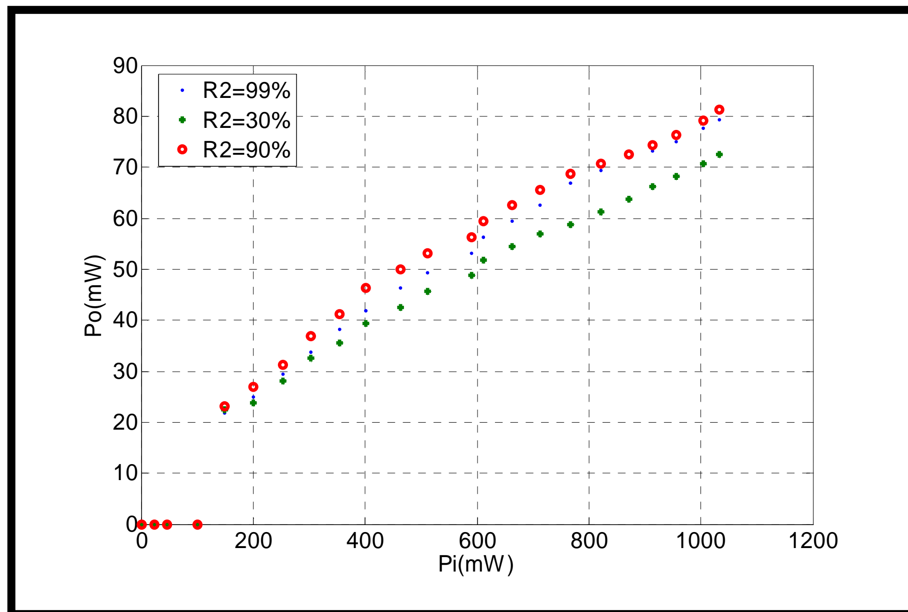

Fig.(4.47) Peak pumping power vs. the peak output laser power at different reflectivities, L=13.5 cm.

Fig.(5.48) shows the relation between the threshold pumping peak power and the logarithmic loss of the output coupler at a fixed resonator length. From this figure it is found that the internal resonator loss from intercepting with the y-axis ≈0.16. The

maximum P_{th} was measured to be ≈45mW at R=30%, and the lower threshold power was found to be ≈39mW at R=99%.

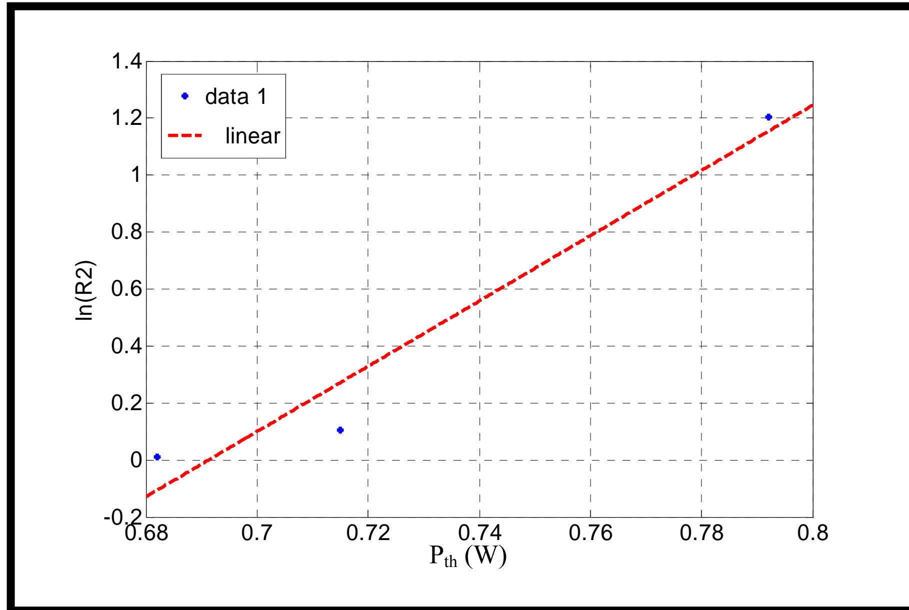

Fig.(5.48) The threshold peak power vs. the logarithmic coupling loss.

The relation between the operating current and the peak pumping power of the bulk diode laser transmitted from the two focusing lenses of focal lengths (f=5, 4.5 cm) is shown in Fig.(5.49). The second curve is drawn between the operating current and the peak power obtained after the highly transmissive mirror placed at 45°.

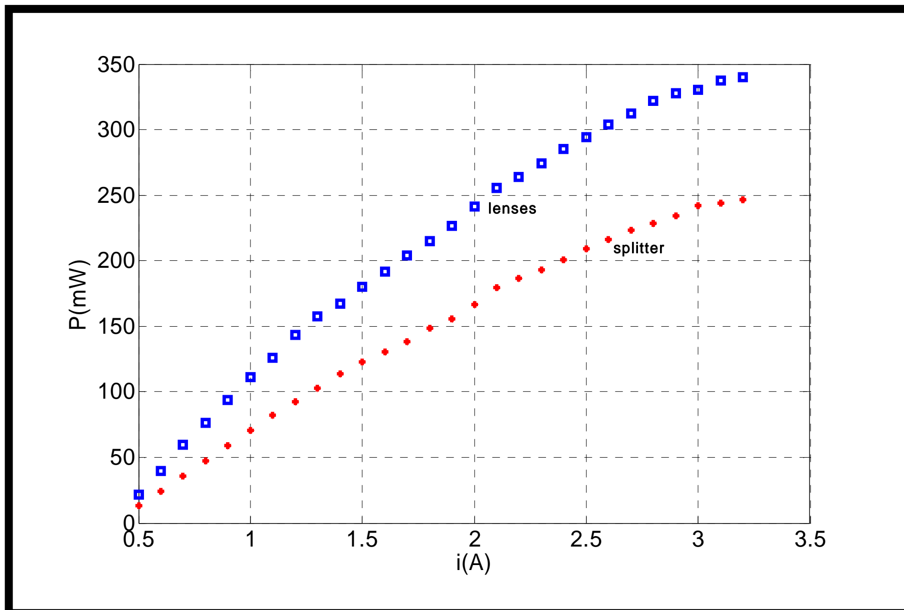

Fig.(5.49) The diode laser current vs. the power transmitted from the focusing lenses and the splitter .

From the first curve it was found that the measured transfer efficiency η_t from these two lenses that are used to focus the pumping spot on to the disk medium to achieve a pumping spot of d≈4mm equals to 28% which is relatively small due to the fact that it is not antireflection coated.

The slope efficiency which is calculated as the ratio of the output power to the pumping power after the splitter was found to be (36.5%, 35.5%, and 32.5%) at a mirror reflectivity of (90%, 30%, and high), respectively, and at a resonator length of 13.5 cm.

While for a mirror reflectivity of 90% with different resonator lengths of (10, 13.5, 17.5) cm, the slope efficiency are found to be (42.6%, 37.1%, 17.5%), respectively.

Due to the fact that decreasing the repetition rate of the bulk diode laser will increase the emitted peak power from it, and since this laser unit has the opportunity to be internally triggered. So the same system configuration was used but with internally triggered bulk diode laser this time (below 1kHz), and the effect of such change is investigated. It is necessary to mention that the duty cycle D.C. in external triggering can not be changed unlike the case of internal triggering.

Operating at a current of i=3.2A, temperature of 18.1°C and duty cycle D.C.=7.69, Fig.(5.50) shows the graph between the repetition rate and the energy obtained from the bulk laser diode using external triggering. It is obvious from the fitted data that the laser diode peak power decreases with increasing repetition rate, hence it is expected that decreasing the repetition rate will increase the output laser peak power obtained from the system.

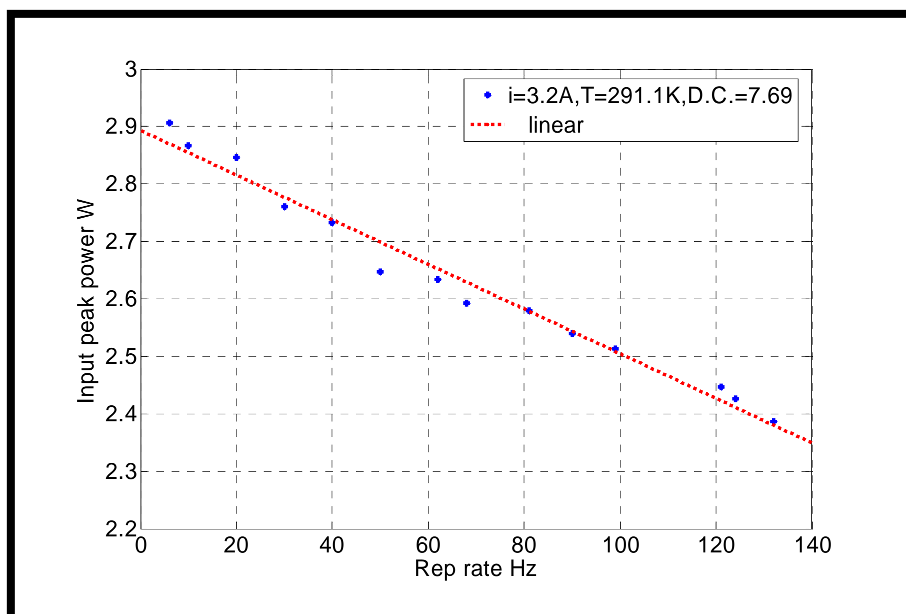

Fig.(5.50) The repetition rate vs. the emitted peak power from the bulk diode laser.

The effect of the operating temperature on the output power was investigated, Fig.(5.51) shows the relation between the operating current of the bulk diode laser externally triggered at repetition rate of 3Hz and the output laser peak power with a resonator length of L=10cm at different operating temperatures.

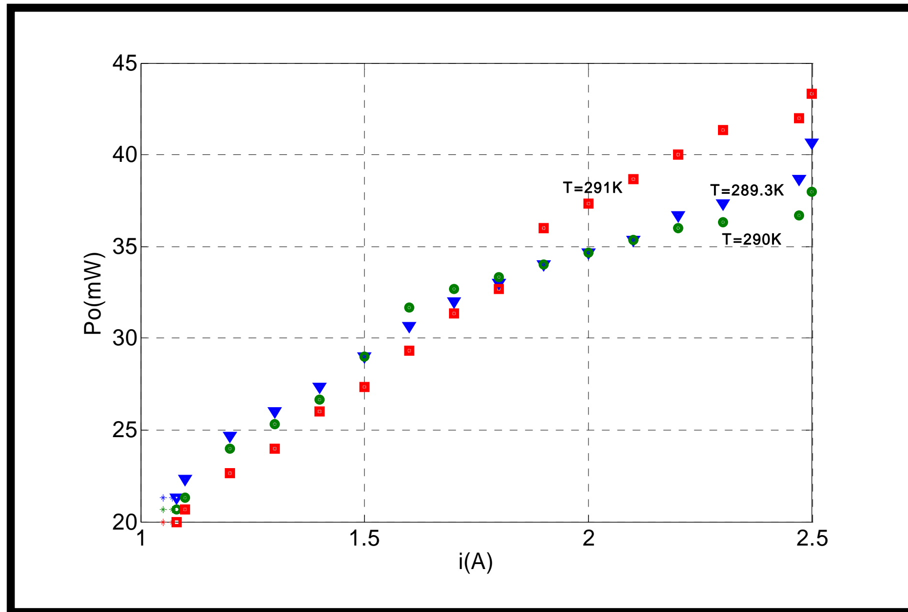

Fig.(5.51) The current vs. the laser output peak power at different operating temperature, L=10 cm, prf=3Hz.

It was found that lowering the temperature of the diode laser increases the peak pumping power obtained from it but this will lead to a shift in the emission wavelength of the diode laser, i.e. reducing the portion of the absorbed power hence reducing the laser output peak power of the system, so there is a compromise between T, Pin, Po.

Fig.(5.52) shows the relation between the operating current of the diode laser in external triggering and the obtained laser output peak power at different repetition rates using L=10cm. From the measured values of the laser output peak power as it was expected that reducing repetition rate will increase the obtained pumping power from the diode laser hence the laser output peak power, but far from the expected it is found that maximum output peak power was found at repetition rates of 45, and 50Hz.

The maximum output power was found to be 150 mW, at a repetition rate of 50 Hz, and the slope efficiency was found to be 66.6%.

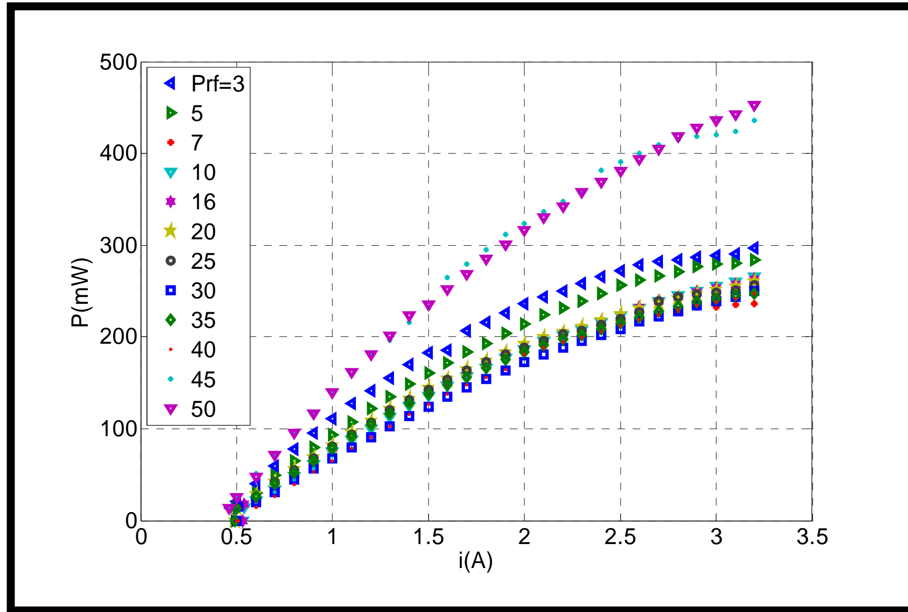

Fig.(5.52) The current vs. the output laser peak power at different repetition rates, L=10 cm.

5.4.3.2 V-shape face pumping:

Using the pumping configuration in chapter three that are proposed for V-shape laser, see Fig.(4.13), once the pumping source used was the 808 nm bulk diode laser operating in CW mode and also the 810nm QW GaAlAs diode laser was also used and a comparison between the two sources using the same pumping configuration was made as shown below:

Using the bulk diode laser, Fig.(5.53) shows a graph between the operating current and the transmitted power from the focusing lens with f=6cm. From this curve the measured radiation transfer efficiency is found to be η_r=53%. The second curve is drawn between the operating current and the radiation emitted from the disk medium. From this curve the measured value for the both the upper state efficiency and the absorption efficiency is found to be $\eta_u \eta_a$=7%.

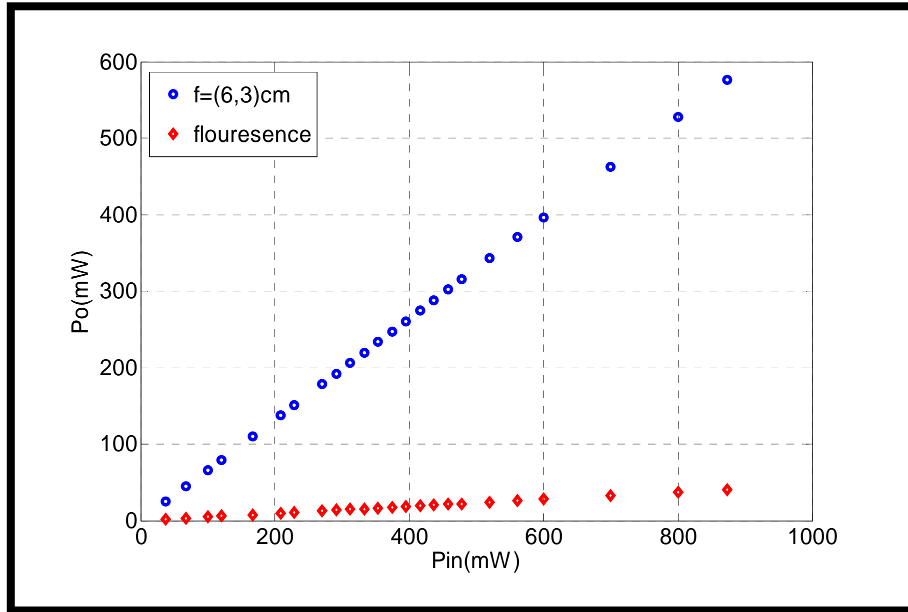

Fig.(4.53) The operating current vs. the transmitted power.

Fig.(5.54) shows the relation between the operating current of the bulk diode laser and the 1064nm CW laser output power at resonator length of L=13 cm.

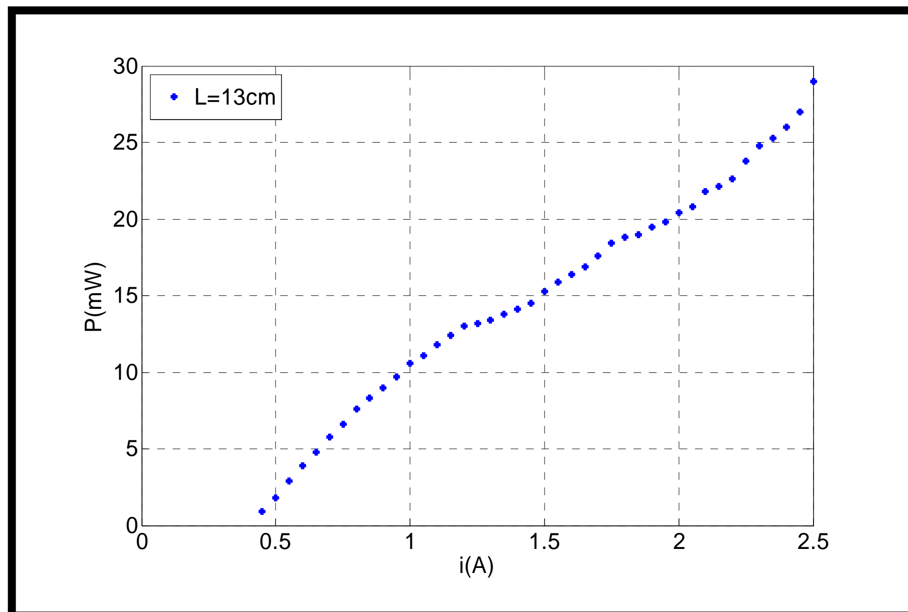

Fig.(5.54) The current vs. the laser output power at L=13 cm

From this graph it is found that the maximum output power obtained is 29mW, the measured optical to optical slop efficiency $\eta_{o\text{-}o}$=1.7%, and the measured threshold power P_{th} is found to be ≈25mW.

The slope efficiency is found to be 5.13%, with a maximum output power of 29 mW, at a pumping power of 1800 mW.

Now using the QW diode laser as a pumping source instead of the bulk one, two focusing lenses of focal lengths f=(6,3) cm are used to focus the rhombic spot of the QW diode laser onto circular spot of d=4mm in order to occupy the whole face of the disk which is allowed to be pumped. The relation between the pumping power and the transmitted power is shown in Fig.(5.55).

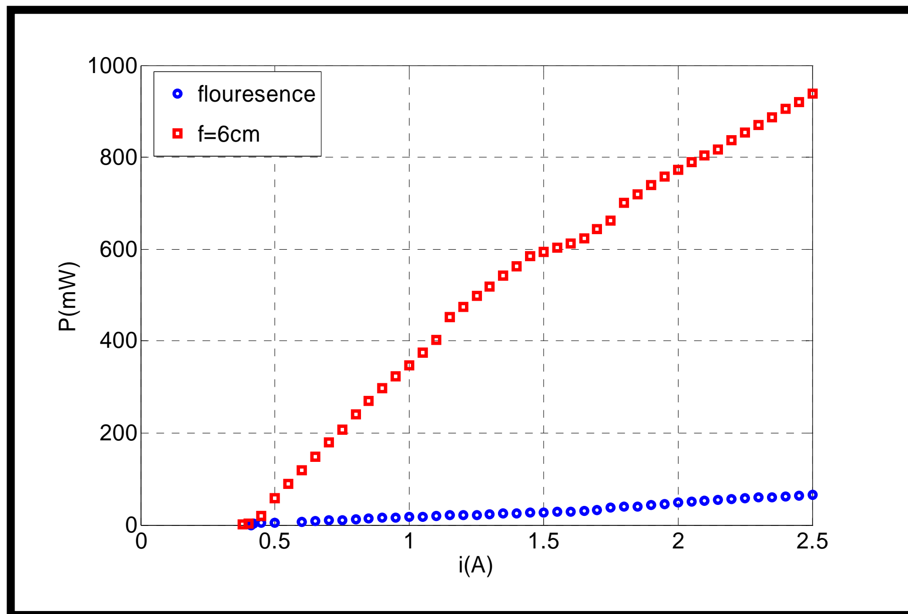

Fig.(5.55) The pumping power vs. the transmitted power.

From this graph the radiation transfer efficiency measured is found to be ≈67%, while the fluorescence curve is drawn between the operating current of the QW diode laser and the power emitted from the disk medium and the measured efficiency is found to be $\eta_u\eta_a$=7%.

The relation between the pumping power from the QW diode laser and the obtained 1064 nm laser output power using an output coupler of R=90% with different resonator lengths is shown in Fig(5.56) below:

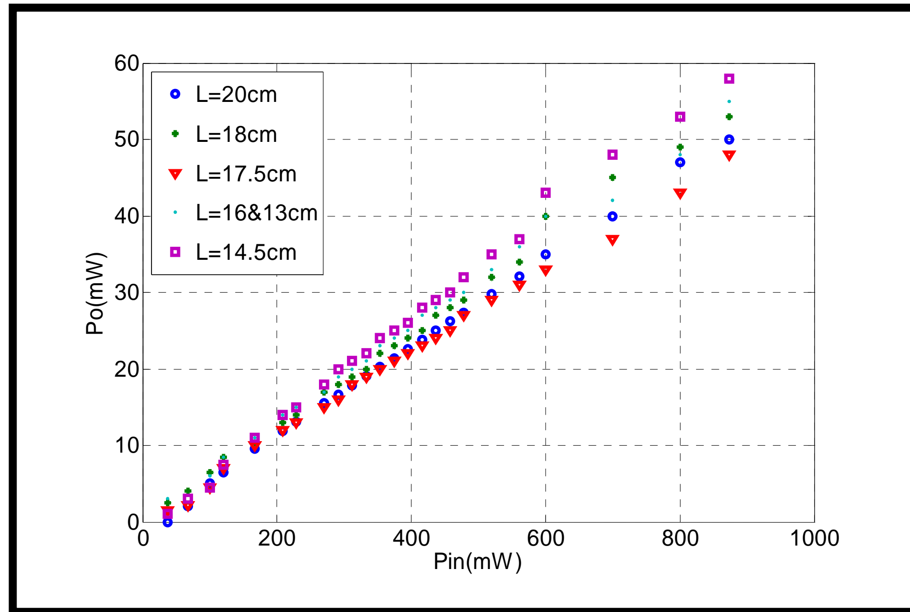

Fig.(5.56) The pumping power vs. the laser output power at different resonator lengths

From the above figure it is found that the maximum output power obtained at L=14.5cm and the measured threshold power is found to be P_{th}=37mW, the maximum output power obtained from this configuration is found to be =58mW. From this curve the maximum measured optical to optical slope efficiency is found to be ≈7% which is higher than that of the bulk diode laser. The slope efficiency is calculated to be 11.3%.

In pulsed operation the internally triggered bulk diode laser was used as the pumping source with a repetition rate of 1.3kHz. The influence of the laser diode operating temperature on the laser output power is investigated as shown in Fig.(5.57).

From the figure below again there is a compromise between the operating temperature T, the input peak power Pin, and the output laser peak power Po, it was found that the maximum output peak power was obtained at T=16°C, the measured threshold peak powers were found to be P_{th}≈713mW , 690mW, 665mW, for operating temperatures of T=20, 18, 16°C respectively, i.e. the measured threshold peak power is increased with increasing the operating temperature of the diode laser at a fixed resonator length of L=13cm, from these values the maximum optical to optical slope efficiency η_{o-o} was approximately equal to 1%. The maximum output power was achieved at an operating temperature of 16°C, which equals to 40 mW. The slope efficiency attained at different operating temperatures of (20, 18, 16) °C, were found to be (16.2, 16.7, 18) %, respectively.

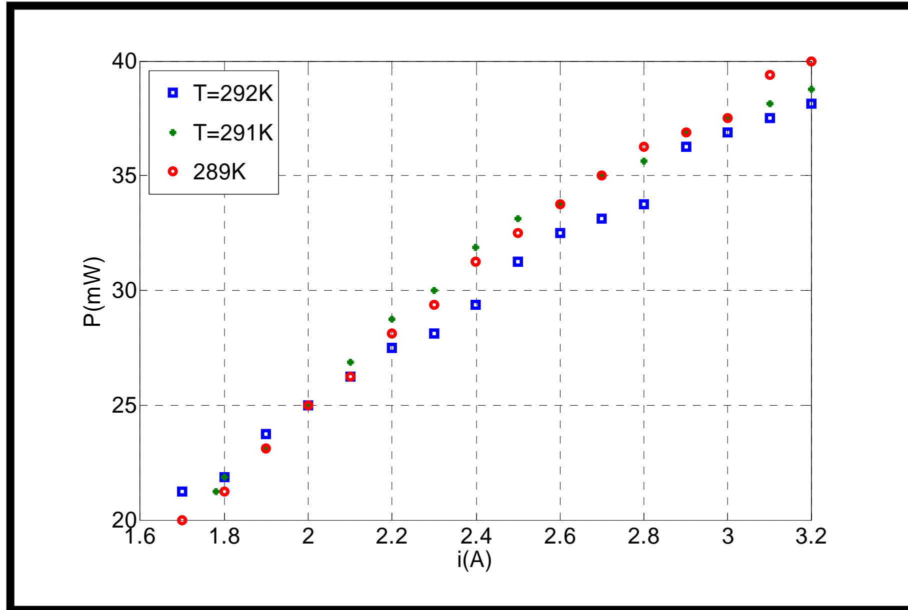

Fig.(5.57) The current vs. the laser output power at L=13 cm.

Now the bulk diode laser is externally triggered at different repetition rates (<1kHz) in order to increase the pumping peak power emitted from this source and hence the output laser peak power, the influence of such change was investigated as shown in the following figures.

The focusing lens used was the same as that for internal triggering, so the transmitted peak power from this lens was found to be as shown in Fig.(5.58) below, a graph between the operating current of the bulk diode laser at prf=100Hz, the measured radiation transfer efficiency was found to be η_r=52%, it is obvious that the value of this efficiency is low because the lens used in the system was not anti-reflection coated at 808 nm, so a large amount of the pumped beam is lost due to reflection.

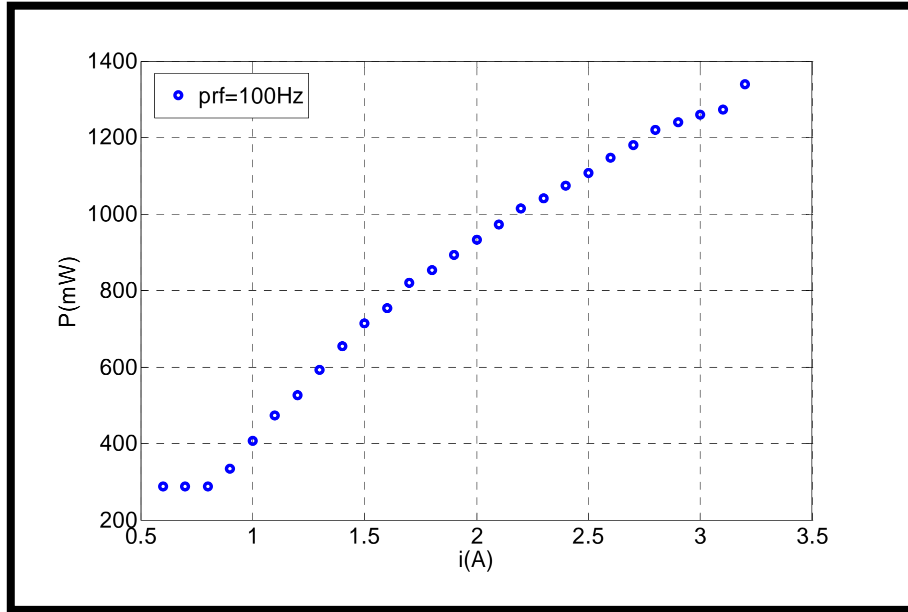

Fig.(5.58) The current vs. the transmitted pumping peak power

The influence of changing the repetition rate of the pumping source on the 1064 nm laser output peak power was investigated at a resonator length of L=13 cm as shown in Fig.(5.59) below:

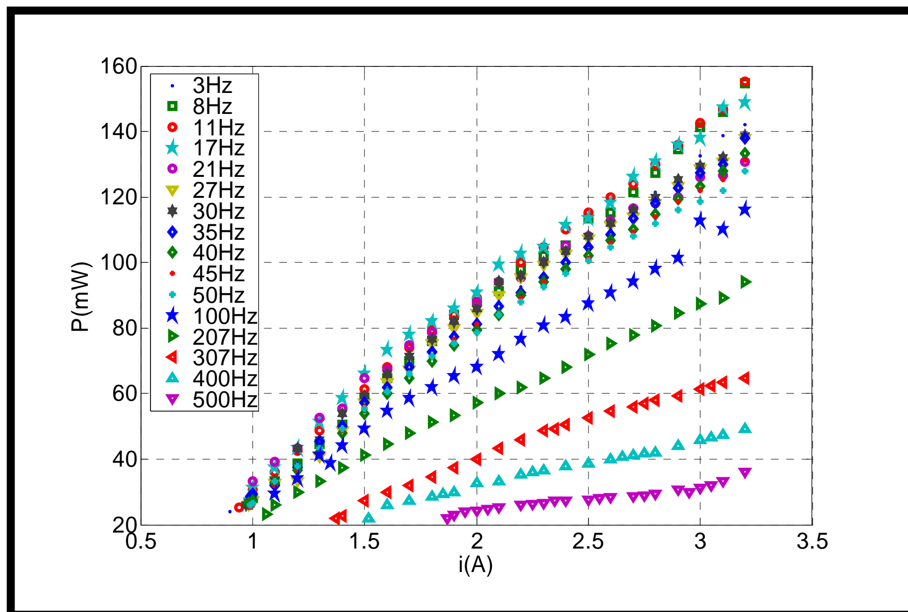

Fig.(5.59) The current vs. the laser output peak power at different repetition rates, using L=13cm.

From this figure the curves were drawn between the pumping current of the bulk diode laser and the 1064 nm laser output peak power with different repetition rates (3-

500)Hz, it was found that the maximum output peak power was obtained at repetition rate of 3Hz which was 155mW, and decreases with increasing repetition rate, due to the fact that decreasing the repetition rate will increase the value of the pumping peak power. Also the measured threshold peak power was increased with increasing repetition rate which was Pth=670mW to 1882mW for repetition rates of 3Hz to 500Hz, due to the fact that increasing the repetition rate will constrain the internal amplification inside the active medium.

The maximum optical to optical slope efficiency obtained for this pumping configuration was found to be 7% to 4.3% for repetition rates of 3Hz to 500Hz. while the slope efficiency of 71.4%.

The obtained values of the output power, threshold power, and slope efficiency from this work are compared with those values accomplished by other researchers as shown in table 6.1.

Table 6.1 comparison between the achieved experimental work and that achieved by other researchers.

Researcher name	***Year***	***Active medium type and shape***	***Dimensions***	***Pumping source and scheme***	P_{th} (mW)	P_o (mW)	η (%)
Muhammed K.Al-Ani,[30]	*2007*	*Nd:YVO$_4$ (Disc)*	*(4*5*1)mm*	*Bulk (CW), direct FP*	*3.5*	*600*	*56*
Adolf Giesen,[15]	*2005*	*Yb:YAG (Disc)*	*Φmm,(100-200)µm*	*V-shape*	*100W*	*500W*	*55*
Cartsen Langrock, et.al,[19].	*2002*	*Nd:YAG (rod)*	*Length 7.5mm*	*L-shape cavity*	*6.14W*	*150*	*6.4*
Christian Stewen, et.al,[28].	*2000*	*Yb:YAG (Disc)*	*Thickness 230 µm*	*V-shape*	*300W*	*647W*	*51*
Haider H.Suhail,[29]	*2000*	*Nd:YVO$_4$ (slab)*	*(3*3*1)mm*	*End pumping*	*35*	*239*	*30*
This work	*2008*	*Nd:YVO$_4$ (Disc)*	*(4*5*1)mm*	*Bulk (internal triggering), direct FP*	*41*	*95*	*42.6*
				Bulk (external trigeering), direct FP	*41*	*150*	*66.6*
				QW (CW), V-Shape	*37*	*58*	*11.3*
				Bulk (CW), V-Shape	*25*	*29*	*3.2*
				Bulk(internal triggering), V-shape	*665*	*40*	*18*
				Bulk (external trigeering), V-shape	*670*	*155*	*71.4*

5.1 Introduction:

This chapter consists of two parts: the first part includes the analytical and solution of some problems in bulk and QW (GaAs/AlGaAs) structures, and the differences between both structures.

Second part illustrates the result of the experimental work that is divided into two parts, first part shows the performance of direct face pumping of Nd:YVO_4 disc medium using 808 nm bulk diode laser internally and externally triggered, while second part shows the performance of face pumping using V-shape configuration of the Nd:YVO_4 disk medium using 810nm QW GaAlAs in CW mode in comparison to 808 nm bulk diode laser, operating once in CW mode and in pulsed mode (internally and externally triggered).

5.2 Theoretical Model Results:

In this section the results of the theoretical model are presented, which includes the results for the GaAs/AlGaAs bulk diode, and QW laser.

5.2.1 Characterization of GaAs/AlGaAs Bulk Diode Laser:

Fig.(5.1) shows the difference in probability between the stimulated emission and absorption with the transition energy which are plotted at different Fermi-level values. The condition of Bernard and Duraffourg which implies that Eg <=hν<=E_{Fc}-E_{Fv}, from this graph the value of f_c-f_v=0 gives zero gain which is the transparency condition.

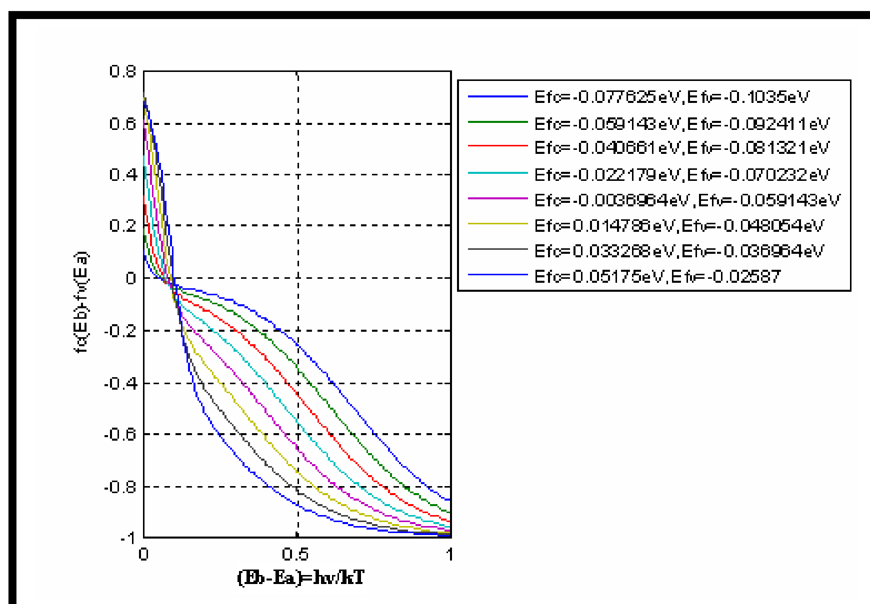

Fig.(5.1) Probability of transition vs. the normalized transition energy.

Fig.(5.2) shows the relation between the number density in upper level $N_u \sim f_c(E_c)\rho(E_c)$ plotted at different Fermi=energy levels.

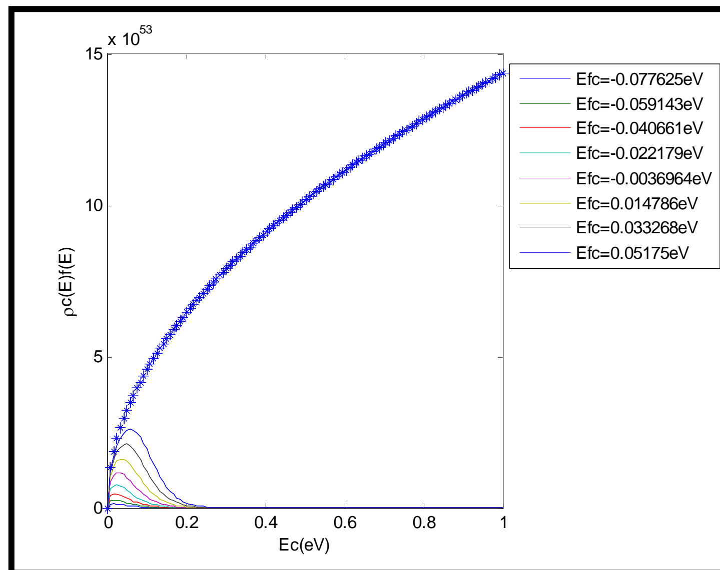

Fig.(5.2) Number density in upper level vs. the conduction band energy.

Fig.(5.3) shows the relation between the carrier density and the quasi-Fermi levels at different temperatures, this figure shows that reducing the temperature of the laser diode will result in a reduction in the density of injected carriers at the same value of the quasi-fermi level.

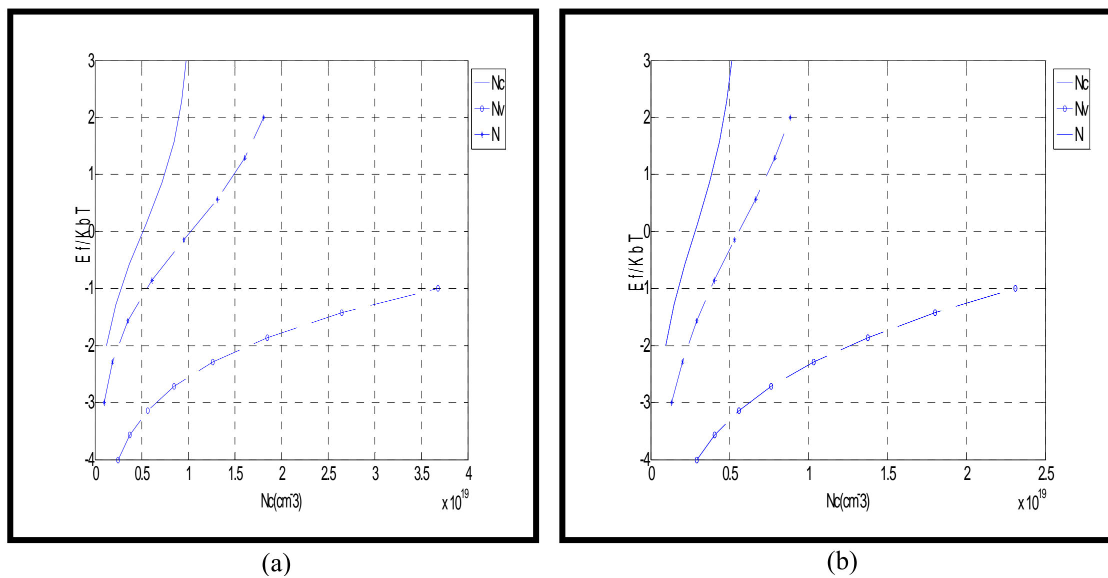

(a) (b)

Fig.(5.3) Normalized plots of the quasi- Fermi levels of both valence and conduction bands E_F/kT versus the concentration of injected carriers N at (a)T=300°K, (b)200 °K,

Fig.(5.4)shows the relation between the gain coefficient and photon energy, using the injected carrier density N as a parameter. One notes that, upon increasing the carrier

density, the difference in quasi-Fermi energy E_{Fc}-E_{Fv}, increases and this results in a corresponding increase in the gain bandwidth, even at the highest carrier injection this bandwidth is however a small fraction of the energy gap, for each plot increasing the injected carrier density will increase the peak gain, reduction of the operating temperature will result to a reduction in the gain bandwidth and a reduction in the value of the injected carrier density which produces transparency. Also a 3-D plot for the gain two temperatures 200°K, 300° is shown in Fig.(5.4, (a), (b)).

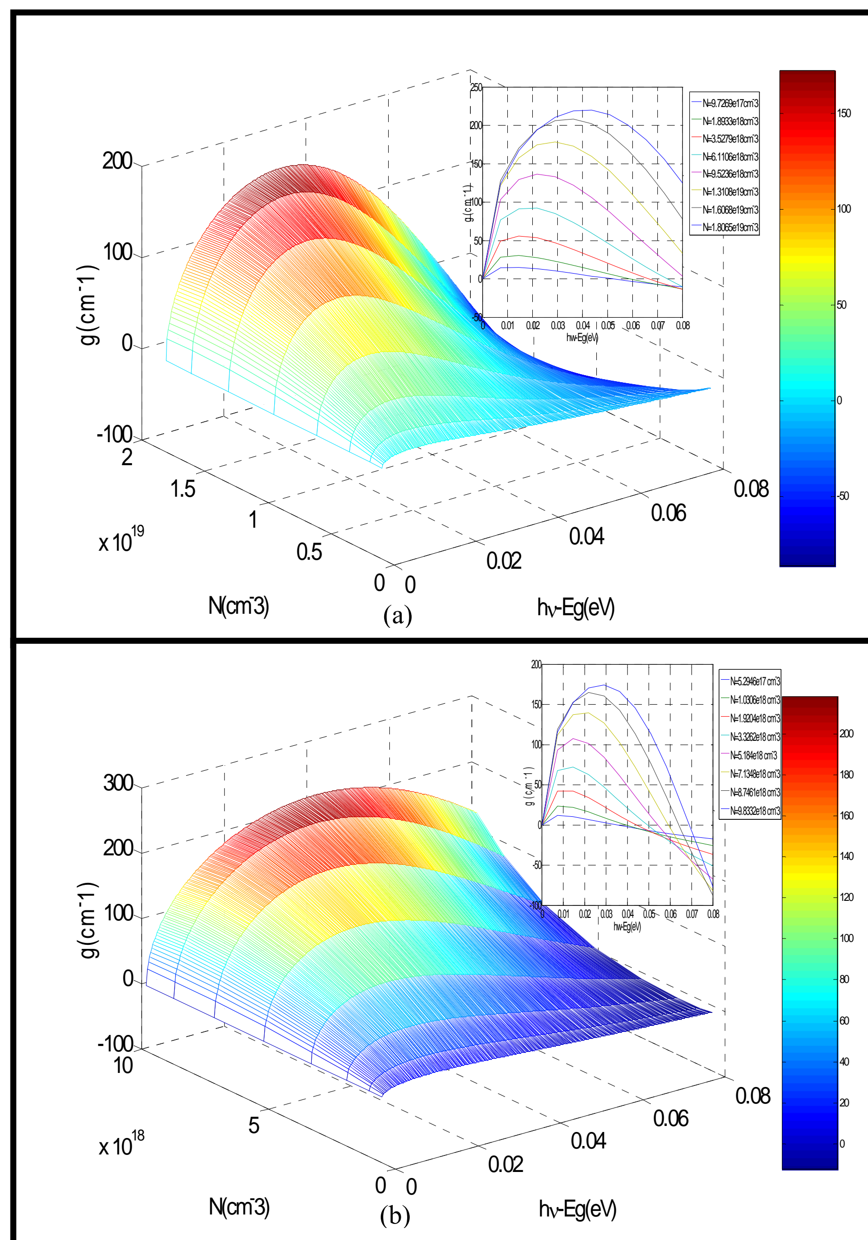

Fig.(5.4) 3-D plot of the gain, energy, carrier curve at (a)300°K, (b)200°K.

Fig.(5.5) shows a plot of peak gain coefficient versus the density of injected carriers at different temperatures, which can be approximated by a linear relation; $g_{max}=\sigma(N-N_{tr})$, where $\sigma=dg/dN$ is the differential gain, at T=300°K, Ntr=0.03e19cm^{-3}, and at T=200°K, N_{tr}=0.5e17cm^{-3} which means a reduction of more than 500 by reducing the operating temperature by 100°K, as indicated in each curve the differential gain coefficient will be increased by a factor of approximately 0.7.

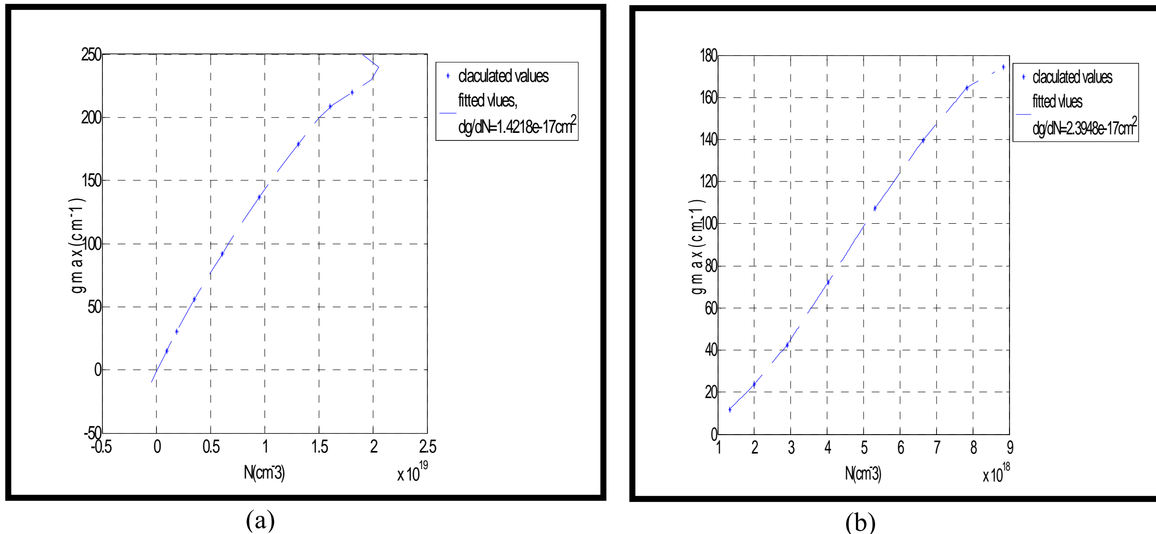

(a) (b)

Fig.(5.5) Plot of the peak gain coefficient versus the injected carrier density at (a)T=300°K, (b)200 °K,.

Fig.(5.6) is a plot of the threshold current density with the thickness of the active region with variable facet reflectivity, it can be seen that the increasing of the facet reflectivity will minimize the value of the threshold current density, while increasing the value of the thickness of the active region at fixed reflectivity will result in an increase in the value of the threshold current density, also reducing the operating temperature will result in a reduction in the value of the threshold current density by a factor of 1kA/cm^2 for the same value of the active region and R=0.32, while the reduction in the threshold current density for the coated facet is not very significant, i.e. coating the facet of the laser diode is very important.

A 3-D plot of the threshold current density versus the threshold carrier density and the active region thickness at a facet reflectivities of R=(0.32,0.8) at an operating temperature of T=300°K is shown in Fig.(5.7). Also the inset figure is drawn between the threshold current density and the threshold carrier density. From this figure it is obvious

that increasing the facet reflectivity will result in a decrease in both the threshold current density and the carrier density.

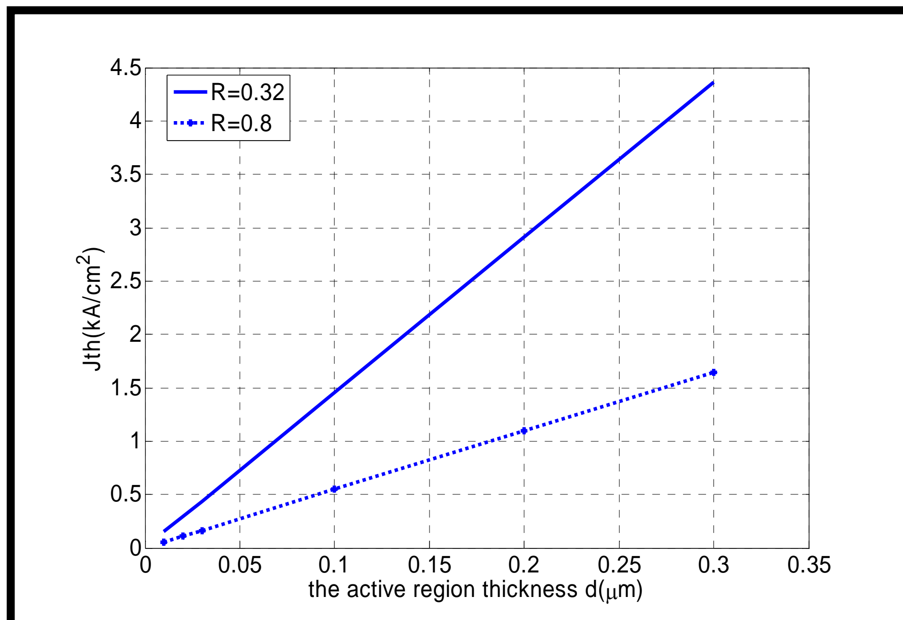

(a)

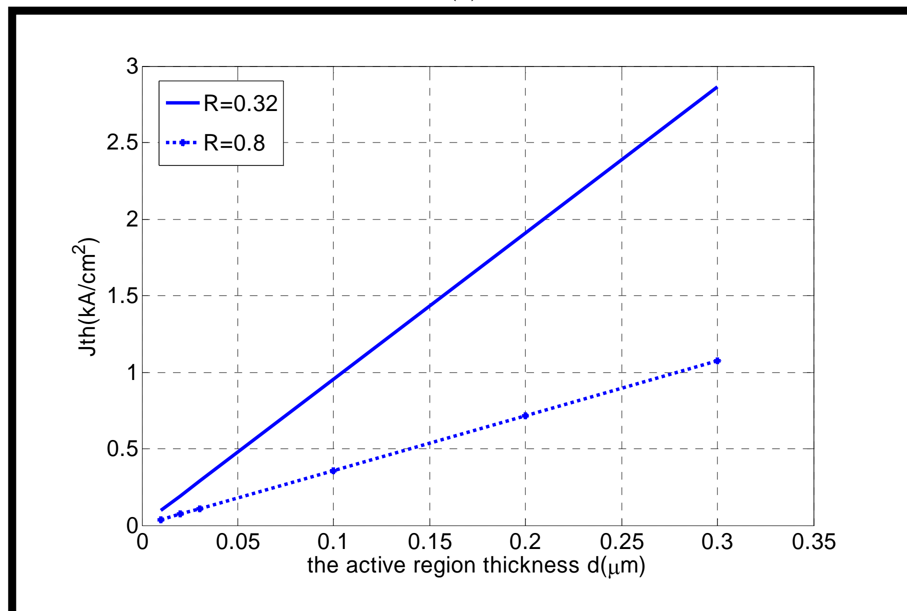

(b)

Fig.(5.6) Plot of the threshold current density versus the thickness of the active region at different output reflectivities for TE polarization, (a) 300°K, (b)200°K.

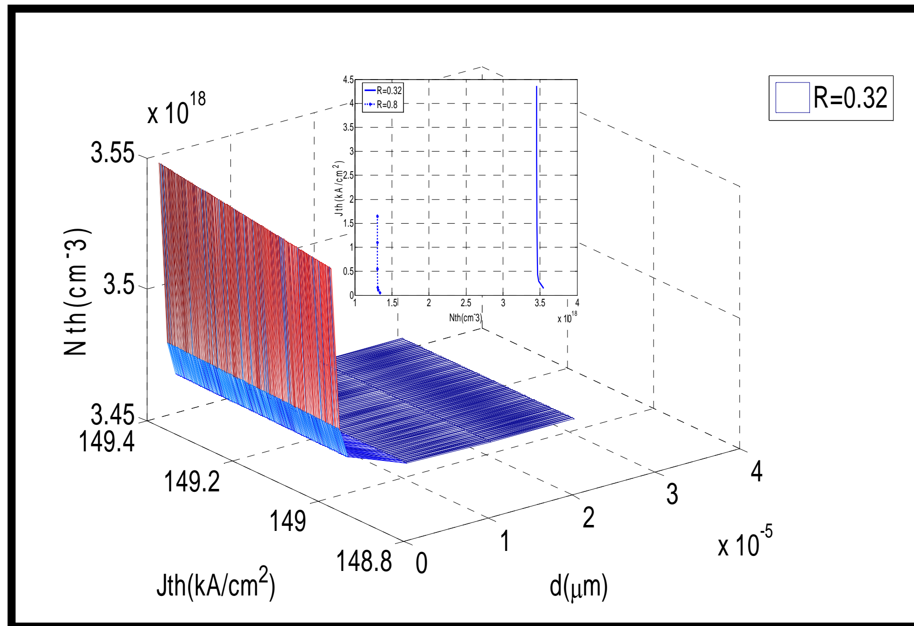

(a)

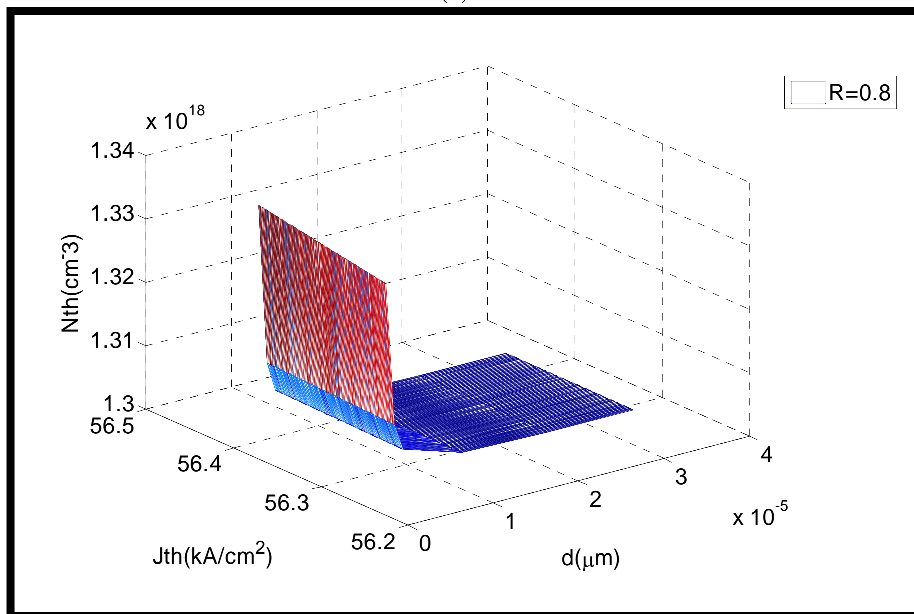

(b)

Fig.(5.7) 3-D plot of the threshold current vs. the threshold carrier density and the active region thickness at T=300°K, at facet reflectivity (a)R=0.32, (b)R=0.8.

Fig.(5.8) is a 3-D plot of the threshold current density versus the threshold carrier density and the active region thickness at a facet reflectivities of R=(0.32,0.8) at an operating temperature of T=200°K. From these two figures it can be seen that the same value of injected carrier density using the same value of the facet reflectivity will result in a reduction of 0.05kA/cm^2 in the threshold carrier density, and that the value of the

threshold current density will be minimized when the operating temperature is reduced from T=300°K to T=200°K.

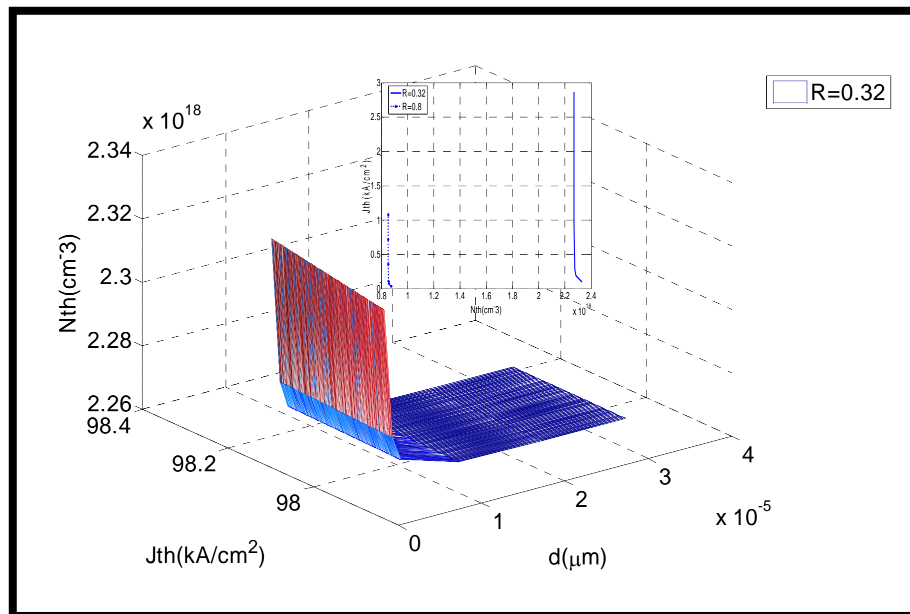

(a)

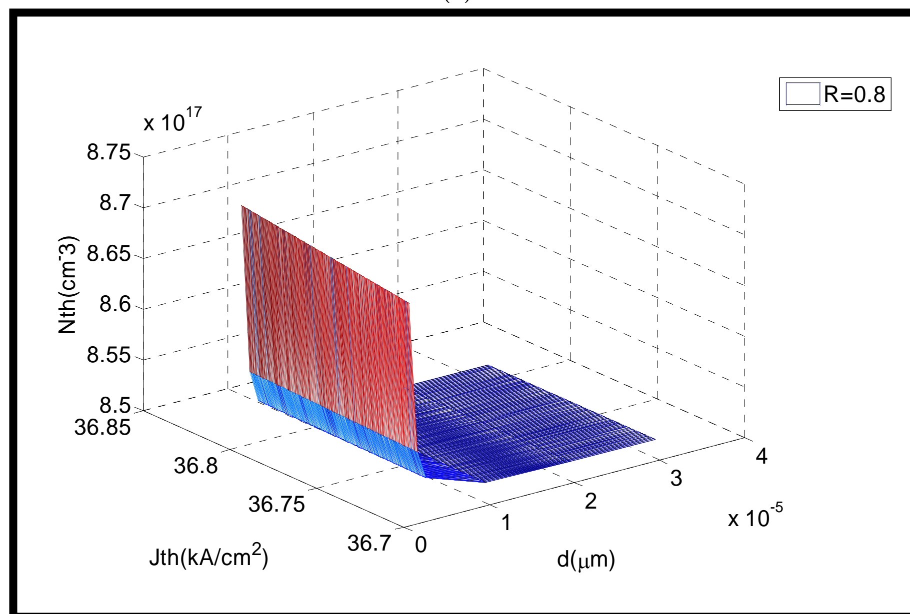

(b)

Fig.(5.8) 3-D plot of the threshold current vs. the threshold carrier density and the active region thickness at T=200°K, at facet reflectivity (a)R=0.32, (b)R=0.8.

Fig.(5.9, 5.10) is a relation between the injected current and the light output power at facet reflectivity of R=0.32 at operating temperature of T==300°K to T=200°K, respectively, at different stripe widths of s=(20, 40, 60, 80, 100)µm, from this figure the threshold current at T=300°K are 8.98mA, 17.7mA, 27mA, 36mA, 45mA, while at

T=200°K this values are found to be 6.5mA, 13.4 mA, 19.8 mA, 26.3mA, 33.2 mA, at stripe width values of s=(20, 40, 60, 80, 100)µm, respectively.

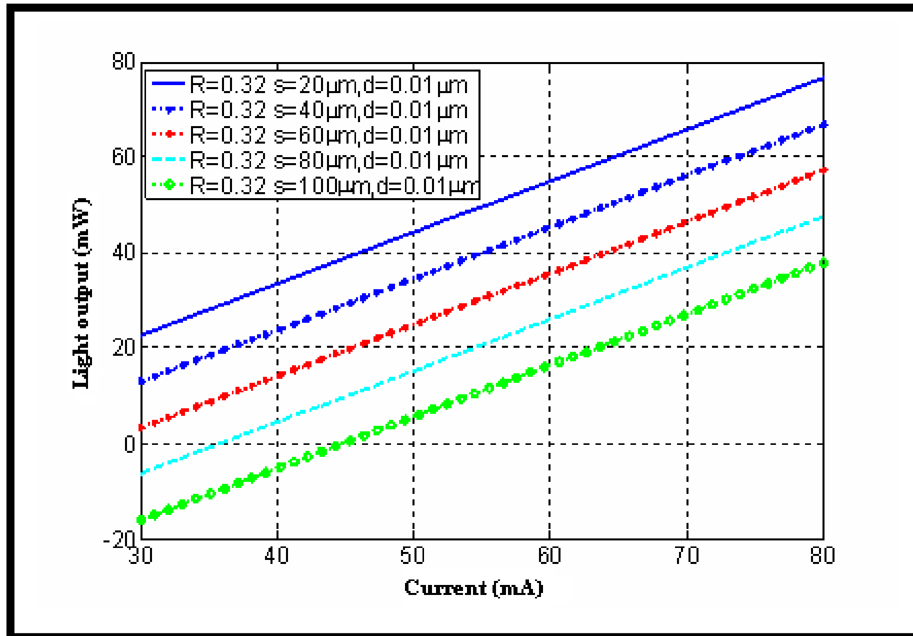

Fig.(5.9) Plot of the light output power versus the injection current at 300°K.

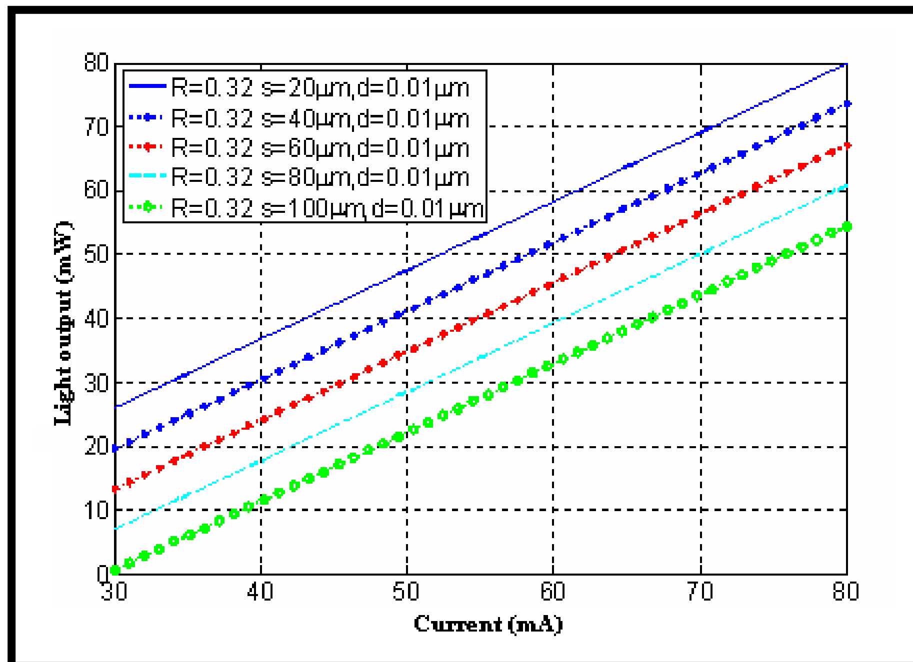

Fig.(5.10) Plot of the light output power versus the injection current at 200°K.

From the above two graphs the optical output power were found to be (78, 65, 58, 47, 39)mW, and (82, 73, 68, 62, 55)mW, these values were calculated at stripe widths of

s=(20, 40, 60, 80, 100)μm, and facet reflectivity of R=0.32 and two operating temperature of T=300 °K and T=200°K.

The relation between the injected current and the light output power at facet reflectivity of R=0.8 at operating temperature of T==300°K and T=200°K, respectively, at different stripe widths of s=(20, 40, 60, 80, 100)μm, is shown in Fig.(5.11, 5.12).

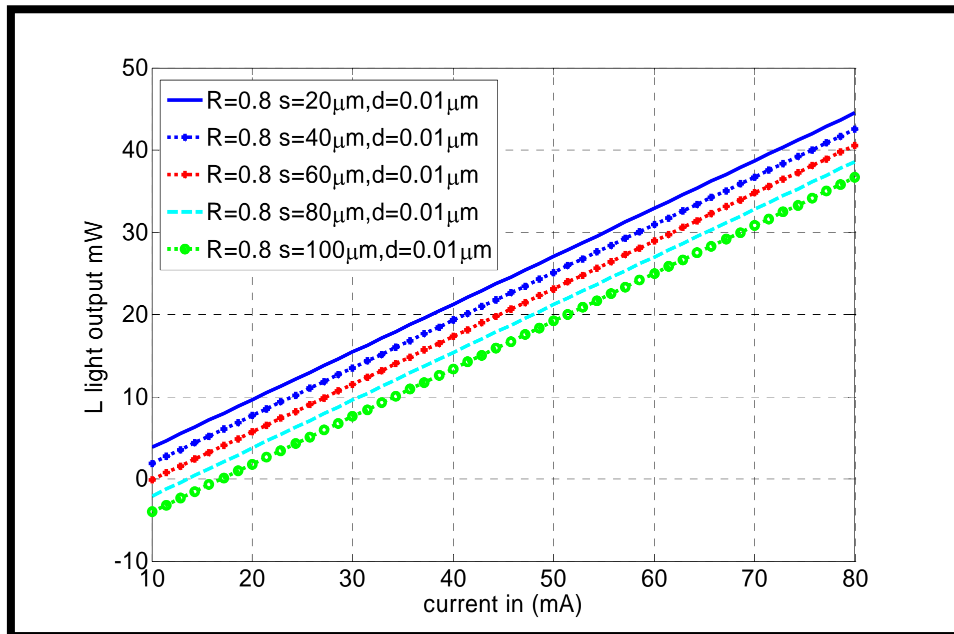

Fig.(5.11) Plot of the light output power versus the injection current at 300°K.

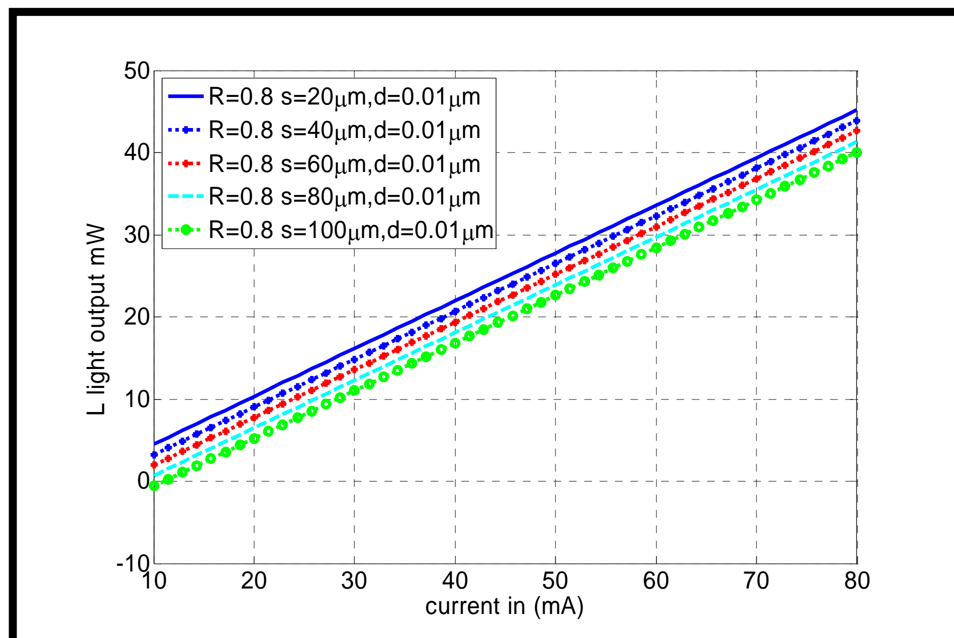

Fig.(5.12) Plot of the light output power versus the injection current at 200°K.

From the above two graphs , the threshold current at $T=300^{o}K$ are 3.42mA, 6.87mA, 6.87mA, 10.2mA, and 17.15 mA, while at $T=200^{o}K$ these values are found to be 3.6 mA, 6.2 mA, 10.4mA, 13.5 mA, and 16.6 mA, at stripe width values of s=(20, 40, 60, 80, 100)μm, respectively. The optical output power were found to be (44, 42, 40.5, 38, 37)mW, and (45, 44, 43, 41.5, 40)mW, these values were calculated at stripe widths of s=(20, 40, 60, 80, 100)μm, and facet reflectivity of R=0.8and two operating temperature of $T=300\ ^{o}K$ and $T=200^{o}K$.

It was found from examining these figures that there is a significant difference in the value of the threshold current, and the power obtained at the same pumping current results in a higher output power with reducing the operating temperature.

It is obvious from the above Fig.s(5.9, 10, 11, and 12), the value of the threshold current changes slowly when the facet reflectivity is high due to cooling in opposite to the case of R=0.32. Also the output power attained at the same injection current increases slightly when the operating temperature is reduced. This drives the attention that coating the facet will significantly reduces the threshold current but also slightly reduces the output power.

5.2.2 Characterization of GaAs/AlGaAs QW laser:

5.2.2.1 Spectral Gain- carrier density distribution:

The calculation of the peak modal gain requires a calculation of the spectral dependence of the modal gain, for a structure with a GaAs quantum well (100 Å). The modal gain has been calculated using the Fermi's-Golden Rule that is the product of the material gain coefficient times the optical confinement factor evaluated at the curve's spectral peak. Fig.(5.13a,b) represents the simplified gain model in which the spectral broadening effects as well as effects resulting from the anisotropy of the QW have been ignored. This curve is associated with a carrier density of $N=3.34*10^{18}cm^{-3}$ at $300^{o}K$. Note the sharp features arising from the low-energy heavy-hole transition, and the higher energy light-hole transition. The gain cross-over between the n=1 heavy and light-hole transition energies. The first figure was plotted against the transition wavelength, while the second was plotted against the transition energy.

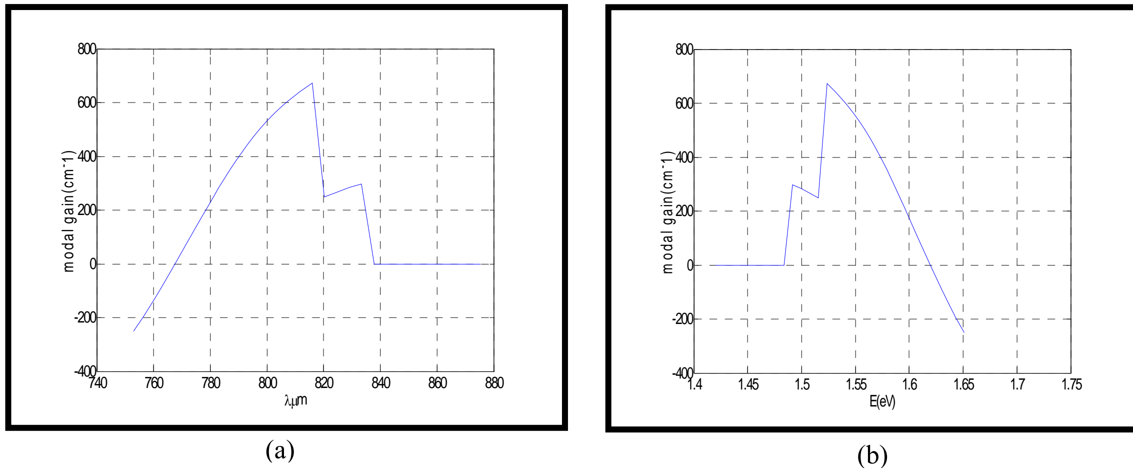

(a) (b)

Fig.(5.13) Plot of the modal gain versus (a) the transition wavelength, (b) the transition energy, at $T=300^{o}K$, $L_z=100$ Å.

Fig.(5.14a,b) is a 3D- plot of the modal gain versus the injected carrier density and the transition energy, the transition wavelength, respectively. It is obvious that increasing the carrier density will result in an increase in the value of the peak gain.

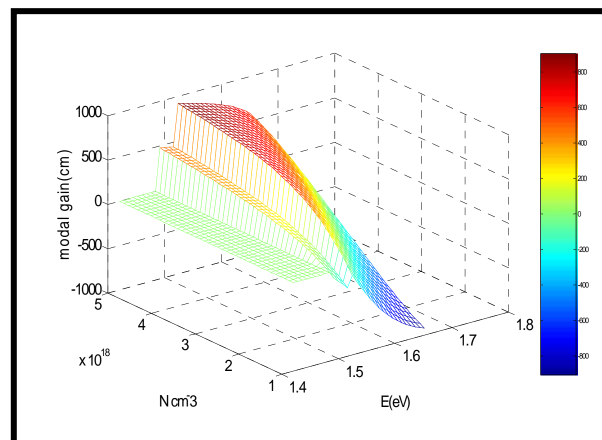

(a)

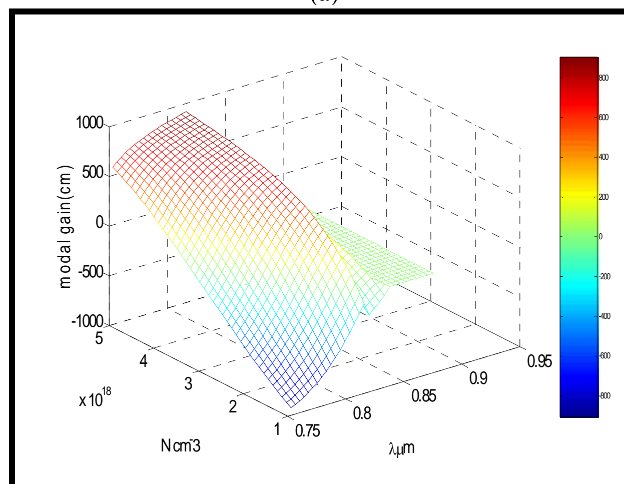

(b)

Fig.(5.14) 3D-plot of the modal gain and carrier density versus,
(a) transition energy, (b) transition wavelength.

The relation between the modal gain for the same injection condition, N=1.827e18, versus the wavelength transition and the transition energy, respectively, is shown in Fig.(5.15a, b), with TE and TM polarization enhancement, in which the feedback condition for lasing usually selects TE over TM polarization even when the gain is polarization-independent. The anisotropy factor in the QW provides an enhancement of the oscillator strength for TE polarization at photon energies near the gain peak as opposed to TM polrization, where the oscillator strength diminshed. Thus for QW structure, stability of lasing in the TE mode is improved further, and TM polarization need not to be considered.

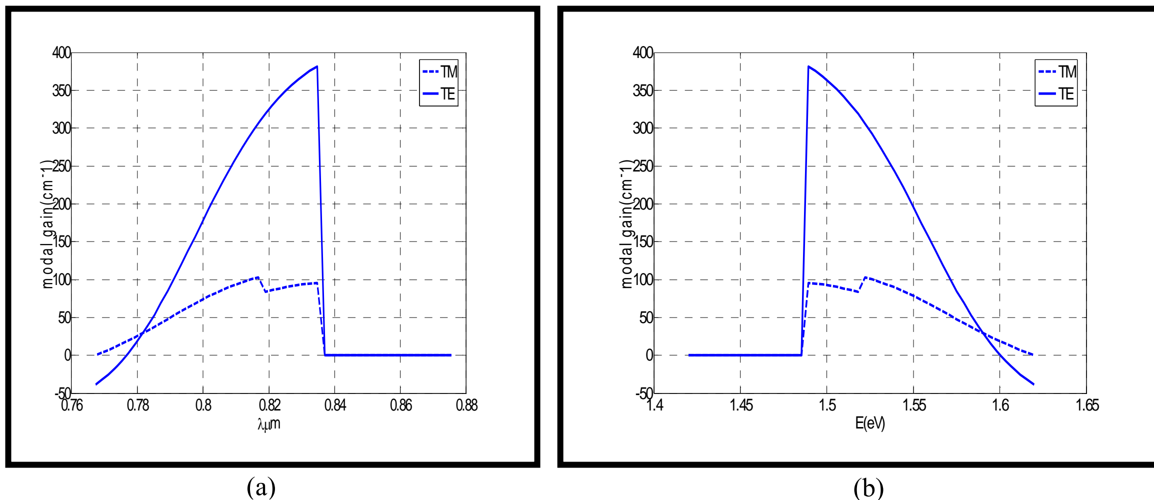

(a) (b)

Fig.(5.15) Plot of the TE and TM modal gain versus, (a) the transition wavelength, (b) the transition energy.

Fig.(5.16a,b) plot the modal gain for the same injection condition N=3.348e18cm^{-3}, versus the transition wavelength and transition energy, respectively. From the simplified model and the TE polarization enhancement, the planar symmetry of the electronic wavefunctions in a QW structure results in a polarization dependence of the stimulated optical transitions, which results in a difference between the dipole e-lh and e-hh.

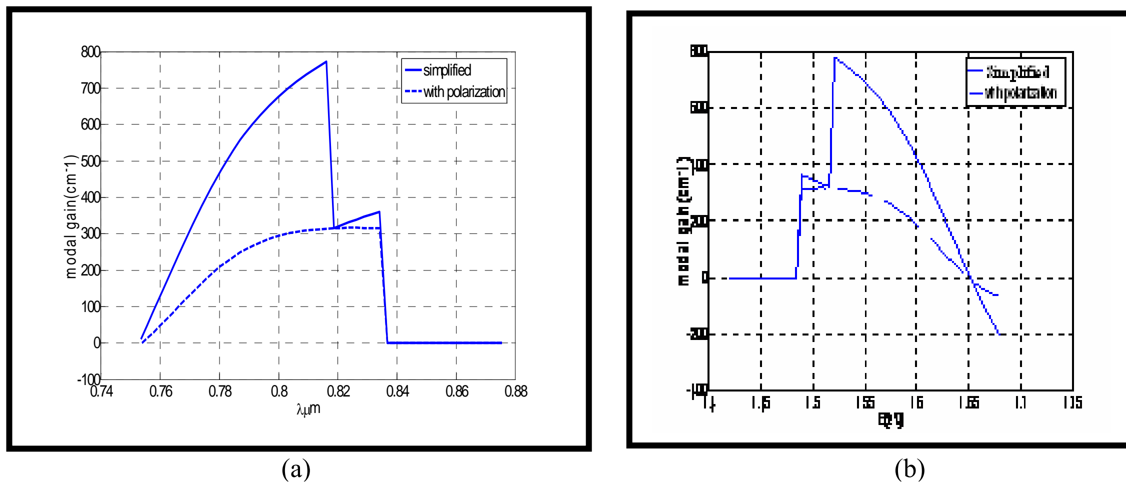

(a) (b)

Fig.(5.16) Plot of the modal gain versus (a) the transition wavelength, (b) the transition energy at Lz=100 Å.

Fig.(5.17) is a 3-D plot of the TE modal gain with carrier concentration and the transition wavelength, the transition energy, respectively. It can be seen that the peak gain is enhanced for TE polarization, and an overall diminshing effect is only observed at the high-energy tail of the gain spectrum.

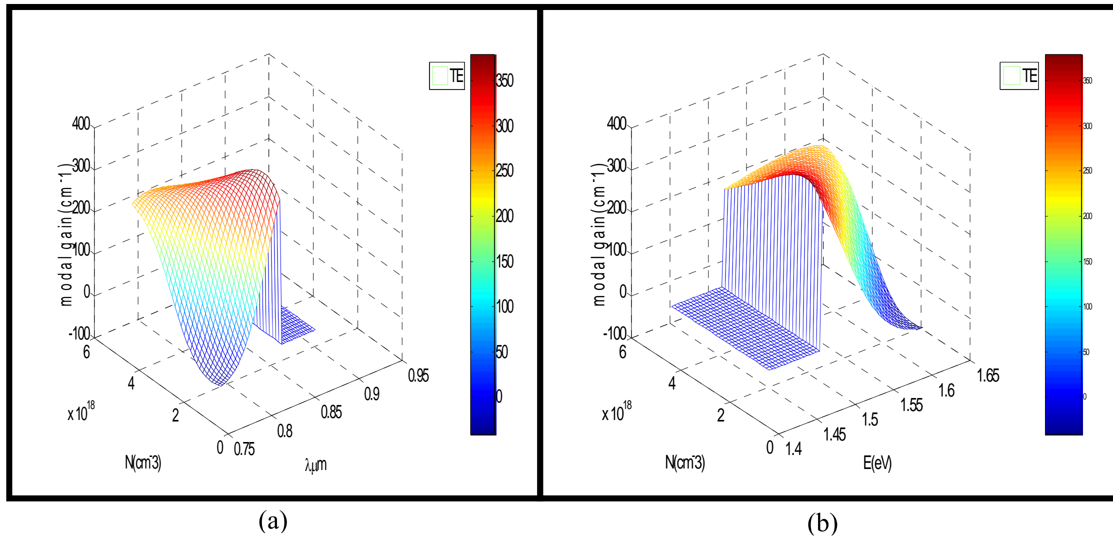

(a) (b)

Fig.(5.17) 3-D plot of the TE modal gain with the injected carrier density and, (a) the transition wavelength, (b) the transition energy

Fig.(5.18) is a 3-D plot of the TM modal gain with carrier concentration and the transition wavelength, the transition energy, respectively. The difference between the TM curve and the TE curve that the polarization enhancement of the TE modal gain is more obvious than that of the TM mode.

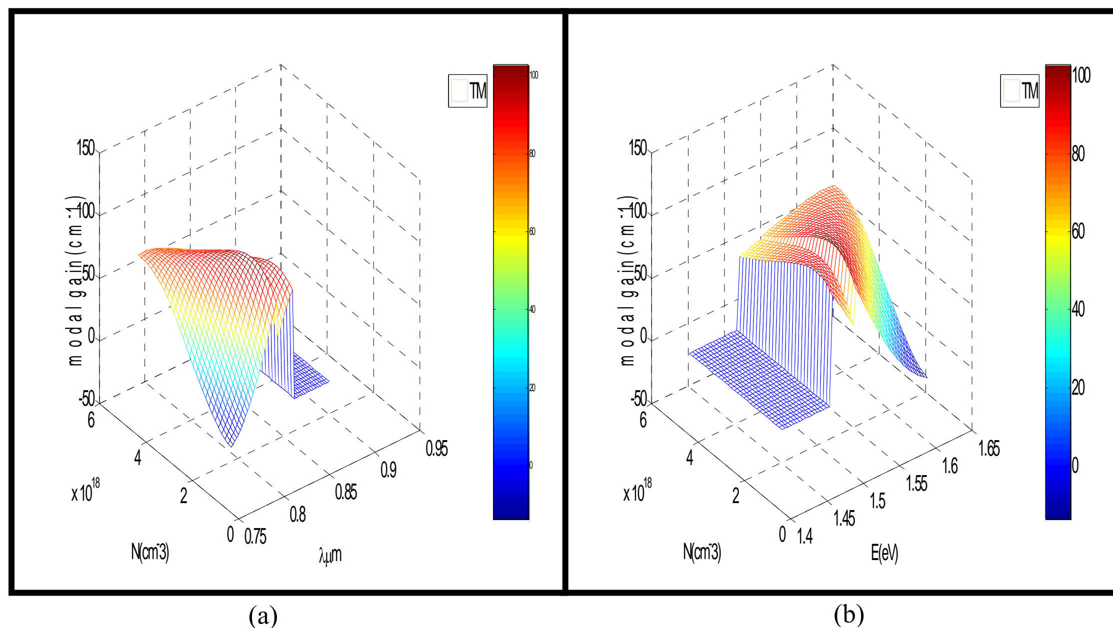

(a) (b)

Fig.(5.18) 3-D plot of the TM modal gain with the injected carrier density and, (a) the transition wavelength, (b) the transition energy

The relation between the modal gain for the same injection condition, N=3.348e18 cm^{-3}, versus the wavelength transition and the transition energy, respectively using L_z=75 Å, T=300°K is shown Fig.(5.19a,b). The transition energy and wavelength are varied due to the fact that varying the quantum well thickness will result in a change in transition energy. Also, reducing the active region thickness will result in an increase in both the simplified modal gain, and the TE enhanced polarized modal gain.

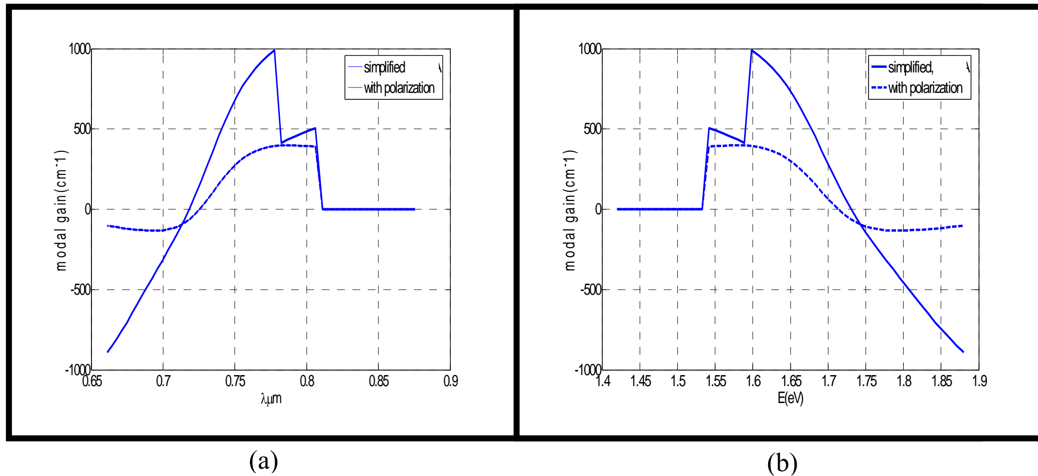

(a) (b)

Fig.(5.19) Plot of the modal gain versus (a) the transition wavelength, (b) the transition energy, Lz=75 Å.

Fig.(5.20a,b) is a 3-D plot of the TE modal gain with carrier concentration against the transition wavelength, and the transition energy, the difference between the TE using Lz=100°A curve and that using L_z=75 Å is the increase in the peak modal gain in the later case.

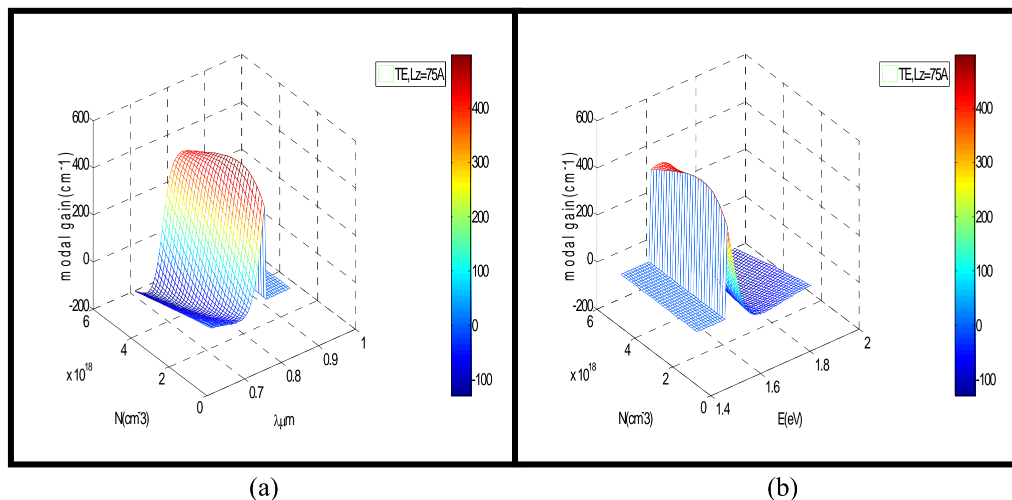

(a) (b)

Fig.(5.20) 3-D plot of the TE modal gain with the injected carrier density and, (a) the transition wavelength, (b) the transition energy, Lz=75 Å.

Fig.(5.21) is a 3-D plot of the TM modal gain with carrier concentration against the transition wavelength, and the transition energy. The difference between the TM curve and the TE curve that the polarization enhancement of the TE modal gain is more obvious than that of the TM mode, also there is an increase in the peak modal gain.

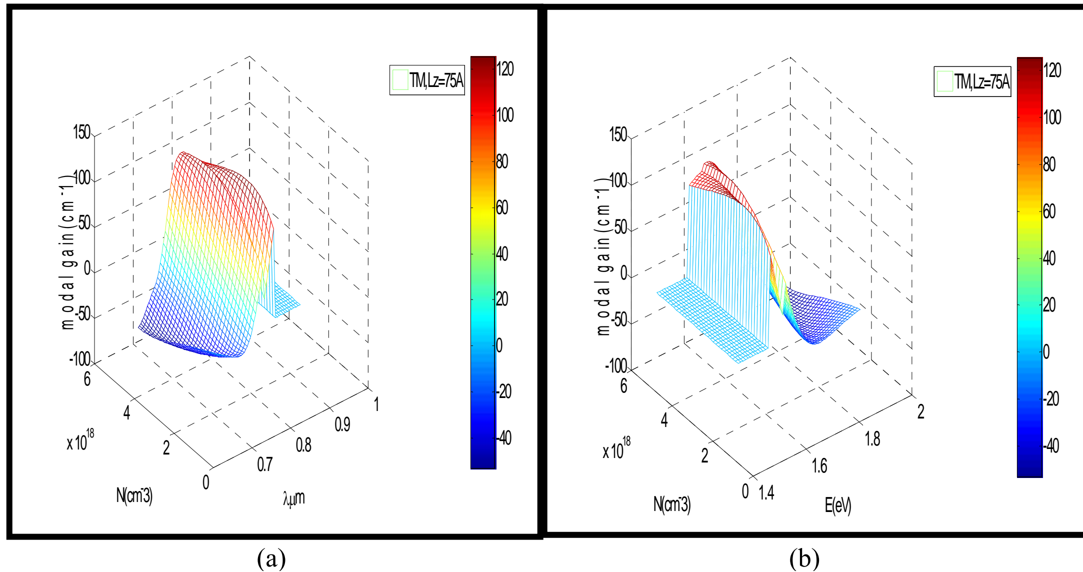

(a) (b)

Fig.(5.21) 3-D plot of the TM modal gain with the injected carrier density and, (a) the transition wavelength, (b) the transition energy, Lz=75 Å.

5.2.2.2 Spontaneous Emission Rate:

The sponaneous emission rate is calculated for injected carrier density, N=1.27e18cm^{-3}, and the thickness of the well is L_z=100 Å, at T=300°K. This spectrum represents the total emission at all angles and polarizations as shown in Fig.(5.22a,b). This spectrally dependent sponatanous emission rate represents the radiative component of carrier recombination, therefore this rate does not contain the polarization anisotropy.

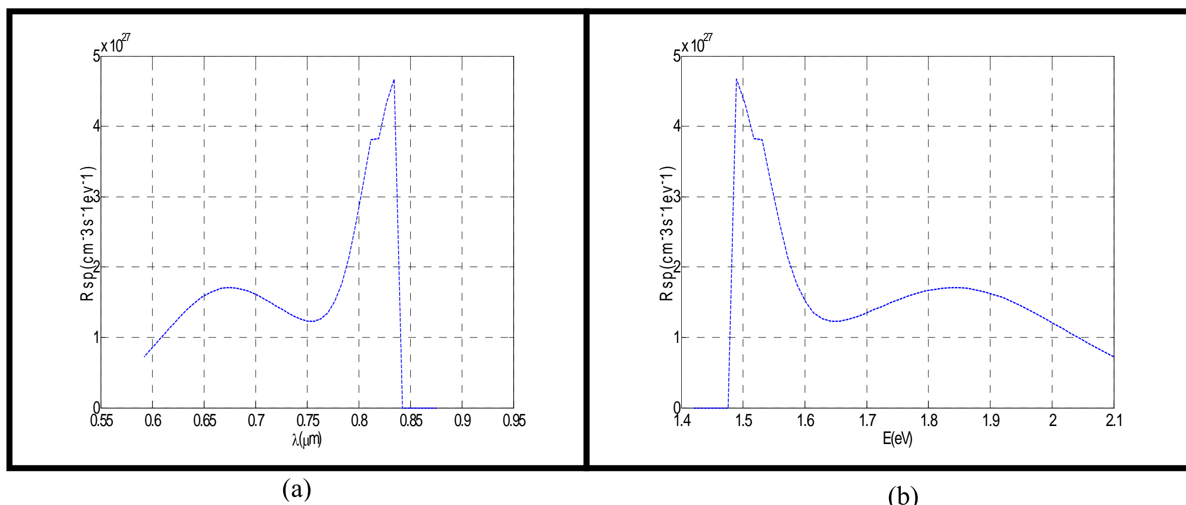

(a) (b)

Fig.(5.22) Plot of the spontaneous emission rate versus, (a) the transition wavelength, (b) the transition energy, L_z=100 Å.

Fig.(5.23 a, b) is a 3-D plot of the spontaneous emission rate and the injected carrier density versus the transition energy and the transition wavelength, respectively. It is obvious that increasing the injected carrier density will result in an increase in the spontaneous emission rate due to that fact of increasing the radiative recombination.

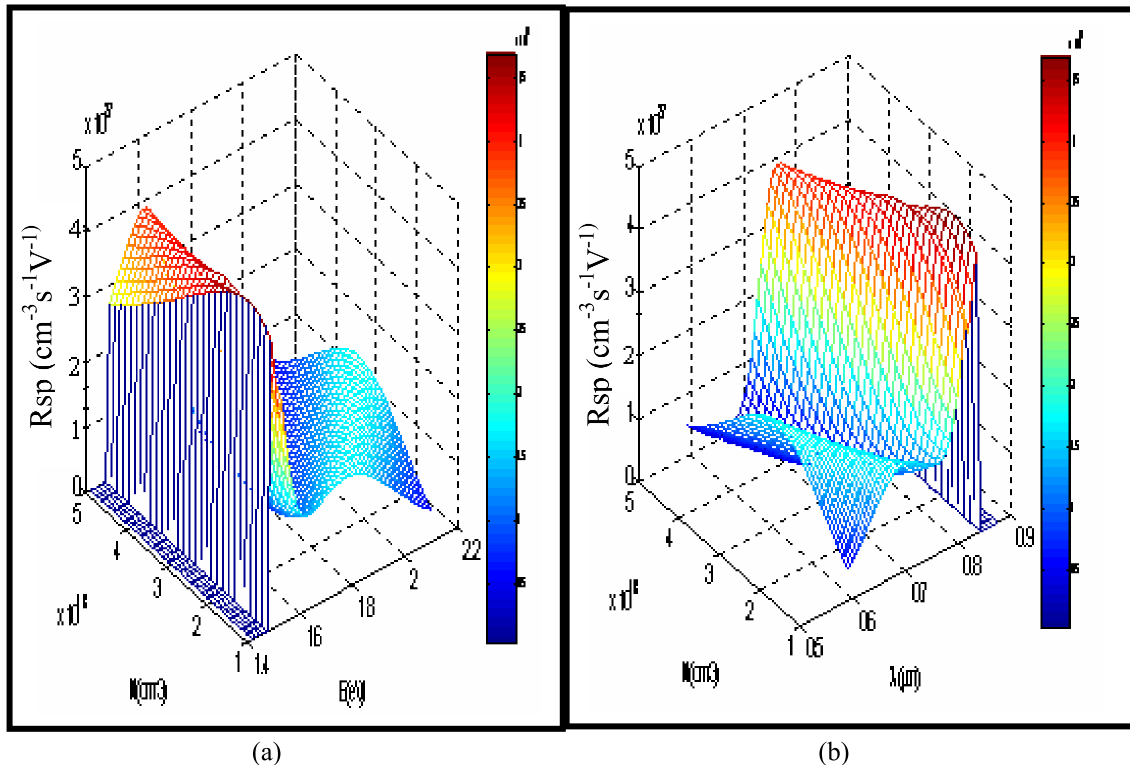

Fig.(5.23) 3-D plot of the spontaneous emission rate with the injected carrier density versus, (a) the transition energy, (b) the transition wavelength, L_z=100 Ǻ.

The sponaneous emission rate is calculated for injected carrier density, N=4.724e18 cm^{-3}, and the thickness of the well is L_z=75 Ǻ, at T=300°K. This spectrum represents the total emission at all angles and polarizations as shown in Fig.(5.24a,b),

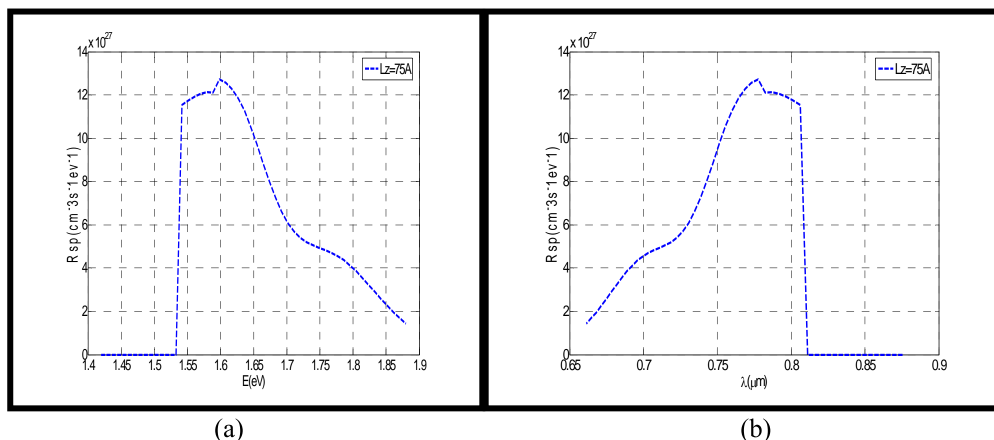

Fig.(5.24) Plot of the spontaneous emission rate versus, (a) the transition wavelength, (b) the transition energy, Lz=75 Ǻ.

Fig.(5.25a, b) is a 3-D plot of the spontaneous emission rate and the injected carrier density versus the transition energy and the transition wavelength, respectively. Again it is obvious that increasing the injected carrier density will result in an increase in the spontaneous emission rate due to that fact of increasing the radiative recombination.

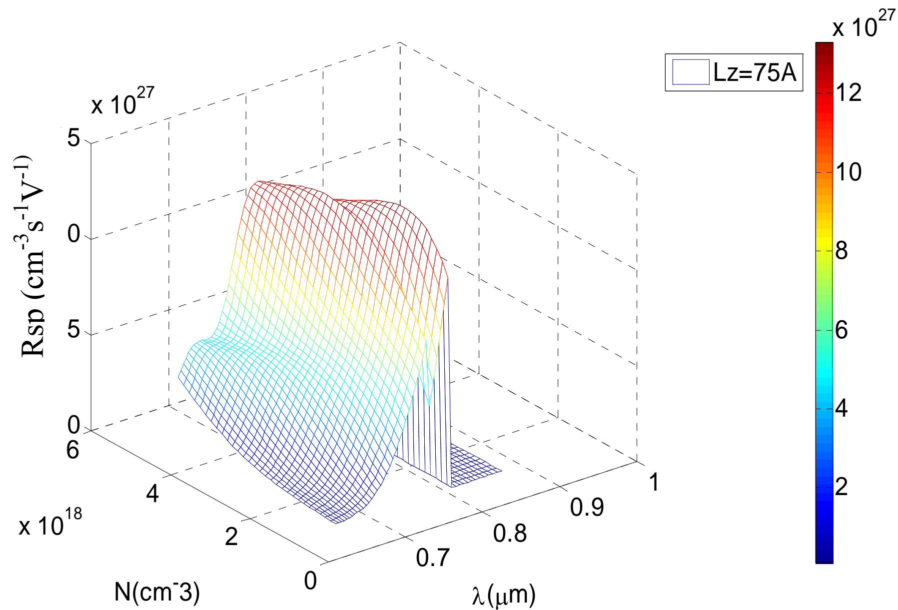

(a)

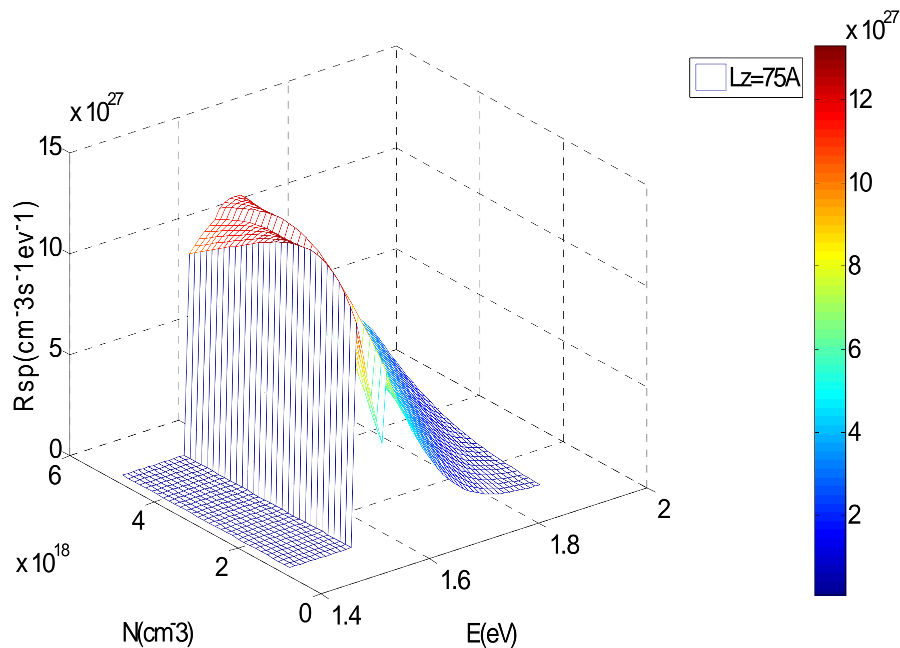

(b)

Fig.(5.25) 3-D plot of the spontaneous emission rate with the injected carrier density versus, (a) the transition energy, (b) the transition wavelength.

5.2.2.3 Peak modal gain and transparency density:

Fig.(5.26a, b, c, d) shows the peak modal gain versus the injected carrier density at well thickness of L_z =(200, 150, 100, 75) Å, respectively. The high gain sensitivity of g_{max} to changes in the number of injected electrons for different well widths. Because of their high density of states, narrow wells could be useful when high gain values are needed.

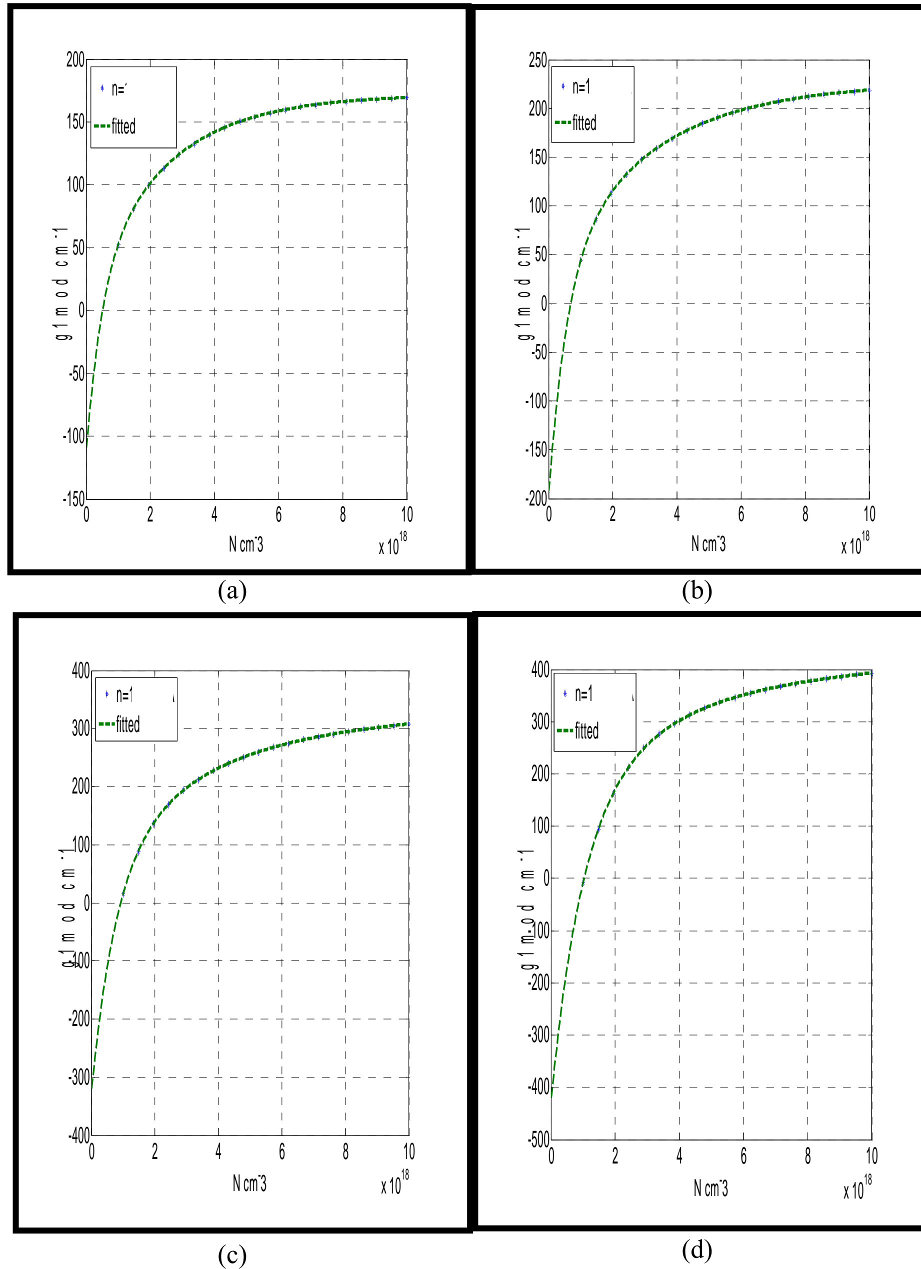

Fig.(5.26) Peak modal gain versus the injected carrier density at, (a) L_z=200 Å, (b) L_z=150 Å, (c) L_z=100 Å, (d) L_z=75 Å.

Fig.(5.27) shows the relation between the value of the zero gain injection (transparency) versus the well thickness obtained from Fig.(5.26), from this figure the value of transparency shifts down to a lower injection current as L_z increases.

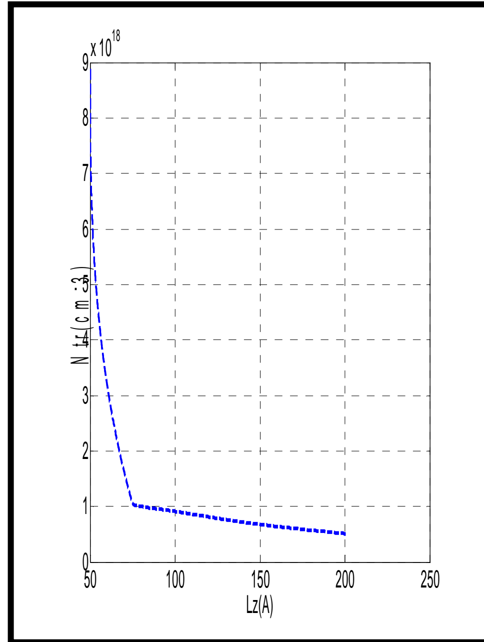

Fig.(5.27) Plot of the transparency carrier density versus the well thickness.

5.2.2.4 Nonradiative transitions and carrier leakage:

Unavoidable Nonradiative and leakage current components are known o contribute to the total current, leading to possibly substantial deviation from the idealization. These mechanisms for such nonideal contributions have been considered, (1) Nonradiative transitions inside the QW's, which includes bulk and interface recombination via defect states in the bandgap, as well as Auger recombination; (2) carrier "leakage" over the top of the QW's into the continuum of the bulk- like states, including spillage sideways to the barrier layers, and, eventually, to the cladding layers, possibly involving recombination from the higher lying indirect conduction band valleys (L and X).

Fig.(5.28) is a 3-D plot of the interface recombination current versus the QW carrier density and the interface recombination velocity, the figure clearly demonstrates the severity of interface recombination, particularly at low N values. It needs to be stressed that interface recombination is the only nonideal contribution to the current that affects primarily the region of lower injection carrier density, which is the preferred operating

region of QW lasers. Therefore, technological attention to the quality of the interfaces during epitaxial growth is of utmost importance.

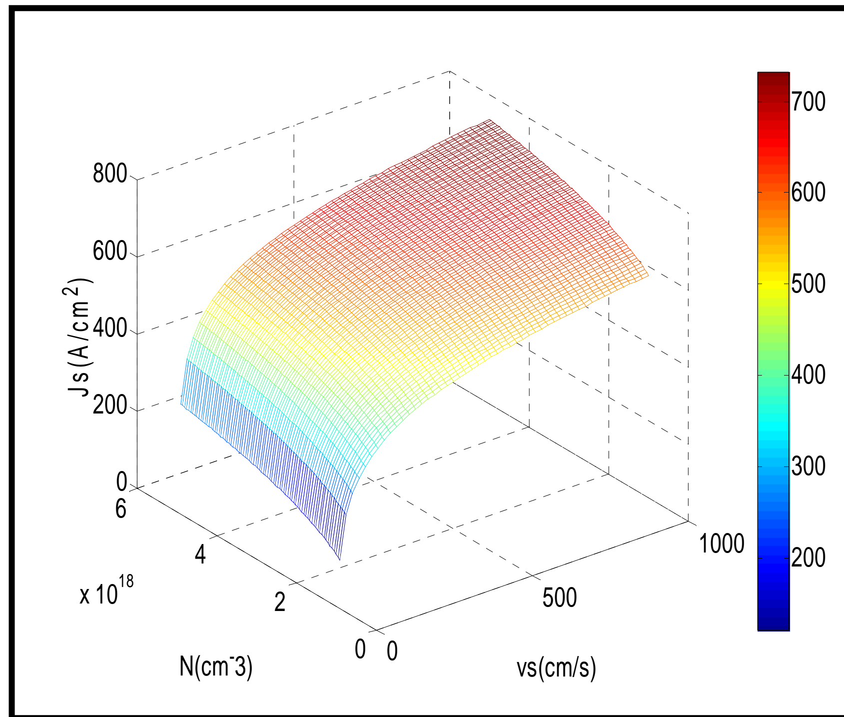

Fig.(5.28) 3-D plot of the interface recombination current density (log J_s) versus the recombination velocities and QW injection carrier density N.

Fig.(5.29) is a 3-D plot of the Auger recombination current density, the QW carrier density, and the thickness of the well. In the auger effect, the energy released by a recombining electron is absorbed by another electron (or hole), which then dissipates the energy by the emission of phonons, which becomes proportional to N^3. It is apparent that Auger recombination is largely negligible in GaAs except for high injection densities. Its contribution is below 20% for $N<5*10^{18}$ cm^{-3}.

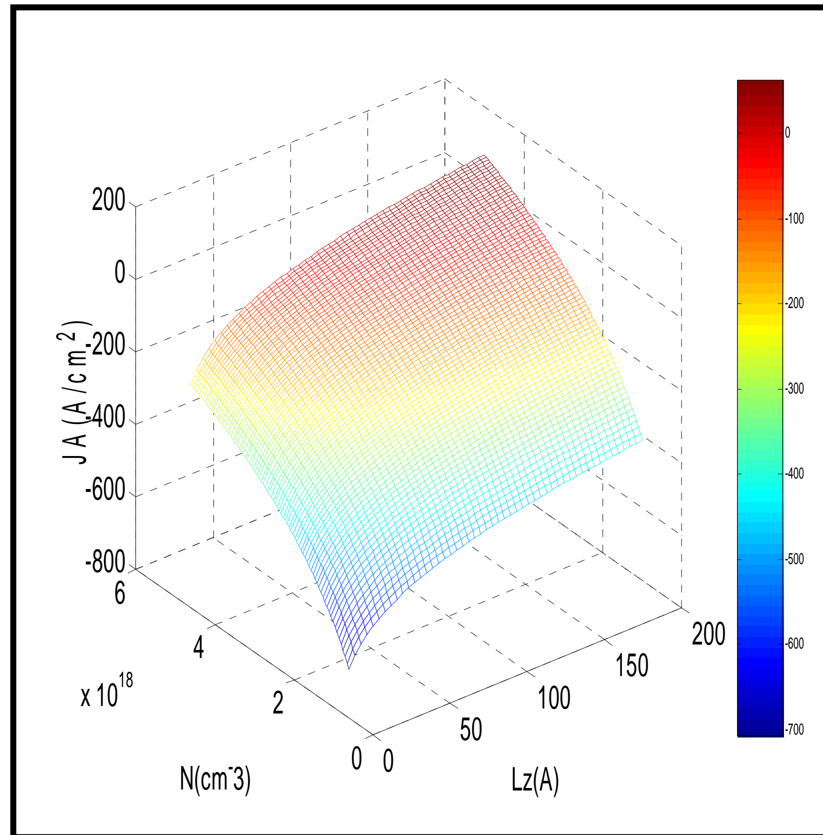

Fig.(5.29) 3-D plot of the Auger recombination current density (log J_A) versus QW injection carrier density, and the QW thickness.

Fig.(5.30) is a 3-D plot of the QW leakage current density with the QW injection carrier density and carrier lifetime, with QW thickness L_z=75 Å. The carrier leakage out the QWs within the guiding region can be estimated from the potential steps formed at the QW hetero-interfaces and the positions of the quasi-Fermi levels. Since the carrier diffusion lengths are generally large compared with the typical thickness of the overall guiding region in the structure. It seems to be that the leakage component behaves very similarly to the Auger component of being negligible except at a high injection. There, its contribution reaches values somewhat larger than the Auger current when $N>6.2*10^{18}cm^{-3}$.

The carrier leakage out of the QW is very temperature sensitive, and this may lead to a substantial contribution to the temperature dependence of threshold current in a QW laser.

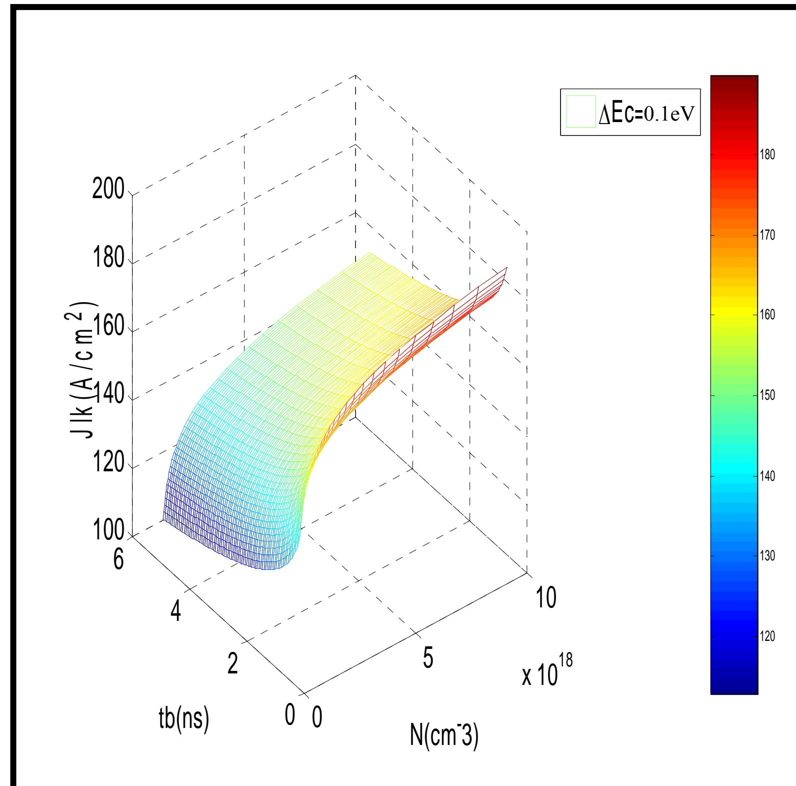

Fig.(5.30) 3-D plot of QW leakage current density (log J_{lk}) versus QW injection carrier density and carrier lifetimes.

5.2.2.5 Radiative QW current:

Fig.(5.31) shows the relation between the radiative current density for different QW thickness (L_z=75 Å, 100 Å, 150 Å, 200 Å) was drawn against the injected carrier density, to obtain the spectral gain maximum versus current density, the radiative component of the current is calculated by integration of the spontaneous emission, at higher injection levels the situation becomes more favorable, because the radiative current increases more rapidly due to bimolecular nature roughly proportional to N^2. It can be seen that increasing the carrier density for L_z=200 Å will result in a decrease of the value of the injected carrier density.

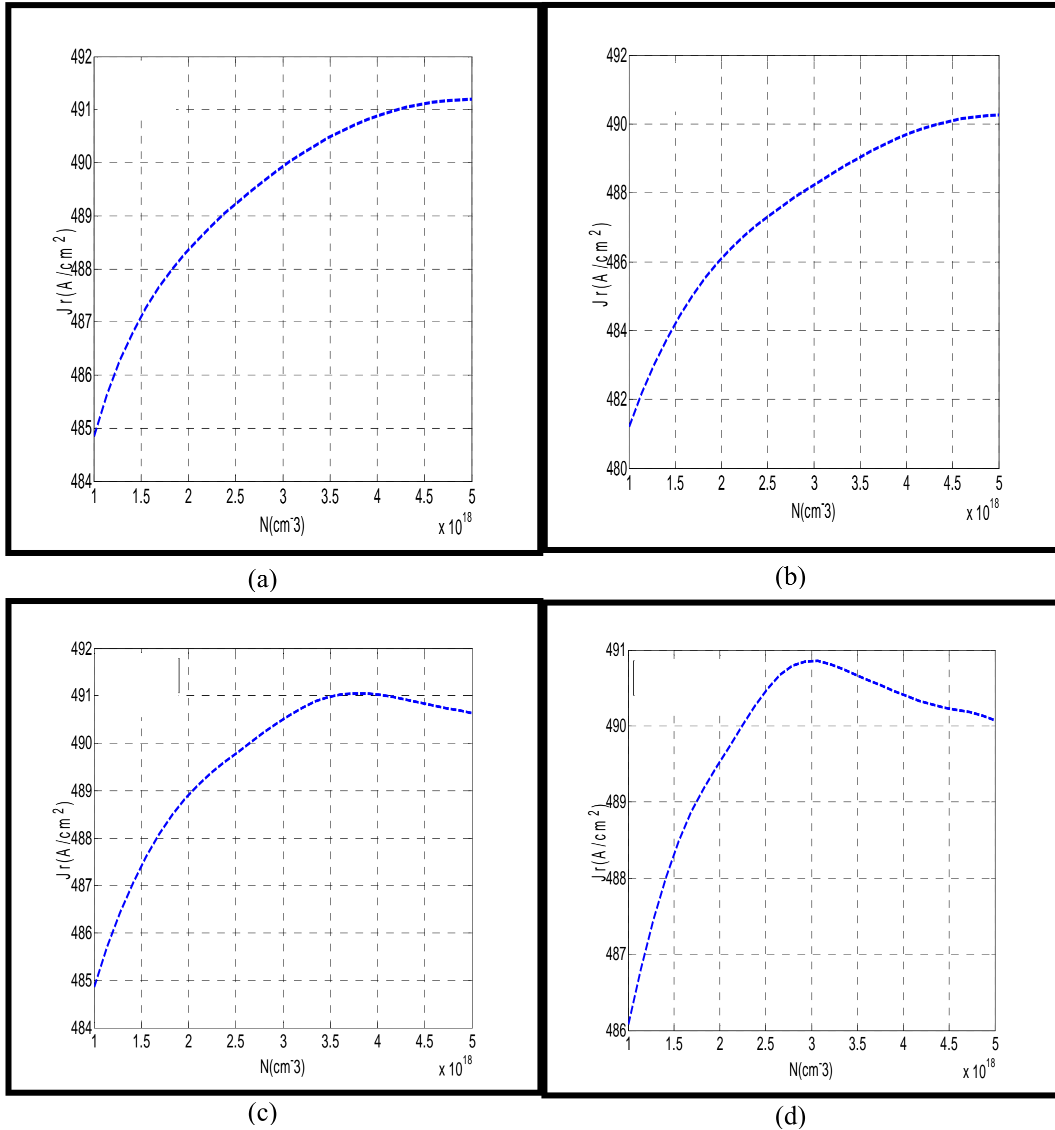

Fig.(5.31) plot of the radiative current density (log J_r) versus the injected carrier density at, (a)L_z=75 Å, (b) L_z=100 Å, (c) L_z=150 Å, (d) L_z=200 Å.

Fig.(5.32a,b) is a 3-D plot of the Quasi-Fermi level against the injected QW carrier density and the QW thickness, which represents the probability of occupation of a given energy state, in either conduction or valence subband, which is affected by the density of electrons N_e and holes N_h injected to the corresponding bands.

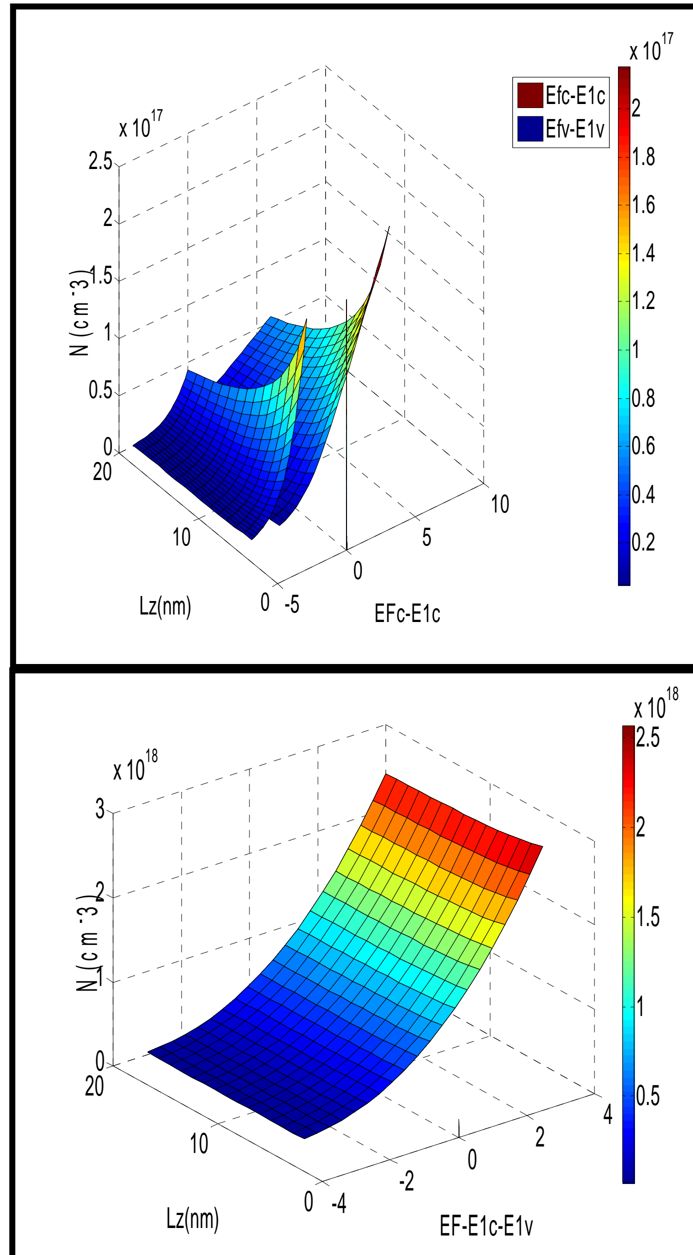

Fig.(5.32a,b) 3-D plot of the Quasi-Fermi level against the injected carrier density and the QW thickness

5.3 Heat treatment inside the QW laser:

Temperature dependence of the bandgap and the quasi-Fermi levels that cause the gain to depend on the temperature relate the output wavelength to the temperature of the active region. As the cavity temperature tends to rise with the operation of the laser, the output wavelength will show a notable shift. Fig.(4.33) shows a 3-D plot shows the relation between the operating temperature, the cavity position, and the time. A full knowledge of the exact temperature profile along the cavity is an advantage in designing heat sinks capable of reducing catastrophic optical damage for high power laser diodes. From this figure as the cavity position increases the temperature increases, i.e. greater temperature increase at the laser facets, and at the facets there is no gradual increases in temperature, i.e. tendency to catastrophic optical damage.

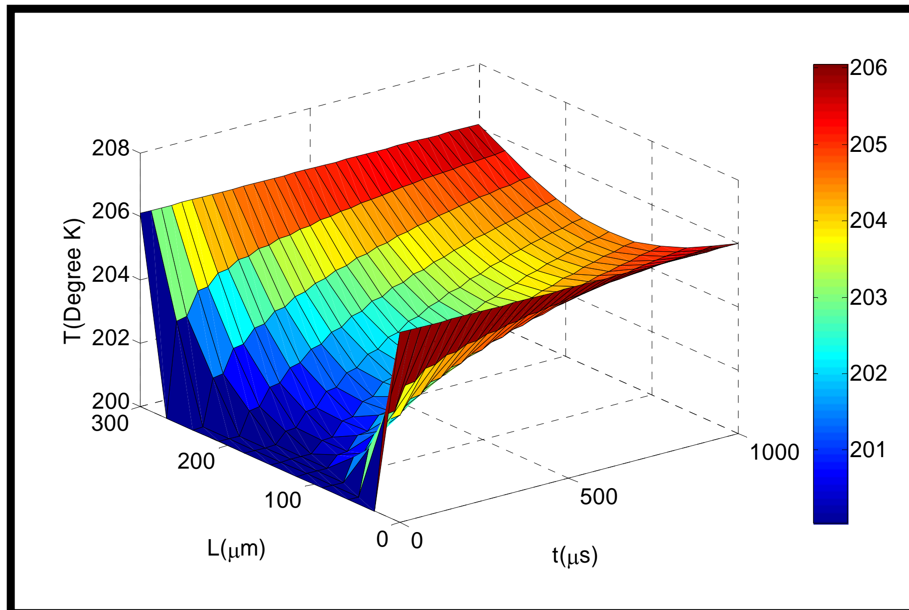

Fig.(5.33) 3-D plot of the heat conduction equation.

6.1 Conclusions:

QW Laser structure shows improvements compared to conventional double heterostructure (DH) laser, the most improvement parameters are:

1- Higher polarization stability due to large difference of the optical gain for the TE and TM modes.
2- Higher peak gain results for different quantum well thicknesses over the conventional laser.
3- Width of the gain spectra decreases, showing better gain discrimination as the well narrows.
4- Below a critical L_z value, despite the increase of the density of states, the gain decreases.
5- Reducing the temperature of the laser diode will reduce the threshold current and increases the obtained output power.
6- Bandgap renormalization at high injected carriers leads to a peak gain shift towards longer wavelength.
7- From the experimental work it was found that the CW operation of face pumped V-shape laser using QW laser source is more efficient than using bulk diode laser.

   In pulsed mode it was found that reducing the repetition rate increases the peak pumping power i.e. increases the output laser peak power due to the fact that reducing the temperature of the laser medium and increasing the ability of internal amplification at low repetition rates.

   It is necessary to use external triggering to lower the repetition rate of the diode laser, which in turn will need less cooling than operating in high repetition rates and will increase the optical to optical slope efficiency of the system due to the increased peak pumping power.

   The optimum resonator length which achieves the maximum output power was found to be 10 cm, and the maximum attained power was found to be 95 mW, with slope efficiency of 42.6% for direct face pumping (internal triggering), while for external triggering the maximum output power was found to be 150 mW, at a repetition rate of 50 Hz, and the slope efficiency was found to be 66.6%.

   The optimum output coupler reflectivity which achieves the maximum output power was found to be 90%.

The threshold power were found to be ≈45mW at R=30%, and the lower threshold power was found to be ≈39mW at R=99%.
The optimum value for the repetition rate when the laser diode is operating in external triggering was found to be 50 Hz.

For V-shape pumping using QW laser in CW mode the optimum resonator length was found to be 14.5 cm which achieves a maximum output power of 58 mW, with a slope efficiency of 11.3%, using bulk diode laser the efficiency was found to be 3.2%, with a maximum output power of 29 mW, this draws us to the fact that QW laser source is more efficient and suitable for pumping solid state media.

For internal triggering, the maximum output power was achieved at an operating temperature of 16°C, which equals to 40 mW, while for external triggering the maximum output power was found to be equals to 158 mW at repetition rate of 11Hz, with a slope efficiency of 71.4%.

The optimum value for repetition rate for operating the bulk laser diode in external triggering was found to be 11Hz.

6.2 Future Work:

There is still a lot of work that could be done in this field to improve the present work which suggested being a future work, such as:

1- The effect of adding an external magnetic field on band edge, density of states, gain profile and as a result on the current sensitivity to the temperature.
2- Studying the effect of lattice mismatch between the well and the barrier (results in a stress), that will affect the material gain and as a result the current.
3- Increasing the confinement of the electron (reducing the dimensionality of the semiconductor device), i.e. from quantum well to wire then to dot, which significantly affects the electronic and optical properties of low-dimensional systems which in turn can de directly attributed to the influence of dimensionality on the density of states, and lowers the current sensitivity to temperature.
4- Modulation dynamics can be investigated in quantum well lasers.
5- Intrsubband lasers (QCL) which based on supperlattice concept can be studied and a comparison can be made between the interband QW lasers and intersubband QCL.

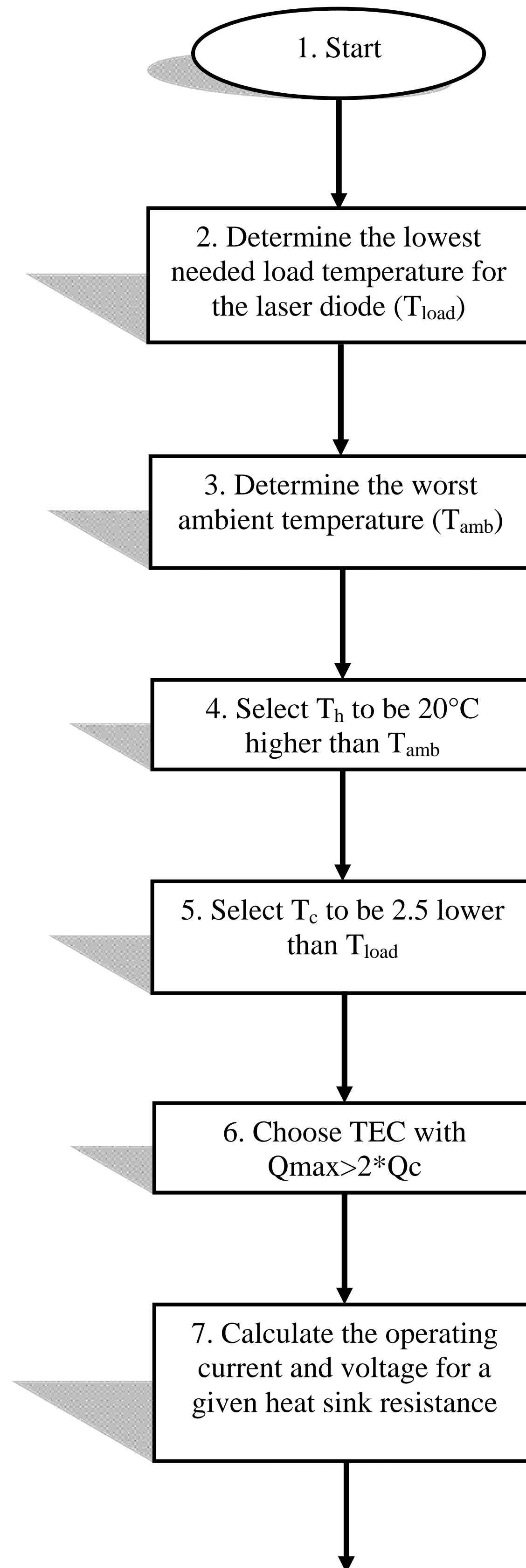
1. Start
2. Determine the lowest needed load temperature for the laser diode (T_{load})
3. Determine the worst ambient temperature (T_{amb})
4. Select T_h to be 20°C higher than T_{amb}
5. Select T_c to be 2.5 lower than T_{load}
6. Choose TEC with Qmax>2*Qc
7. Calculate the operating current and voltage for a given heat sink resistance

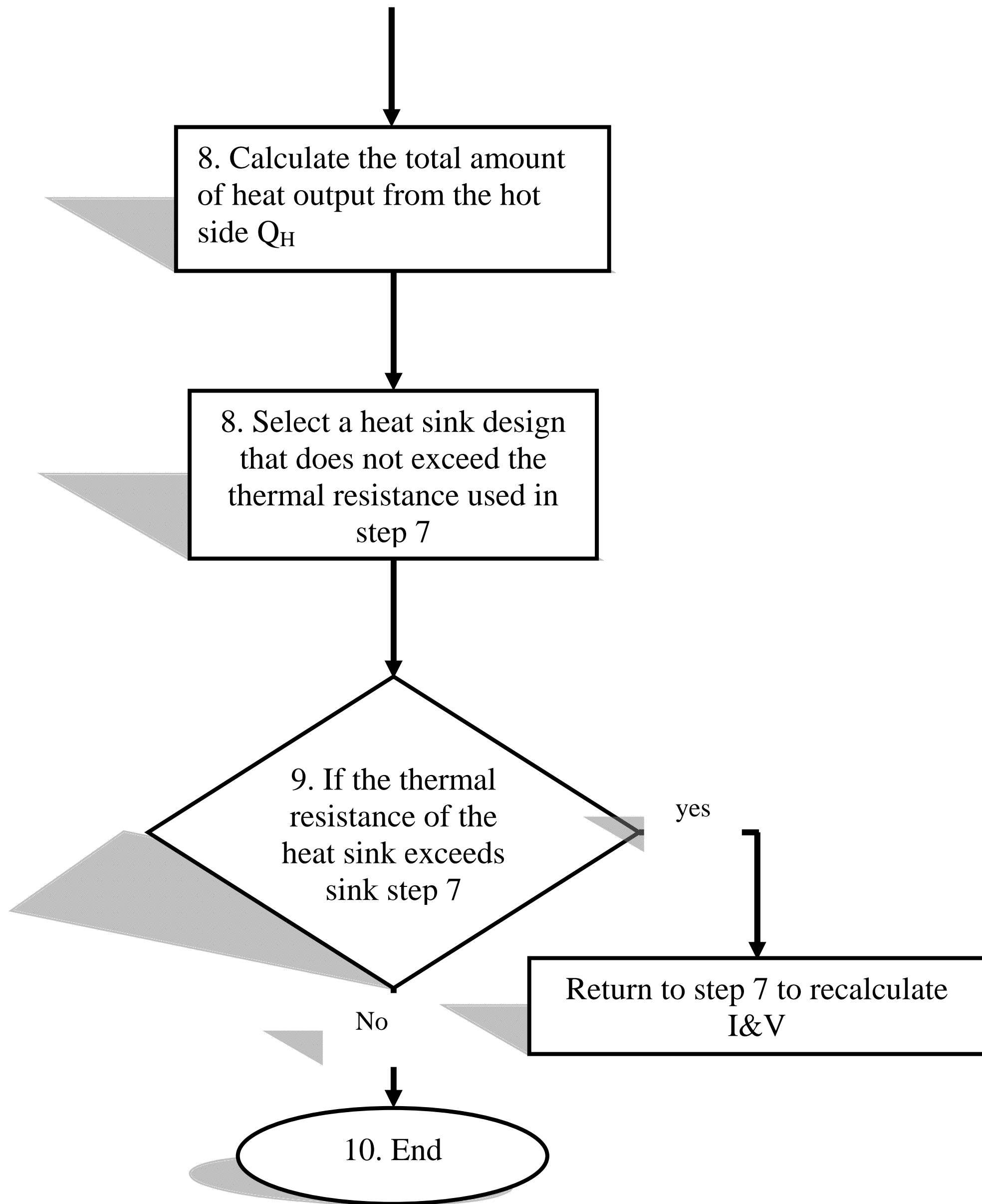
8. Calculate the total amount of heat output from the hot side Q_H
8. Select a heat sink design that does not exceed the thermal resistance used in step 7
9. If the thermal resistance of the heat sink exceeds sink step 7
yes
Return to step 7 to recalculate I&V
No
10. End

1.1 Historical Background:

The semiconductor laser has a history as long as that of the laser itself. The concept of a semiconductor laser was introduced by Basov et al.(1961), who suggested that stimulated emission of radiation could occur in semiconductors by the recombination of carriers injected across a p-n junction. After this the progress were slow for many reasons, one of them involving high threshold currents for lasing, which limited laser operation to short pulses at cryogenic temperatures, and low efficiency, which led to a high heat dissipation. These problems were solved by the introduction of heterostructures. In a heterostructure laser, one replaces the simple p-n junction with multiple semiconductor layers of different compositions. Thus CW operation at room temperature became possible because of better carrier and optical confinement. Laser performance continued to improve as more advanced heterostructures, such as quantum wells and strained quantum wells were used as gain media.

Two factors are largely responsible for the transformation of semiconductor lasers from laboratory devices operating only at cryogenic temperature into practical optoelectronic components capable of running continuously at room temperature. One is the exceptional and fortuitous close lattice match between AlAs and GaAs, which allow heterostructures consisting of layers of different compositions of $Al_xGa_{1-x}As$ to be grown. The second is the performance of several important opto-electronic applications where semiconductor lasers are uniquely well suited because they have the smallest size (several cubic millimeters), highest efficiency (often as much as 50% or even more) and the longest lifetime of all existing lasers, [1].

Semiconductor lasers or laser diodes are the most widely used laser ever devised. They are normally pumped directly with an injection current. Laser diodes are used in such everyday items as CD players and laser printers and are finding a host of new applications ranging from medical imaging to environmental sensing. The semiconductor laser is also the source which drives optical fiber communications, [2]. A specific aspect of the progress made in semiconductor lasers is the wide wavelength range covered by the source using different semiconductor materials. Laser diodes from the ultra-violet through to the mid and far infrared are available. The III-V semiconductor materials used for the devices are summarized in table 1.1, along with some of their key physical properties. The materials are grouped as nitrides, arsenides, phosphates and antimonides which

sequentially lead to longer wavelength devices when combined as ternaries (Fig.1.1). Quaternaries combining the arsenides and phosphates are used for devices at the key telecommunication wavelengths of 1.3 and 1.55 μm. In all the materials, lasers of shorter wavelength than that associated with the energy band gap of the bulk semiconductor material, a binary, ternary, or quaternary, can be obtained using quantum wells. The visible semiconductor lasers based on AlGaInP are quantum well (QW) devices, usually multiple QWs. Longer wavelength lasers (4-12 μm) have been produced using intersub-band transitions in quantum cascade lasers. Strain can also be used to vary the energy gap of the active layer material in a semiconductor laser, [2].

Table 1.1 Key III–V Semiconductor materials used in semiconductor lasers which operate at room temperature and their key physical properties

III–V Compounds	Lattice Constant (Angstroms)	Electron (Conduction band) Effective Mass+	Heavy Hole (Valence band) Effective Mass+	Relative Dielectric Constant	Refractive Index (Near E_G)	Band Gap (E_G) at ~300 K(eV)
AlN	3.112# 4.982	0.40	3.53	8.5	2.15	6.28
GaN	3.190 5.185	0.20	0.80	8.9	2.5	3.425
InN	3.545 5.703	0.11	1.63	15.3	2.9	1.20 1.9$
AlAs*	5.6611	0.146	0.76	10.1	3.2	2.168
GaAs	5.6533	0.067	0.45	13.1	3.4	1.42
InAs	6.0584	0.022	0.40	15.1	3.5	0.354
AlP*	5.4635	0.83	0.70	9.8	3.0	2.45
GaP*	5.4512	0.82	0.60	11.1	3.37	2.26
InP	5.8686	0.08	0.56	12.4	3.4	1.35
AlSb*	6.1355	0.33	0.47	12.0	3.5	1.63
GaSb	6.0959	0.041	0.27	15.7	3.9	0.70
InSb	6.4794	0.014	0.34	16.8	3.5	0.175

Notes:
* Indirect Band Gap Compound, all others Direct Gap
# Nitrides have a hexagonal (Wurtzite) crystal structure, hence two lattice constants, a_o and c_o, c/a~1.633 from theory for closest packed arrangement
+ Relative to the rest mass of an electron
$ Earlier value of 0.70 is now regarded as incorrect, actual value measured varies in different materials

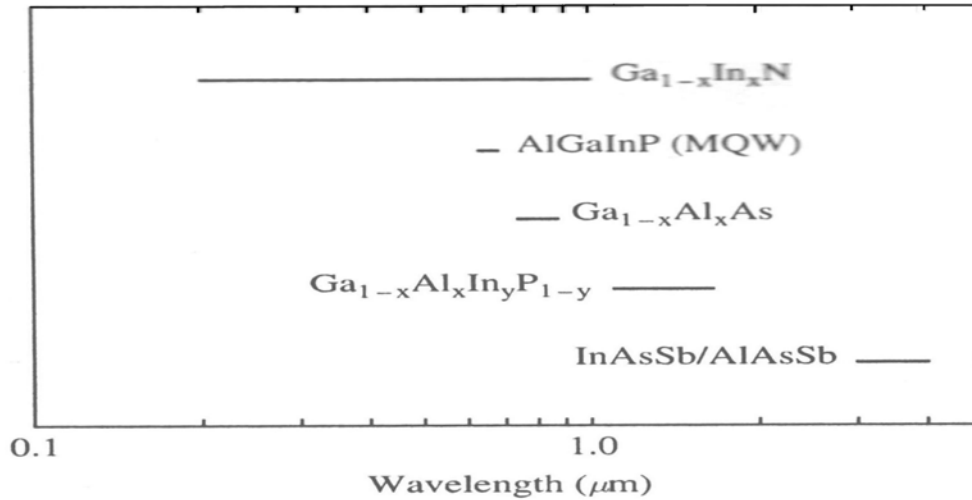

Fig.(1.1).Range of emission wavelengths possible with different III-V semiconductor material compositions, [2].

Laser action arises in laser diodes due to a recombination of charge carriers injected into semiconductor material using an electrical contact. The double heterostructure semiconductor laser achieves confinement of the injected carriers in the active layer region via potential barriers as indicated in the band structure for a forward biased ppn double heterostructure laser diode shown in Fig.(1.2). It achieves confinement of the injected carriers in the active layer region via potential barriers.

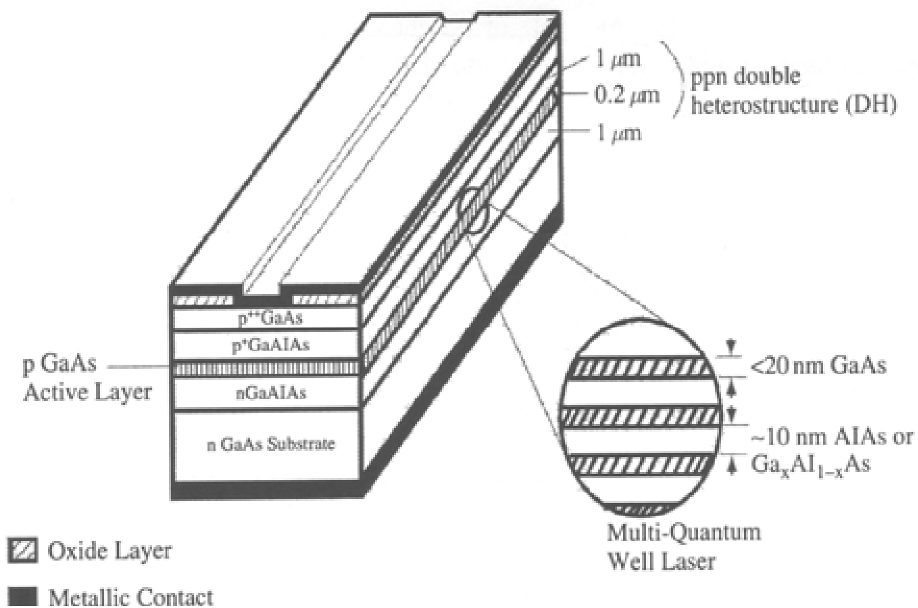

Fig.(1.2) Standard GaAs/$Ga_{1-x}Al_xAs$ stripe double heterostructure laser diode in the case of a QW stripe DH LD the active layer is made up of one or more quantum wells as indicated by the inset expansion,[2].

1.2 Motivation:

Modern solid state lasers being compact, reliable and moderately priced, diode lasers are indispensable as they represent the most efficient pump source available. This statement applies to CW lasers as well as to ultra- short pulse lasers.

The main features that distinguish the semiconductor laser are, [3,14]:

1. Small physical size (300 μm×10 μm×50 μm) that enables it to be incorporated easily into other instruments.
2. Its direct pumping by low-power electric current (15 mA at 2 volts is typical), $\hbar\omega \approx E_g \approx qV_a$ which makes it possible to drive it with conventional transistor circuity, and making battery operation a very useful option.
3. Its superior efficiency in converting electric power to light. Actual operating efficiencies, e.g. Ar^+, HeNe<1%, solid state lasers 1-20%. CO_2 lasers≤30%, semiconductor lasers ≤50%.
4. The ability to modulate its output by direct modulation of the pumping current at rates exceeding 20 GHz. This is of major importance in high-data rate optical communication systems.
5. The compatibility of its output beam dimensions with those of typical silica based fibers and the possibility of tailoring its output wavelength to the low-loss, low-dispersion region of such fibers.

While the disadvantages of laser diodes are, [5]:

- ❖ Very large beam divergence 10°-60° full angle at 1/2 power making them essentially useless without a collimating lens of high quality. Furthermore, the divergence is typically 2 to 4 times greater in one direction than in the orthogonal direction, yielding an elliptical beam in cross section, so to efficiently collect and collimate the radiation it is needed a very high numerical aperture lens.
- ❖ The diodes are very susceptible to static and to electrical current or voltage transients. Over current for microseconds can irreparably damage a facet, constraints of the circuit for current control include a soft turn on and off, (i.e. absolutely no current/voltage spikes on power up or down).
- ❖ The power output even at constant current is strongly temperature dependent, the maximum current should be limited to less than or equal to maximum rated current at the highest design operating temperature a possible approach is using a series resistor.

❖ The wavelength is also a strongly temperature function which can be an inconvenience or can be used with suitable temperature control to tune the output to a desired wavelength, for the designer that wants to precisely control wavelength and power output the LD device should be mounted on a TEC cooler which must be well-heat sunk and controlled by a stable high feedback circuit with adequately sensitive and positioned thermistor sensor capable of holding the temperature of the reference surface constant to a few millidegrees centigrade.

❖ The lifetime is also strongly temperature dependent so that for long reliable device of >10,000hours, the device temperature should be maintained close to room temperature and not allowed to exceed 40°C.

❖ The spectral output, which in some devices can at rated maximum output power be a very narrow single frequency TEMoo mode with long coherence length, may at lower output power degenerate into multimode operation.

❖ The polarization ratio is a strong function of operating output power being more truly plane polarized at higher output powers. Polarization ratios of 100:1 or more are difficult to achieve.

❖ The modulation of output power can be achieved by varying the device current. To achieve repeatable power levels, or depth of modulation at high rates in the 10 to 100 MHz range, requires very careful circuit design with the need to control the device temperature.

Fig.(1.3a) shows a cross section through a typical double heterostructure diode laser. In order to generate laser light coming close to a beam by having at least comparable dimensions in both orthogonal directions to the axis of propagation, some structure perpendicular to the layer planes has to be foreseen generally called stripe laser design see Fig.(3.1a). This leads to the emission of an **astigmatic beam** having different angles of divergence in both possible orthogonal directions described by an elliptical cross section. All modern LEDs, ILDs and SLD consist of an active layer and two cladding layers surrounded by a substrate on one side and a contact layer on the other side, as shown in Fig.(1.3b).

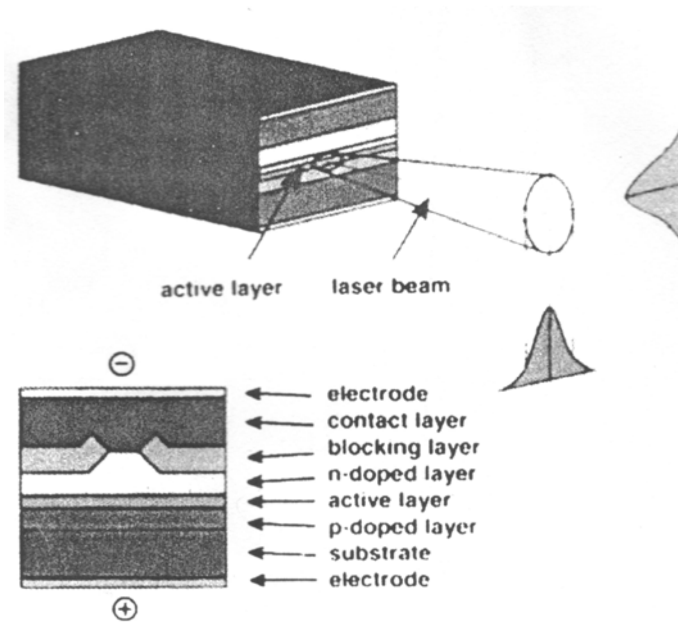

Fig.(1.3a) Basic description of a modern heterostructure diode laser. Upper part: indicating as astigmatic beam out of facet. Lower part: cross-section showing the layers including a waveguide structure, [12].

layer	Wavelength	
	0.3 to 0.83 µm	1.1 to 1.67µm
Contact layer	GaAs	$In_{1-u}Ga_uAs_vP_{1-v}$
Cladding layer	$Ga_{1-y}Al_yAs$	InP
Active layer	$Ga_{1-x}Al_xAs$	$In_{1-x}Ga_xAs_yP_{1-y}$
Cladding layer	$Ga_{1-z}Al_zAs$	InP
Substrate	GaAs	InP
	y>x, z>x	x>u, y>v

Fig.(1.3b) Basic structure and material composition of LEDs and ILDs, [15].

In combination with solid-state lasers to be pumped, two heterostructures combinations have proven to be most useful and commercially mature (i.e. available at moderate prices and sufficient output power): the **broad-area AlGaAs/GaAs laser diode** (λ ≈800 nm) depicted in Fig.(1.4) and the **broad-area InGaAs/AlGaAs laser diode** (λ

≈980 nm, shown in Fig.(1.5)). Both figures give various typical details about dimensions, layer composition and contacts. In order to be able to freely choose wavelength and lattice matched substrate when designing a laser diode, a plot of energygap versus lattice parameter as shown in Fig.(1.6) is required.

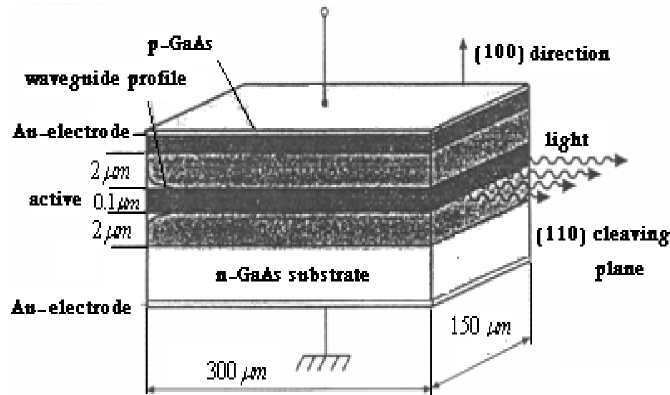

Fig.(1.4) Broad-area AlGaAs/GaAs laser diode: layer composition, dimensions and contacts are specified, [12].

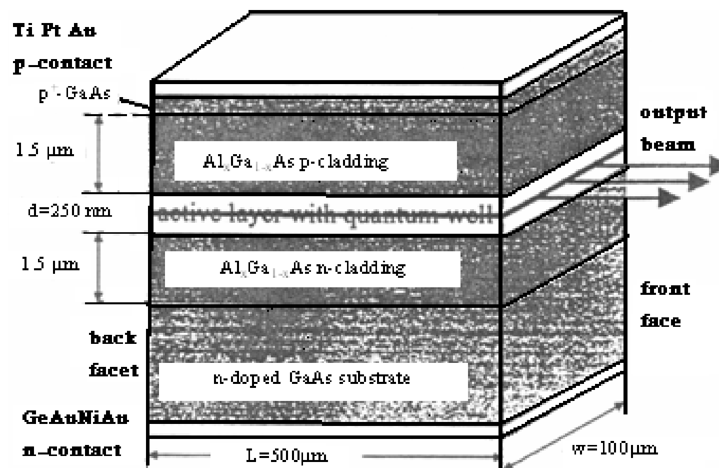

Fig.(1.5) broad-area InGaAs/AlGaAs laser diode: layer composition, dimensions and contacts are specified, [12].

Fig.(1.6) for InAlGaAsP compound semiconductors is very useful. **Lattice match** in general is necessary (exception: strained layers being just elastically distorted) to prevent losses caused by lattice defects, like e.g. dislocations or stacking faults. The lattice parameter of GaAs and InP are clearly marked by bold lines in the figure.

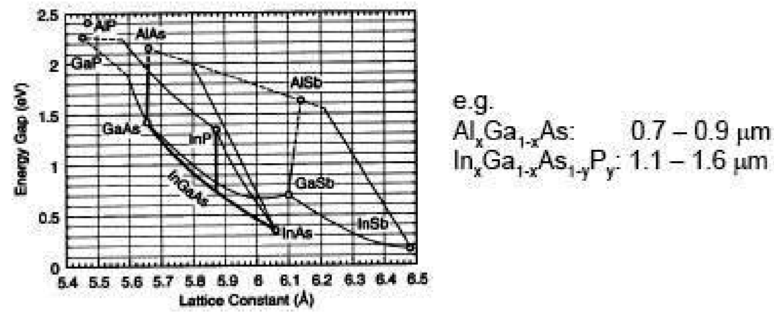

Fig.(1.6) bandgap and lattice parameters of InAlGaAsP compound semiconductors, [1].

1.3 Quantum well laser:

Since the 1990s practically all laser diodes include quantum wells (QWs) in the active layer of diode lasers. Lasers that include quantum wells in their active region are called **quantum well lasers.** If the thickness of the active layer of a DH laser is greatly reduced to a point where the dimension becomes comparable to the deBroglie wavelength, ($\lambda \approx h/p$), a QW double heterostructure laser is produced. Such lasers exploit the more favorable optical properties of a QW or multiple QW (MQW) structure compared to those of the corresponding bulk material (in particular the increased differential gain and decreased dependence of this gain on temperature). These favorable properties are essentially related to the completely different form for the density of states of QW materials compared to bulk materials, arising from quantum confinement in the well direction. Strong QW and also MQW lasers are however seriously affected by the strong reduction in the confinement factor arising from reduced layer thickness, [6].

To limit beam size in the QW direction, one must then use a separate confinement structure, [10]. Though a number of layers are added to the semiconductor, the size of the laser diode is kept to a minimum by arranging the layers in a structure called "Quantum Wells". A quantum well is a three-layer structure with very thin layer of laser material in - between layers of higher bandgap material, as shown in Fig.(1.7).

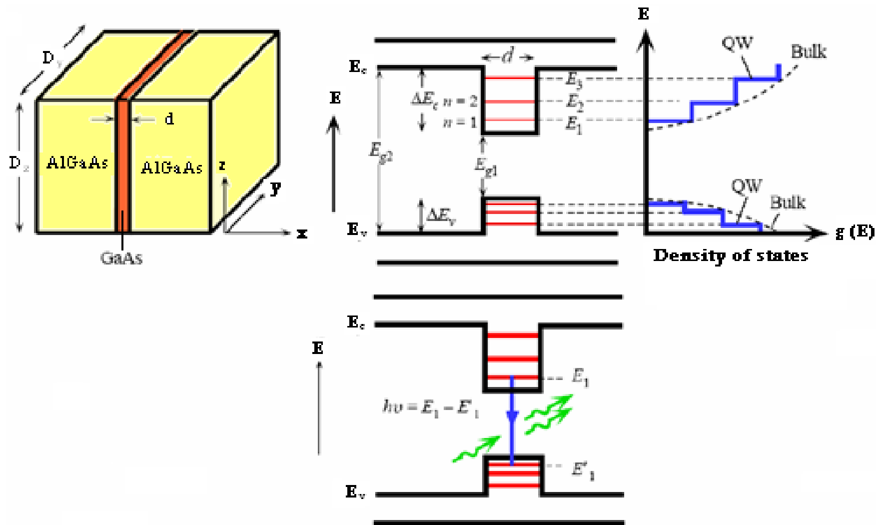

Fig.(1.7) Single quantum well GaAs/GaAlAs laser, [16].

The quantum well is a development that is a result of the advancement in the epitaxial layer growth technology. The main advantage of the quantum well structure is the vast improvement of the lasing action due to the variation of the energy level distribution of the semiconductor material when its thickness is reduced below 20nm. The high concentration of charge carriers in the narrow strip of the active material reduces the threshold current required to initiate lasing. The high bandgap layers on either side of the active layers perform confinement of charge carriers to the active materials as well as confinement of the laser output to a narrow width. A multiple-quantum-well is a structure consisting of an alternating pattern of active and high bandgap materials, [6].

Another feature used in a commercial laser diode is the use of an internal photodiode known as monitor photodiode. This monitor photodiode is used in the feedback loop to stabilize the output power from the laser. While laser diodes convert electrical energy to optical energy, photodiodes transform optical energy to electrical energy. Absorption of photons of energy greater than or equal to the energy gap of photodiode results in generation of electron-hole pairs. These charge carriers under the influence of an external electric field drift to the electrodes of opposite polarity, creating a net current. The current generated is proportional to the number of incident photons. This current is fed to the circuit which drives the laser diode, and it increases or decreases the output of the diode as the case may be, [18].

Quantum well lasers have several advantages, [7]:

- ✓ Putting QWs in the active region further reduces the threshold current.
  - For example, in a single quantum well laser the threshold current can be of the order of 0.5-1 mA, while in a double heterostructure lasers that does not include QWs this value is in the 10-50 mA range.
- ✓ The emission wavelength of QWs can be controlled by appropriately choosing the width of the quantum well.

The photon energy from a QW is given by,[76]:

$$\hbar\omega=Eg+E_n+Ep, \quad \ldots\ldots(1.1)$$

where:

E_g is the bandgap energy,

$E_{n,p}$ are the confinement energies for the electrons (p) and holes (p), are given by:

$$E_{n,p}=\hbar^2(n\pi/L_z)^2/(2m_{c,v}), \quad \ldots\ldots(1.2)$$

where:

L_z is the QW layer thickness,

$m_{c,,v}$ is the effective mass for electrons and holes.

Thus, within certain limits, the emission wavelength of a laser can be modified by varying the appropriate layer thickness, 'L_z' of the QW. Obviously, this can only be done when the material is grown, [15].

- ✓ The emission linewidth is significantly narrower in QW lasers than in bulk diode lasers. This is due to the fact that in QWs the electrons (holes) are confined to discrete energy levels, and not to energy bands. This means that the range of photon energies emitted by the laser is also limited to a narrow spectrum.
- ✓ Laser structures can have one or more QWs in the active region.

Depending on the details of the structure, the current depending optical gain is different in bulk GaAs, GaAs quantum well and stained InGaAs quantum well material. Fig.(1.8) allows to compare the structures , quantum wells locally in their energy bands exhibiting a higher density of states give rise to such higher gain, [12].

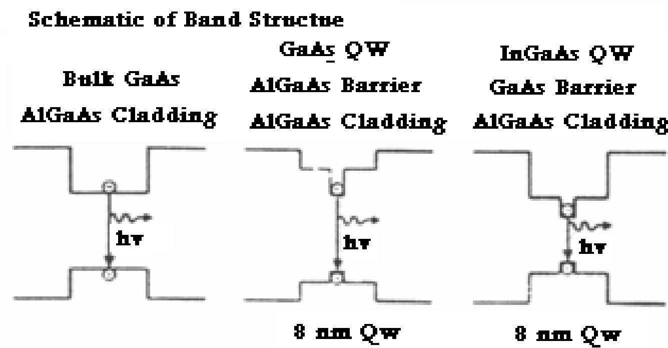

Fig.(1.8) Schematic of bandgap structures, [12].

The schematics of the laser active region with multiple QWs (MQW) is shown in Fig.(1.9):

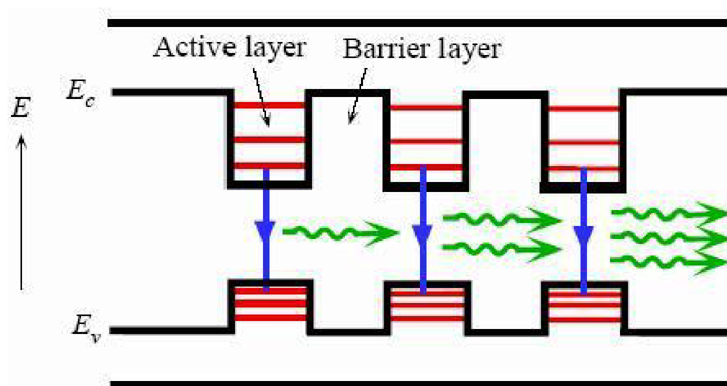

Fig.(1.9) Multi-quantum wells in the active region of a diode laser, [15].

However, since the gain volume of a QW is very small (i.e. the QW width is very small), the overlap between the optical field and the charge carriers is not great. (a similar problems are encountered when talking about homojunction lasers.) Therefore, to further improve the efficiency of these types of lasers, the QWs are usually surrounded by an optical waveguide structure so as to confine the photons to near the quantum well.

This is done by 'sandwiching' the active layer between layers of lower refractive index. Similarly to double heterostructure lasers, the multi-layer arrangement results in a waveguide structure that confines the photons to a region near the quantum well, while the quantum well itself confines the charge carriers. This type of arrangement, where the optical field and the charge carriers are separately confined, is known as **separate confinement heterostructure laser** (SCH), [8].

In one variation of this concept, the quantum well is inserted into a region in which the composition (and hence the refractive index) of the confining material is continuously

varied. The role of the graded refractive index is to confine light to the active region. These lasers are given the rather uninspiring but accurate name of "**Graded Refractive Index Separate Confinement Heterostructure Laser"** or GRINSCH**.** Fig.(1.10) shows, a GRINSCH design, [1]:

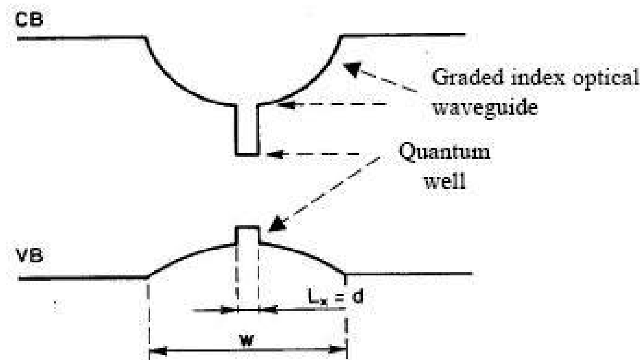

Fig.(1.10) Energy band structure of a GRINSCH laser, where 'd' is the width of the quantum well and 'w' is the width of the optical waveguide, [15].

Fig.(1.11a) shows a particularly simple example of several structures introduced for this purpose. Everything in this figure is to scale except for the bulk GaAs bandgap energy. At the centre of the structure is the thin (~10 nm) QW (GaAs) and, on both sides of the well, are two thicker (~0.1 μm) inner barrier layers of wider bandgap and, hence, lower refractive index material ($Al_{0.2}Ga_{0.8}As$). Outside the inner barrier layers are two much thicker (~1 μm) cladding layers of still wider bandgap material ($Al_{0.6}Ga_{0.4}As$), constituting the p and n sides of the diode, [17].

Beam confinement is established by the higher refractive index of the inner barrier layers compared to cladding layers, while the contribution to the confinement by the very thin QW is negligible. The resulting beam intensity for this waveguide configuration is also shown as a dashed line in Fig.(1.11a). The full width between the $1/e^2$ points, in this case, is confined to a comparatively small dimension (~0.8 μm). A somewhat similar and widely used structure is shown in Fig.(1.20b), where the index of composition of the inner barrier layer ($Al_xGa_{1-x}As$) gradually changes from e.g. x=0.2 at the QW interface to the value x=0.6 at the interfaces between the two cladding layers, where it matches the index of the cladding layers, [17], and the evolution of laser diodes is presented into table (1.2).

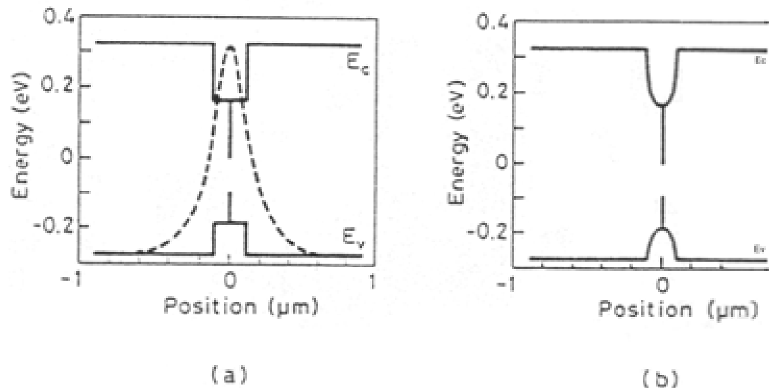

Fig.(1.11) (a) Energy bands of a step index $Al_xGa_{1-x}As$-GaAs separate confinement QW heterostructure. The resulting optical mode profile for this waveguide structure is shown as a dashed line. (b) Energy bands of a grade index AlxGa1$_{-x}$As-GaAs separate confinement QW heterostructure (GRINSCH), [17].

Table (1.2) Evolution of laser diode structure and geometries, [4].

I. Layer structure
1. Homojunction [by diffusion or liquid phase epitaxial (LPE) technique
Example: n-GaAs/p-GaAs/GaAs
2.Single heterojunctions (by LPE) techniques
Example: n-GaAs/p-GaAs/$Al_xGa_{1-x}As$
3.Double heterojunctions (by various epitaxial methods)
Example: n-$Al_{1-x}Ga_{1-x}As$/GaAs/p-$Al_xGa_{1-x}As$
4.Quqntum wells
II. Geometry in the transverse direction
1. Broad area lasers multiple longitudinal modes and multiple transverse modes
2. Stripe geometry lasers (single-mode lasers): single transverse mode and multiple transverse modes
i. Gain-Guided stripe lasers
ii. Index-guided stripe geometry lasers
III. Optical cavity (single-mode single frequency)
1. Short cavity lasers
2. Lasers with distributed Bragg reflectors, distributed feedback, or external grating reflectors
3. Lasers with external mirrors, grooved couple cavity, cleaved coupled cavity, or integrated etalon interference

1.4 Diode-Pumped Solid-State Lasers:

The history of diode-pumped solid-state lasers goes back to 1974. As the laser diodes at that time were very immature severe barriers to practical application were impossible to overcome at the beginning: cryogenic temperature and **high laser threshold current density** >1 kA/cm^2. Quantum well lasers allowing room temperature operation and low laser threshold current density <0.2 kA/cm^2 represented a major break-through. The modern era of diode-pumped solid-state lasers (DPSSLs) opened with the work of the Byer group and Spies. A particularly interesting case involves using diode lasers to pump other solid-state laser materials, thus providing an all solid-state laser. The most relevant examples include, [17]:

- ND:YAG, Nd:YLF, Nd:YVO_4, Nd:glass pumped by GaAs/AlGaAs quantum well (QW) lasers at ~800 nm (typical oscillation wavelengths are around 1μm, 1.3μm, and 0.95μm.
- Yb:YAG, Er:glass or Yb:glass pumped InGaAs/GaAs strained QW lasers in the 950-980 nm range (oscillation wavelength is around 1μm for Yb and 1.54μm for Er lasers). Note that, in the case of Er:Yb codoping, pump light is mostly absorbed by Yb^{+3} ions and then transferred to Er^{+3} lasing ions.
- Alexandrite, Cr:LiSAF, or Cr:LiCAF pumped by GaInP/AlGaInP QW lasers in the 640-680 nm range and oscillating in a ~1300 nm range around 840 nm.
- Tm:Ho:YAG pumped by AlGaAs QW lasers at 785 nm and oscillating around 2.08μm. Note that, in this case, pump light is absorbed by Tm^{+3} ions and transferred to Ho^{+3} lasing ions.

For the example of Nd:glass to be pumped by either AlGaAs diode or Xe-arc lamp the significant advantage of the diode as a solid-state laser pump source are explained in Fig.(1.12) as listed in the insert.

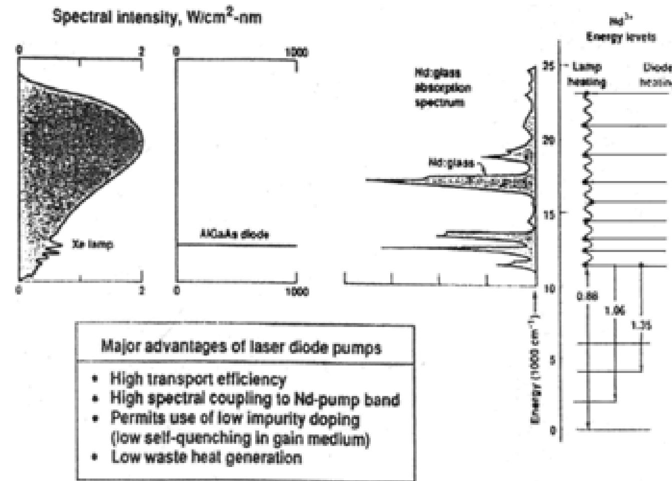

Fig.(1.12) Advantages of AlGaAs laser diodes compared to Xe-arc lamps as Neodymium solid-state laser pump sources, [12].

Fig.(1.13) allows to judge how well the visible and near IR regimes are covered by the emission spectra of commercial semiconductor laser diodes. The upper part shows the maximum power efficiency reaching outstanding values close to 60% for AlGaAs, the lower part allows comparing the maximum facet flux again indicating InGaAsP to be the best material emitting up to~70W/cm, [8,79].

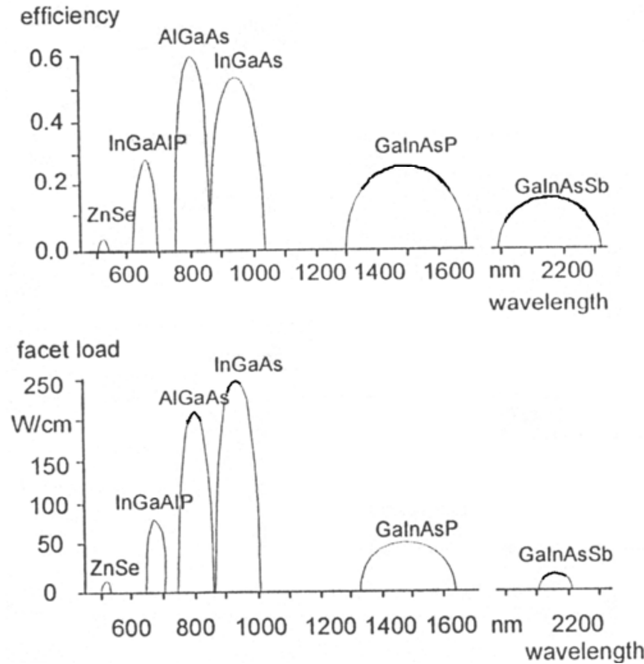

Fig.(1.13) Representative diode array performance extremes (cw, room temperature): maximum power efficiency and maximum facet ,load versus wavelength, [8].

For higher total output powers, **two dimensional stacking** is necessary but yielding a problem of how to get rid of the waste heat, despite the high diode efficiencies. Fig.(1.14, 15) indicate proven solution: the baseline diode cooler design together with a micro-lens conditioned diode laser array as developed by Lawrence Livermore National Laboratory (LLNL). The cooler is a micro-structured silicon device allowing to precisely channel the cooling water flow to the sources of heat. Si can be fabricated to such dimensions with much better precision than the common materials like copper, and hence yield the lower thermal impedance. The micro-lenses reduce the divergence in the vertical direction being much larger than the orthogonal one to similar dimensions. The collimation of such a radiation source can be achieved by e.g. a lens duct as it is also shown in Fig.(1.15, left). Such end-pumped cavity geometry is more compact, uses fewer and simpler optical elements, and is better suited for fiber coupling than laterally pumped solid-state laser like e.g. the slab laser, [40]

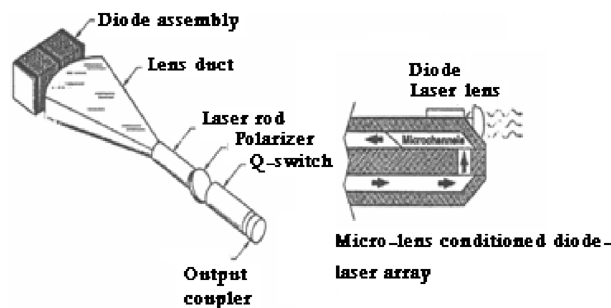

Fig.(1.14) Micro-lens conditioned diode laser array and end-pumped cavity geometry being more compact, using fewer and simpler optical elements and being better suited for fiber coupling than slab lasers, [40].

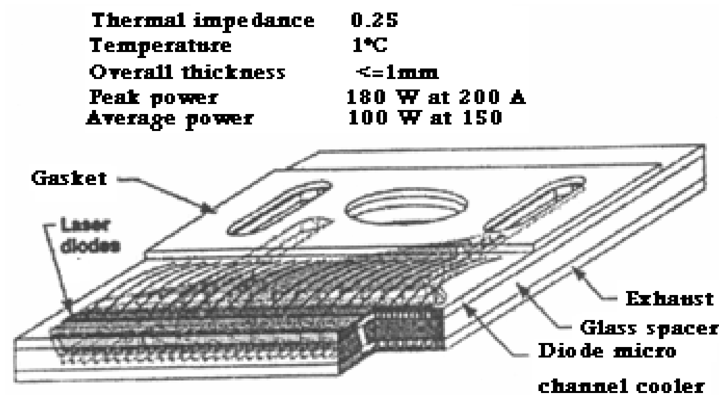

Fig.(1.15) Details of the baseline cooler design and the mounting of the laser diode depicted above, [40].

As a representative example of Nd-ion lasers, Fig.(1.16a) shows the relevant plots of the absorption coefficient versus wavelength for both Nd:YAG (continuous line) and Nd:glass (dashed line). Note that Nd:YAG is most effectively pumped at a wavelength of λ=808nm, which is obtained by a $Ga_{0.91}Al_{0.09}As/Ga_{0.7}Al_{0.3}As$ QW laser, whose emission bandwidth is typically 1-2nm wide. Nd:glass on the other hand, due to its broader and featureless absorption profile, can be pumped over a broader range around the 800nm peak. For the case of Yb-ion lasers, Fig.(1.16b) shows the relevant plots of the absorption coefficient versus wavelength for Yb:YAG (solid line) and Yb:glass (dashed line). Again the absorption coefficient for glass appears broader and featureless compared to that of YAG. The best pumping wavelength is 960 nm for Yb:YAG and 980 nm for glass; these wavelengths are obtained from a InGaAs/GaAs QW laser (e.g. $In_{0.2}Ga_{0.8}As/GaAs$ for λ=980 nm), [17].

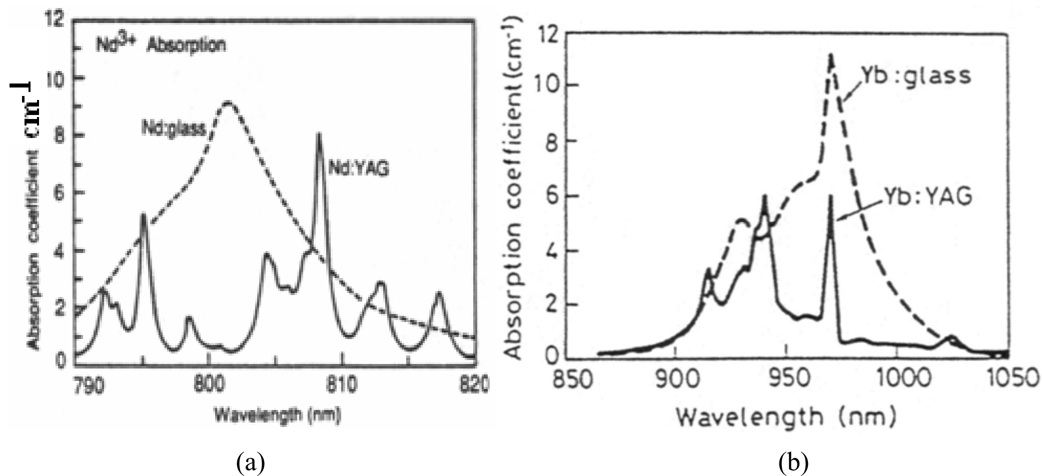

(a) (b)

Fig.(1.16) absorption coefficient versus wavelength in the wavelength range of interest for diode laser pumping: (a) Nd:YAG (solid line) and Nd:glass (dashed line). Neodymium concentration is $1.52*10^{20}$ cm^{-3} for Nd:YAG (1.1 atomic % doping) and $3.2*10^{20}$ cm^{-3} for Nd:glass (3.8 % by weight of Nd_2O_3 (b) Yb:YAG (solid line) and Yb:glass (dashed line); ytterbium concentration is $8.98*10^{20}$ cm^{-3} for Yb:YAG (6.5 atomic %) and $1*10^{20}$ cm^{-3} for Yb:glass, [75,17].

Plots of the absorption coefficient versus wavelength for Cr^{+3} ion lasers (alexandrite, Cr:LiSAF, Cr:LiCAF) show the general structureless shape the dashed curve in Fig.(1.17). The peak absorption coefficient at 600 nm wavelength is ~0.5 cm^{-1} for alexandrite and up to 50 cm^{-1} for Cr:LiSAF. Note that the higher absorption coefficient in Cr:LiSAF is due to the higher Cr concentration that can be used (~100 times higher than for alexandrite) without incurring in concentration quenching of the upper state. Due to the lack of suitable diode lasers at shorter wavelengths, pumping is achieved in the 640-

680 nm wavelength range from GaInP/AlGaInP QW lasers (e.g.$Ga_{0.5}In_{0.5}P/Al_{0.25}Ga_{0.25}In_{0.5}P$ for a 670 nm wavelength) with GaInP being the active QW layer, [10]. Table 1.3 summarizes the most relevant pumping data for some of the active media just considered.

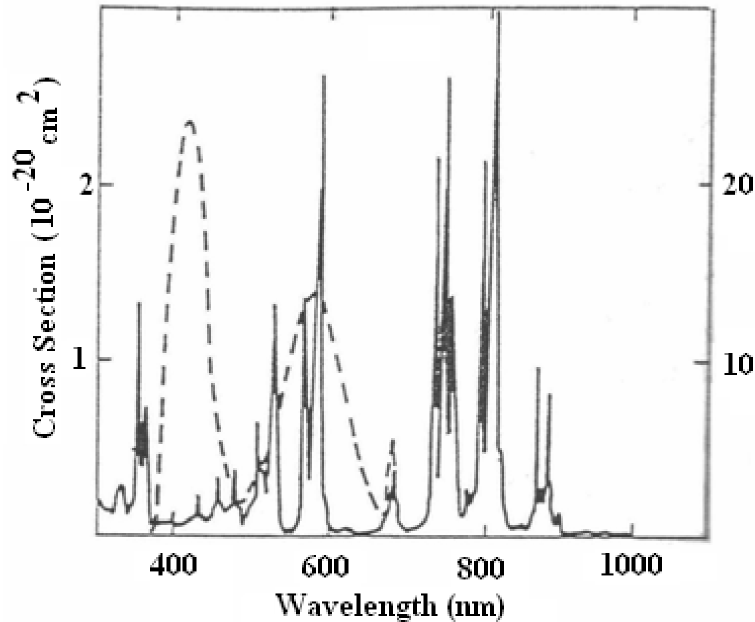

Fig.(1.17) Absorption cross section of Nd^{+3} ion in YAG (solid line) and of Cr^{+3} ion in alexandrite (dashed line). The left-hand scale refers to the cross section of Nd:YAG and the right –hand scale to alexandrite, [17].

The impact of semiconductor lasers on the development of solid-state lasers is most evident in the high-average-power, solid-state laser systems that are finding wide application in the field of materials processing. High average power, diode pumped, solid state lasers (commonly referred to as HAP DPSSLs) are best characterized as being performance limited by thermal management issues associated with solid state laser crystal or glass. Thermal management issues can manifest themselves in several different forms, such as optical quality aberration of the output laser beam due to thermally induced optical refractive index variations in the crystal and, in extreme cases, feature of the laser crystal due to buildup of excessive stress in the crystal, [40].

Table 1.3 Comparison between pumping parameters and laser wavelengths for different laser materials, [17].

	Nd:YAG	***Yb:YAG***	***Yb:Er:glass***	***Cr:LISAF***	***Tm:Ho:YAG***
Concentration	1 at.%	6.5 at.%		1 mol	6.5 at.% Tm
Pumping diode	AlGaAs	InGaAs	InGaAs	GaInP	AlGaAs
Diode wavelength (nm)	808	950	980	670	785
Active-ion concentration [10^{20} cm^{-3}]	1.38	9	19 [Yb] 1 [Er]	0.9	8 [Tm] 0.5 [Ho]
Pump absorption coefficient (cm^{-1})	4	5	16	4.5	6
Oscillation wavelength (μm)	1.06, 1.32, 1.34 0.947	5 1.03	16 1.53	4.5 0.72-0.84	6 2.08

The most common ion/host crystal combination used in HAP DPSSL systems today is Nd:YAG. Of all well developed laser crystals that can be grown with rare- earth impurities, YAG (yttribium-aluminium-garnet) is the most robust in a thermal sense- i.e., it has the highest thermal conductivity and resistance to feature. Thus, YAG is the crystalline host of choice for HAP DPSSLs. The wide use of Nd^{+3} as the active ion is nearly all HAP DPSSLs is associated with several fortuitous coincidences between the pump irradiance and wavelength that can be conveniently developed by AlGaAs semiconductor 2D laser diode arrays. AlGaAs is the most mature of the semiconductor laser materials in use today, [40].

Because many rare earth ion based HAP DPSSLs are only practical if pumped at higher irradiances than the several $1kW/cm^2$ possible with conventional scaled diode array technologies, this approach has opened a path to HAP DPSSLs that rely on ions other than Nd^{+3} as the lasant. Two of the systems, which lead the world for average power generation in their respective class, are Tm:YAG and Yb:YAG DPSSLs made by LLNL which generate output radiation at 2 and 1μm, respectively.

1.4.1 Compact Active Mirror Laser (CAMIL):

Solid-state lasers (SSL) scalable to high-average power (HAP) are highly desirable for many government and commercial applications. The key challenges to developing HAP SSL are thermomechanical effects, which occur in the gain medium as a result of pumping. Even with pumping by the efficient semiconductor laser diodes, significant portion of the pump energy is dissipated into heat, which is deposited into the SSL medium. This causes thermal lensing, mechanical stresses, and other effects, with likely consequences of degraded beam quality (**BQ**), reduced laser power, and possibly a fracture of the SSL medium. Beam quality is particularly affected by temperature gradients perpendicular to the laser axis. Popular SSL configurations, such as rods or slabs, are particularly susceptible to such thermal effects. Despite ingenious designs that are recently appeared, attempts to further increase average power output from rod and slab lasers drive the design toward regimes of increased complexity, reduced electric efficiency, and worsening **BQ**.

Disk-type SSLs enjoy inherently low susceptibility to thermo-optical distortions and have demonstrated lasing at HAP with outstanding beam quality. Their large, round aperture reduces diffraction and beam clipping losses experienced by other SSL configurations. In a disk laser, transverse temperature gradients are reduced because waste heat is extracted from the gain medium in the direction parallel to laser beam axis. A disk laser may use transmissive disks shown in Fig.(1.18a) or a reflective disks shown in Fig.(1.18b). In a tranmissive disk, waste heat is removed by a gas flowing through the optical pat. In a reflective disk, also shown as active mirror, amplifier (AMA), the back surface of the disk is available for liquid cooling, which is more efficient than gas cooling and well suited for continuous operation at HAP.

A variety of lamp-pumped AMA concepts has been investigated since the late 1960's, but the true potential of AMA was unlocked with the introduction of diode pumping.

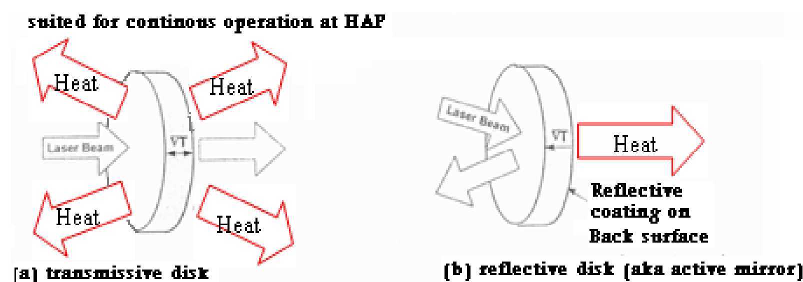

Fig.(1.18) Architectures for pumping and cooling of disk lasers, [30] .

In a CAMIL, the gain medium disk with about 1to 3 mm thickness and with a diameter typically between 1 and 15 cm is mounted on a rigid, cooled substrate, Fig.(1.19a) shows that the CAMIL substrate contains a built-in heat exchanger with microchannels on the front surface so that coolant can directly wet the back face of the laser medium disk. The disk is attached to the substrate by a hydrostatic pressure differential between the surrounding atmosphere and the coolant fluid in the microchannels. This novel approach provides very high heat transfer rates and effectively mitigates thermal deformations of the disk. Optical contact between the disk and the substrate provides an effective seal. The substrate acts as a "backbone" that mitigates thermal deformations of the disk. Pump radiation is injected into the disk either through one of the large faces (face-pumping) or through the peripheral edge (side-pumping). A laser oscillator can be constructed by placing about ten or more CAMIL modules into a conventional unstable resonator, Fig(1.19b), [12] .

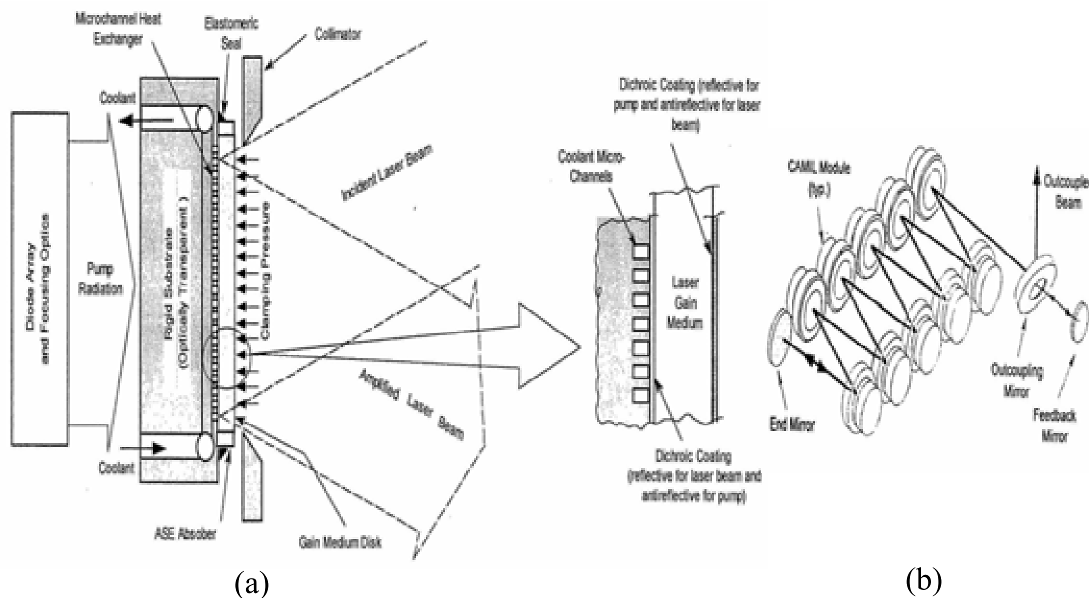

Fig.(1.19) (a)CAMIL concept, (b) Face-pumped CAMIL module, [29].

1.4.2 Face Pumping and Its Limitations:

The face pumped (FP) version of CAMIL can be implemented with diode pump radiation injected into the back face of the disk (facing the substrate) as shown in Fig.(1.20a) or the front face of the disk as shown in Fig.(1.20b). in the former case, the substrate is made of material optically transparent at pump diode wavelength. Both disk faces have with dichroic coatings :(1) the front face coating is antireflective at laser

wavelength and reflective at a pump wavelength, and (2) the rear surface coating has the opposite properties. Collimated pump diode radiation is injected into the disk through the substrate and the heat exchanger, host material of the disk is doped with lasant ions so that a large fraction of the pump power is absorbed in two passes through the medium. Disk materials suitable for face-pumping include Nd:YAG, Nd:GGG, Nd:Glass, and Yb:S-FAP. Back face-pumped CAMIL is very conductive to integration into compact, self-contained modules. Front-injected CAMIL-FP operates in a similar way as the back-injected version, but it does not require a transparent heat exchanger.

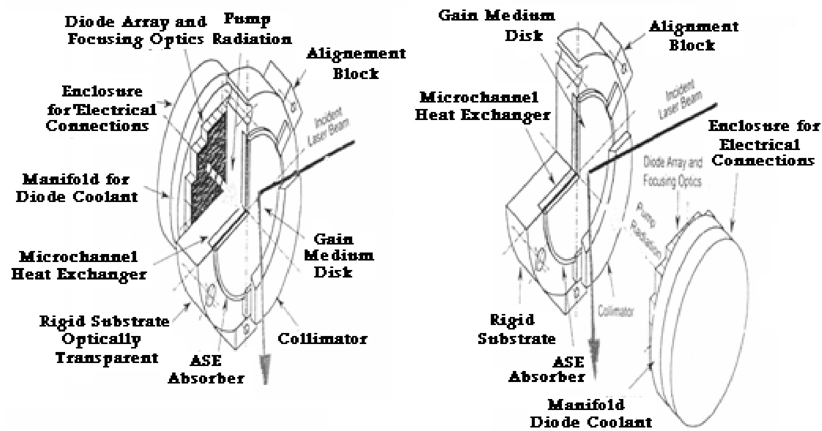

Fig.(1.20) (a) CAMIL module with back face pumping, (b) CAMIL module with front face pumping, [8].

1.4.3 Side Pumped CAMIL:

In situations where face pumping is impractical, injecting the pump radiation into the disk side (i.e., edge or perimeter) becomes an attractive alternative. Side pumping (SP) takes advantage of the long absorption path (approximately same dimension as disk diameter), which permits doping the disk with reduced concentration of lasant ions. This is of particular importance for some quasi-3 level lasants (e.g., Yb:YAG) where reduced doping can relax pump intensity required to overcome ground state absorption losses. Side-pumping also makes it possible to pump Nd^{+3} ion on the absorption line in the vicinity of 808nm, which has a significantly smaller absorption cross-section compared to the traditional 808nm absorption line. Apart from its attractive features, side-pumping also presents significant technical challenges including 1) delivering and concentrating pump radiation into the relatively small area around the disk perimeter, 2) preventing disk overheating in the areas where the pump radiation is injected, 3) generating uniform laser

gain over the disk aperture, and 4) mitigating depletion of laser gain by amplified spontaneous emission (ASE) and parasitic oscillations.

CAMIL-SP, shown in cross-section in Fig.(1.21a), uses composite disk formed by diffusion doping of undoped optical medium to the peripheral edges of a doped medium disk. This construction improves coupling between the pump diodes and the gain medium, aids concentration of pump radiation, draws heat away from disk edge, and helps to suppress parasitic oscillations providing a trap for ASE. Diode pump arrays are arranged around the circumference of the composite disk and point towards its centre. Placed between the diodes and the disk is a lensing element and a concentrator. The latter is a hollow conical "duct" with internal reflective surfaces and is analogous to linear ducts used for concentration of pump radiation in end-pumped lasers. For greater clarity, an exploded view of CAMIL-SP module is shown in Fig.(1.21b).

Pump radiation is first focused by the lensing element, followed by concentration in the conical "duct" and injection into the perimeter edge of the disk. Tapered portion of the undoped optical medium acts as a continuation of the concentrator because it further concentrates and channels pump radiation into doped portion of the disk. Aided by multiple internal reflections, pump radiation is channeled into and through the doped portion of the disk where it is gradually absorbed. The gain is doped so that large fraction (preferably >90%) of incident pump radiation is absorbed in a single pass through the disk.

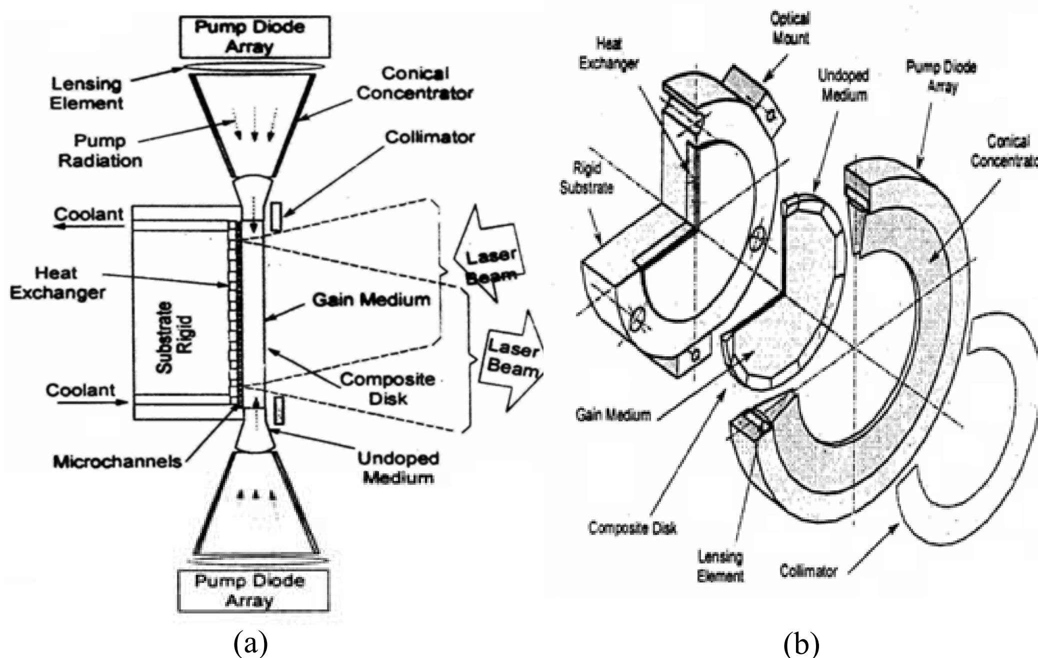

(a) (b)

Fig.(1.21) (a) Cross-section of side pumped CAMIL module, (b) side pumped CAMIL: cutway exploded view, [80].

1.5 Literature Survey:

This survey includes brief information about some bulk, QW diode lasers and some diode pumped solid-state lasers that are close to our field of study:

- In 1990, Yellen, tested strained-layer GRINSCH-SQW InGaAs uncoated lasers operating CW at 1.01 μm for 20000 h at 70 mW (per facet) at heat sink temperature of 30 ºC, [20].
- In 1991, Serreze, fabricated epitaxial wafers grown by metal organic chemical to obtain a high power, very low threshold, GaInP/AlGaInP strained-layer, single quantum well, GRINSCH heterostructure visible light (665 nm) laser. The threshold current densities for single element, uncoated, broad-area diodes operated CW as low as 425 A/cm^2, with output power of 340 mW per facet, and pulsed outputs (100 μs pulse width) of slightly under 1W per facet, with the lowest threshold current densities, and the highest output power values achieved up to date for visible diode laser, [10].
- In 1991, Laporta, achieved for the first time CW laser operation of bulk Er:Yb:Phosphate glass pumped at 980 nm by an InGaAs index-guided diode laser, with an output power of 2 mW at 1.54 μm, also they investigated the effects of pump wavelength by pumping the Er^{+3}:Yb^{+3} glass disk by a Ti:Al_2O_3 at 960 nm and 980 nm. They obtained high output power (70 mW) with the highest slope efficiency (21% for 980 nm pumping), [35].
- In1991, McCall, described and presented an initial experiment of a new microlaser design based on the high-reflectivity whispering-galley modes around the edge of a thin semiconductor microdisk, a threshold pump power below 100μm with a single-mode lasing at 1.3 and 1.5μm wavelengths were achieved when an InGaAs quantum wells pumped optically and cooled with liquid Nitrogen are used, [47].
- In 1993, Foing, et.al., demonstrated for the first time diode pumped Tm:$Ca_2Al_2Sio_7$ laser, an output power of 39 mW was achieved with an 8.6% slope efficiency at 11˚C, [38].
- In 1994, Levi, fabricated InGaAs/InGaAsP quantum well microdisk lasers 0.8μm in radius and 0.18 μm thick with emission at λ=1.542μm, which was operated at room temperature. He found that optical mode spacing in such structures is also large that

a significant fraction (~20%) of spontaneous emission resulting in a superlinear output over a wide pump range, [29].

- In 1995, Taira and Kobayashi, proposed a highly efficient and compact Nd:YVO_4 laser, in CW operation, a single- longitudinal mode output of 95 mW and a multi longitudinal mode output of 435 mW have been observed at 1.06μm with 1W diode laser, and a green output of 105 mW was generated using KTP crystal in the cavity, and a Q-switched pulse with a peak power of 230 mW and a pulse width of 8 ns was obtained, [42].
- In 1995, Khodr, et.al., studied the gain versus current- density relationship for IV-VI semiconductor quantum well lasers. They found that the nonparabolicity affects the gain versus current- density relation by reducing the current density needed for any given gain and increasing the gain saturation level and its effect on the threshold current decreases with increasing the cavity length, [24].
- In 1998, Park, et.al., investigated the effect of the well and the barrier thickness on InGaAsN/GaAs multiple quantum well (MQW) grown by (MOCVD). The results show that a red-shift in the PL wavelength is observed when the InGaAsN well thickness is increased up to 9.5 nm, and it was observed that the introduction of strain-compensated GaAsN layers can extend the emission wavelength, due to the reduction in the barrier potential, [25].
- In 1999, Klotzhin and Bhattucharya, has measured the dynamic and static characteristics of high- speed 1.55 and 1μm wavelength tunneling injection quantum- well lasers and 1μm wavelength self- organized quantum- dot lasers as a function of temperature, they showed that as the differential gain of the quantum-well increased with lowering the temperature, gain compression increased along with it. Also they showed that the modulation bandwidth of the quantum- dot lasers increased from 5-6 GHz at room temperature to larger than 20 GHz at 90 ˚K, [26].
- In 1999, Li, had built a novel diode- pumped Tm:YAG laser and investigated its output properties at different temperatures. They obtained 760 mW output power at wavelength of 2.013 μm when the incident power was 2.1 W in CW operation, with a slope efficiency of 44% and optical to optical slope efficiency reached 36%. When the system was Acousto-optic Q-switched they obtained an output pulses of 1.21 mJ, 380 ns (FWHM) with a repetition rate of 120 Hz, [36].

- In 1999, Chen, et.al., had built a high quality high efficiency $Nd:YVO_4$ end pumped by a 15 W diode laser bar. An optical to optical slope efficiency of 42% was obtained at an output of 3W with a beam quality factor of less than 1.2 with an output stability of ±0.5%. When an A.O. element was used, a pulse width of 25 ns at a repetition rate of 10 kHz with an output power of 0.98 W was achieved, [43].
- In 2000, Beffa, measured the optical modal gain of ridge- waveguide single-quantum well GRIN-SCH GaAs/AlGaAs diode lasers with an emission wavelength of 980 nm up to a temperature of 250 ˚C. They deduced that there is a linear dependence of the line shape function on temperature, [27].
- In 2000, Stewen, et.al., investigated the operation of diode pumping of Yb:YAG thin disk geometry, with thickness of 230µm, using V-shape technique, the output power obtained was found to be 647 W, with a slope efficiency of 51%, [30].
- In 2000, Howard, have successfully achieved "first laser light" from thin- disk laser, a 1.5 mm- thin Yb-YAG/YAG laser element thermally contacted with 4 µm of indium solder to a cooler was optically pumped by a laser diode array with a lens duct. He achieved a laser power of 260 W at low duty factor, [37].
- In 2001, H.H.Suhail, built an Intracavity SHG of diode laser end pumped $Nd:YVO_4$ laser. A 239 mW maximum power at 1064 nm was obtained at a pumping power of 800 mW at a TEM_{oo} mode operation which is achieved at a coupling factor of less than 2, [31].
- In 2002, Langrock, et.al., demonstrate the basic principle of pumping Nd:YAG rod with a length of 7.5 mm using an array of 810 nm, using L-shape cavity. The output power obtained was 150 mW, with a slope efficiency of 6.4%, [21].
- In 2002, Mukhopadhyay, et.al., had built an $Nd:GdVO_4$ microchip laser. The gain medium used was 2.5 mm thick 1.3at. % doped a-axis $Nd:GdVO_4$ crystal which was optically pumped with a diode- array coupled to a fiber that delivers a maximum output power of 15 W at 8.8 nm at the fiber bundle end in a bandwidth of 2 nm (FWHM). The power threshold was measured to be 186 mW, a maximum power of 1.2 W was achieved with an optical to optical slope efficiency of 22%, [39].
- In 2002, Mukhopadhyay, et.al., studied the effect of Nd^{+3} concentration on the CW and Q-switched laser performance at 1064µm from $Nd:YVO_4$ under diode laser

pumping. It was found that the 1 at.%- doped crystal is the best, offering the highest optical –to-optical conversion efficiency (55%), lowest fractional heat load (24%), highest pulse energy (80μJ) and shortest pulse width (20 ns), [41].

- In 2003, Wenzel, et.al presented the experimental results for tapered lasers emitting at 735 nm and 808 nm. Output power of 3W were achieved with nearly diffraction limited beams, tested consists from AlGaAs with zinc or carbon for p-doping for both the waveguide and the cladding layers. The quantum well consists of tensile-strained GaAsP with a thickness of 17 nm, with large differential gain with the absence of Al. The first 735 nm emitting device consists of $Al_{0.7}Ga_{0.3}As$ cladding layers and a 1μm thick $Al_{0.67}Ga_{0.35}As$ waveguide, while the 808 nm laser also consists of $Al_{0.7}Ga_{0.3}As$ cladding layers, but has a 2 μm thick $Al_{0.45}Ga_{0.55}As$ waveguide. The FWHM of the vertical far field intensity profiles is 27° with a slope efficiency of above 0.9 W/A for (732 nm) and 25° with a slope efficiency as high as 1.2W/A (808 nm), [80].
- In 2003, Vetrovec, developed solid-state laser for high-average power by placing the pump diode arrays around the perimeter of the disk so that the pump light is injected to the undoped edge. An output pulse energy of about 22 Joule was obtained by pumping 16 of 5 cm Nd:GGG disks in a double pass configuration with an input energy of 50 mJ, [40].
- In 2004, Park, et.al., investigated the well width dependence of the linewidth enhancement factor of (0001)-oriented wurtzite InGaN/GaN QW structure, they concluded that the linewidth enhancement factor rapidly decreases with increasing peak gain, for peak gain below 1000 cm^{-1}, while in QW structure with a thick well width has a larger linewidth enhancement factor than that with well width, [25].
- In 2005, Giesen, investigated the operation of thin disk laser principle using a Yb:YAG Disk medium with a diameter of several mm, and thickness of (100-200)μm, using V-shape technique. The maximum output power was 500 W, with a slope efficiency of 55%, [9].
- In 2007, Al-Ani, reported diode pumped-laser of $Nd:YVO_4$ disk medium of (4*5*1)mm using a 808 nm CW bulk diode laser. The output power obtained was 600 mW at a pumping power of 1500 mW, with a slope efficiency of 56%, [32].

- In 2007, Tsvid, et.al., determined the gain, spontaneous emission spectra, and radiative efficiency of InGaAs quantum well laser structures, considering the relationship between injection efficiency and radiative efficiency, [23].
- In 2007, Khoon Ee, et.al., presented a novel approach to improve the light extraction efficiency of InGaN quantum wells light emitting diodes (LEDs) using SiO2 microspheres, leading to ~232% increase of the LEDs output power, [28].
- In 2008, Adolfsson, et.al., present an experimental and theoretical investigation of the temperature dependence of the threshold current for double quantum well GaInNAs–GaAs lasers in the temperature range 10 C–110 C. Pulsed measurements of the threshold current have been performed on broad and narrow ridge waveguide (RWG) lasers. The narrow RWG lasers exhibit high characteristic temperatures T_o of 200 K up to a critical temperature T_c, above which T_o is reduced by approximately a factor of 2. Numerical simulations, with a good agreement with experimental data reveal that a weakly temperature dependent lateral diffusion current dominates the threshold current for narrow RWG lasers, [22].
- In 2008, Khoon Ee, et.al, presented optimization studies of InGaN quantum wells light emitting diodes employing SiO_2 / polystyrene microlens arrays. The studies show that the use of microlens arrays leads to increase in light extraction efficiency by 2.7-times, in agreement with simulation, [33].

1.6 Aim of the work:

The aim of this study is to built a mathematical model to investigate the performance of quantum well lasers, which can be hired in pumping solid-state disc used in solid-state lasers having the highest optical efficiency, peak output power, and ultra high beam optical quality, and comparing it with bulk diode lasers.

The experimental part uses the bulk (in pulsed and CW mode) and QW (in CW mode) laser as a pumping source for $Nd{:}YVO_4$ medium in two different pumping schemes: the direct face-pumping, the V-shape face-pumping. As a unique implementation in Iraq, a QW laser source was used as a pumping source for the Disk medium.

1.7 Thesis layout:

Chapter one provides an introduction and literature survey about QW lasers and diode pumping.

Chapter two presents the theoretical concepts about the density of states of both the bulk and QW lasers besides the dynamics. Furthermore the concept of diode pumping techniques, especially conversion of the input to output energy.

Chapter three deals with the proposal of GaAs/AlGaAs QW structure with GaAs as the active region and AlGaAs as the barrier, in which the Al mole fraction was chosen to be equal to 0.35, with varying the thickness of the active region.

Chapter four examined the experimental work which includes the setup and performance of diode pumped disk laser using bulk and QW sources in different modes (CW, pulsed) with two different pumping schemes.

Chapter five consists of two parts: the first part includes the analytical and solution of some problems in bulk and QW (GaAs/AlGaAs) structures, and the differences between both structures, while the second part illustrates the result of the experimental work that are divided into two parts, first part shows the performance of direct face pumping of Nd:YVO_4 disc medium using 808 nm bulk diode laser internally and externally triggered, while second part shows the performance of face pumping using V-shape configuration of the Nd:YVO_4 disk medium using 810nm QW GaAlAs in CW mode in comparison to 808 nm bulk diode laser, operating once in CW mode and in pulsed mode (internally and externally triggered).

Chapter six presents conclusions of the work in addition to the suggested future work.

List of Symbols and Abbreviations:

[illegible]

AMA	Active Mirror Amplifier
ASE	Amplified Spontaneous Emission
BS	Beam Splitter
DBR	Distributed Bragg Reflector
DFB	Distributed Feedback
BQ	Beam Quality
CAMIL	Compact Active MIrror Laser
DH	Double Heterostructure
DPSSL	Diode Pumped Solid State Laser
FFP	Far Field Pattern
FP	Face Pumped
FWHM	Full Width Half Maximum
GRISCH	GRaded Index Separate Confinement Heterostructure
HAP	High Average Power
ILDs	Injection Laser Diodes
LD	Laser Diode
MOCVD	Metal Organic Chemical Vapor Decomposition
MQW	Multiple Quantum Well
NFP	Near Field Pattern
PRF	Pulse Repetition Frequency
QW	Quantum Well
ROC	Radius of Curvature
SLD	Superluminescent diode
SP	Side Pumped
SQW	Single Quantum Well
SSL	Solid State Laser
TE	Transverse Electric
TEC	Thermo Electric Cooler
TM	Transverse Magnetic
VCSEL	Vertical Cavity SEmiconductor Laser

[illegible]

A	Cross Section of the Laser Medium
A_{ij}	Anisotropy Factor for Transition i, j
C_{ij}	Spatial Overlap Factor between States i and j
c_o	Vacuum Speed of Light
C_p	Specified Heat Capacitance of the Active Region
d	Thickness of the Active Region for Bulk Laser
$dn/d\lambda$	Material Dispersion
E_F	Fermi Energy
E_g	Direct Bandgap

E_{ij} Transition Energy between States i and j
En Energy of Subband n
En,p Confinement Energies for the Electrons (e) and Holes (p)
E_o Energygap Constant
f_c Fermi population factor for conduction electrons
f_v Fermi population factor for valence holes
g(E) Spectrally Dependent Gain Coefficient
H Heaviside step function
$h\upsilon_{L,p}$ Photon Energy Emitted at the Laser Transition, and Pump Photon Photon, Respectively
i,j Conduction, Valence Quantum Numbers (at Γ)
k Electron's Vector
k_z Thermal Conductivity of the Active Region
L Cavity Length
L_b Barrier Thickness
Lz Layer Thickness, of the QW
$|M|^2$ Bulk Momentum Transition Matrix Element
m_c Effective Mass of the Electron at the Bottom of the Conduction Band
m_r Reduced Mass
m_v Effective Mass of the Electron at the Top of the Valence Band
n Refractive Index of the Material
$n_{1,2}$ Refractive Index of the Active Layer and the Cladding
N_W No. of Wells
N_{QW} Refractive Index of the MQW Layer
P Usual Quantum Mechanical Linear Momentum Operator
P_e Power Emitted by Stimulated Emission
P_o Output Power
P_{th} Threshold Power
q Charge of the Electron
r Reflectivity of the Output Coupler
R Reflection Loss
R_d Series Resistance of the Diode due to the Resistivity of the Epilayers and Resisitivity of the Metal Contacts
R(E) Radiative Component of Carrier Recombination
s Stripe Width
t_p Pulse Duration
T Temperature
$\check{T}$ Kinetic Energy Operator
T_{hs} Temperature of the Heat Sink
T_1 Transmission of the Output Coupler T_1=1-R
T_2 Collision Time
V_o Applied Forward Voltage for Diode Laser
V(x,y,z) Potential Energy of the System as a Function of the Spatial Coordinates
VP Void Area Percentage
x Al mole Fraction
Δ_{s-o} Split-off Band Separation
ΔE Bandgap of the Recombination Region

$\Delta E_{c,v}$	**Bandgap Discontinuity of the Conduction and Valence Bands**
Γ_a	**Fraction of the Mode Power Carried within the Active GaAs Layer**
$\Gamma_{n,p}$	**Fraction of the Power in the n and p Regions, respectively**
ψ	**Describes the State of the System**
α_n	**Loss Constant of the Unpumped n-$Ga_{1-x}Al_xAs$**
α_p	**Loss (by free holes) in the Bonding p-$Ga_{1-x}Al_xAs$ Region**
α_o	**Absorption Coefficient of the Laser Crystal**
γ	**Gain Constant**
ε_o	**Free-Space Permittivity**
η	**Efficiency of the Laser in Converting the Electrical Power Input to Optical Power**
η_a	**Absorption Efficiency**
η_B	**Beam Overlap Efficiency**
η_d	**Differential Quantum Efficiency Characterized by the Number of Photons Emitted per Injected Electrons**
η_E	**Extraction Efficiency**
η_{ex}	**External Differential Quantum Efficiency**
η_i	**Probability that an Injected Carrier Recombine Radiatively within the Active Region**
η_o	**Overall Efficiency**
η_p	**Pump Efficiency**
η_Q	**Quantum Efficiency**
η_S	**Stokes Factor**
η_t	**Radiation Transfer Efficiency**
$\lambda_{p,L}$	**Wavelength of the Pump Transition and the Laser Wavelength respectively**
ρ	**Mass Density**
σ	**Stimulated Emission Cross Section**
σ_s	**Slope Efficiency**
τ_f	**Florescence Lifetime**

Refrences:

1. **W.W.Chow, *"Semiconductor Laser Fundamentals"*, Springer-Verlag Berlin Heidelberg, 1999.**
2. **D. M.Kane, and K.Alan Shore, *"Introduction"*, John Wiley&Sons,Ltd, 2005.**
3. **A. Yariv, *"Optical Communication in Modern Communication"*, Oxford university Press, 1997.**
4. **I.Stateikina, *"Optoelectronic Semiconductor Devices Principals and Characteristics",* Course in ENGR-797, 2002.**
5. **D. J. Blumenthal, *"Semiconductors"*, Hanyang University, 2006.**
6. **P. S.Zory, *"Quantum Well Lasers"*, Academy Press, 1993.**
7. **A. Yariv, *"Quantum Electronics"*, John Wiley&Sons, 1989.**
8. **Ing. Dickmann, *"Diode Pumped Solid State Lasers"*, 2006.**
9. **A.Giesen, *"Thin Disk Lasers Power Scalability and Beam Quality"*, LTJ, Vol.42, No. 2, June 2005.**
10. **H.B.Serreze, and Y.C.Chen, *"Low-Threshold, Strained-Layer GaInP/AlGaInP* GRINSCH Visible Diode Lasers", IEEE Photonics Technology Letters, Vol.3, No.5, pp.397-399, May 1991.**
11. **B.E. A. Saleh, and M.Carl Teich, "Fundamentals of photonics", John Wiley&Sons, 1991.**
12. **"Lectures on Ultra Short Laser Technology and Applications".**
13. **R.Kimball, M.W.Dowley, and J.L.Arcus, *"Diode Lasers Their Characteristics and Control"*, SPIE, Vol.740, pp.41-46, laser diode optics 1987.**
14. **C.S.Wang, *"The Structure and C/Cs of Laser Diodes for Optical Instruments*", SPIE, Vol.741, pp.52-64, design of optical systems incorporating low power lasers (1987).**
15. ***"Laser and Applications"*, unit 10 semiconductor diode lasers, Internet Source.**
16. ***"Laser Source"*, Internet Source.**
17. **O.Svelto, *"Principles of Lasers"*, Plenum Press, New York, 1998.**
18. ***"Laser Diode Guide",* Sony Semiconductors, 2000 Sony Corporation.**
19. **T.Y.Fan, and R.L.Byer, *"Diode Laser-Pumped Solid State Lasers"*, IEEE Journal of Quantum Electronics, Vol.QE. 24, No. 6, pp.895-912, June 1988.**

20. **S.L.Yellen,R.G.Waters, Y.C.Chen, B.A.Boltz, S.E.Fischer, D.Fekete, and J.M.Ballantyne, *"20,000h InGaAs Quantum Well Lasers"*, Electronics Letters, Vol.26, No.25, pp.2083-2084, December 1990.**
21. **C. Langrock, D.Hum, E.Diamanti, M.Charbonneau, S.Wong, A.Bullington, S.Koseki, M.Wiemer, K.Braden, H.Altug, S.Bank, V.Lordi, C.Barnes, B.Cowan, P.Lu, K.Wang, G.Risk, S.Kim, J.Chuang, X.Xie, W.Zhao, K.Yu, A.Ozcan, J.Wisdom, S.kim, and A.Kahili, *"Laser Diode CW Pumped Nd:YAG Lasers"*, IEEE, Journal of Selected Topics in Quantum Electronics, Vol.37, No.3, pp.101-103, March 2002.**
22. **G. Adolfsson, S. Wang, M.Sadeghi, J. Bengtsson, A. Larsson, J. Lim, V. Vilokkinen, and P.Melanen, *"Effects of Lateral Diffusion on the Temperature Sensitivity of the Threshold Current for 1.3µm Double Quantum-Well GaInNAs–GaAs Lasers"*, IEEE Journal of Quantum Electronics, Vol. 44, No. 7, pp.607-616, July 2008.**
23. **G. Tsvid, J. Kirch, L. J. Mawst, M. Kanskar, J. Cai, R. A. Arif, N. Tansu, P. M. Smowton, and P. Blood, *"Radiative Efficiency of InGaAs/InGaAsP/GaAs Quantum Well Lasers"*, IEEE Journal of Quantum Electronics, Vol. 10, No.7, pp.313-314, 2007.**
24. **M.E. Khodr, and P.J.McCann, *"Gain and Current Density Calculation in IV-VI Quantum Well Laser"*, J. Appl. Phys. Vol.77, No.(10), pp.4927-4930, May 1995.**
25. **S. H. Park, J.Kim, and H.Kim, *"Well- Width Dependence of the Linewidth Enhancement Factor of Wurtzite InGaN/GaN Quantum- Well Lasers"*, Vol.44, No.6, pp.1560-1564, June 2004.**
26. **D. Klotzkin, and P. Bhattacharya, *"Temperature Dependence of Dynamic and Dc Characteristics of Quantum- Well Quantum- Dot Lasers: A Comparative Study"*, Journal of Lightwave Technology, Vol. 17, No.9, pp.1634-1642, September 1999.**
27. **F. Beffa, K.Jackel, M.Achtenhagen, and C.Harder, *"High-Temperature Optical Gain of 980 nm InGaAs/AlGaAs Quantum-Well Lasers"*et.al., Appl. Phys. Lett., Vol.77, No.15, pp.2301-2303, October 2000.**
28. ***Y.Khoon Ee , P. Kumnorkaew , R. A. Arif , J. F. Gilchrist and N.Tansu," Enhancement of Light Extraction Efficiency of InGaN Quantum***

Wells LEDs Using SiO2 Microspheres", Optical Society of America, pp.1-2, 2007.

29. A.F,Levi., *"Microdisk Lasers"*, Solid State Electronics, Vol.37, pp1297-1302, 1994.
30. C. Stewen, K.Contag, M.Larionov, A.Giesen, H.Hugel, *"A 1-kW CW Thin Disc Lasers"*, IEEE, Journal of Selected Topics in Quantum Electronics, Vol.6, No.4, pp.650-657, July/August 2000.
31. H.H.Suhail, *"Intracavity Second Harmonic Generation of Diode Laser End Pumped Nd:YVO_4 Crystal"*, Ph.D. Thesis, Military College of Engineering, Iraq, 2000.
32. M.K.Al-Ani, *"Performance Study of Diode Pumped Solid State Disc Lasers"*, Ph.D. Thesis, University of Technology, Iraq, 2007.
33. *Y.Khoon Ee , P. Kumnorkaew , R. A. Arif , J. F. Gilchrist and N.Tansu," Size Effects and Light Extraction Efficiency Optimization of III-Nitride Light Emitting Diodes with SiO_2 / Polystyrene Microlens Array"*, Optical Society of America, pp.1-3, 2008.
34. M. Oka, and S. Kubota, *"Stable Intracavity Doubling of Orthogonal Linearly Polarized Modes in Diode-Pumped Nd:YAG Lasers"*, Optics Letters, Vol.13, No.10, pp.895-897, October 1999.
35. P.Laporta, S.De Silvestri, V.Magni, and O.Svelto, *"Diode-Pumped CW Bulk Er:YB:Glass Laser"*, Optics Letters, Vol.16, No.24, December 1991.
36. C. Li, J.Song, D.Shen, N.Seong, and K.Uda, *"Diode-Pumped High-Efficiency Tm:YAG Lasers"*, Optics Express, Vol.4, No.1, 1999.
37. H.T.Powell, and L.Zapata, *"First Light Generated From Yb:YAG/YAG Composite Thin Disk Laser"*, Laser Science and Technology, June 2000.
38. J.P.Foing, E.Scheer, B.Viana, and N.Britos, *"Diode Pumped Emission of Tm^{+3} Doped $Ca_2Al_2SiO_7$ Crystals"*, Arcueil Cedex France, 1993.
39. P. K.Mukhopadhyay, K.Rangansthan, J.George, S.K.Sharma, and T.P.S.Nathan, *"Effect of Absorbed Pump Power on the Quality of Output Beam From Monolithic Microchip Lasers"*, Indian Academy of Science, Vol. 58, No.4, pp.657-668, April 2002.
40. J. Vetrovec, A.Koumvakalis, R.Shah, and T.Endo, *"Development of Solid-State*

Disk Laser for High-Average Power", SPIE LASE , pp.26-31, January 2003.

41. P. K. Mukhopadhayay, K.Rangansthan, J.George, S.K.Sharma, and T.P.S.Nathan, *"Effect of Nd^{+3} Concentrations on CW and Pulsed Performance of Fiber-Coupled Diode Laser Pumped Nd:YVO_4 Laser at 1064 nm"*, Indian Academy of Science, Vol.59 No.1, pp.75-89, July 2002.
42. T. Taira, and T. Kobayashi, *"Intracavity Frequency Doubling and Q-Switching in Diode- Laser Pumped Nd:YVO_4 Lasers"*, Applied Optics, Vol.34, No.21, pp.4298-4301, July 1995.
43. Y. Chen, Z.Xiong, G.Lim, H.Zheng, and X.Peng, *"High-Efficiency Nd:YVO_4 Laser End-Pumped with a Diode Laser Bar"*, Sintec Optronics Pte Ltd, Singaporee, 1999.
44. S.H.Park, *"Barrier-Height Effects on Lasing Characteristics of InGaAs/InGaAlAs Strained Quantum Well Lasers"*, Journal of the Korean Society, Vol.32, No.5, pp.713-717, May 1998.
45. S.L.McCall, A. F. J. Levi, R. E. Slusher, S. J. Pearton, and R. A.*"Whispering-Gallery Mode Microdisk Lasers",* Applied Physics Lett. Vol.60, No.(3), January 1992.
46. K.Srinivasan, K.Srinivasan, M.Borselli, T.J.Johnson, P.E.Barclay, and O.Painter,A.Stintz and S.Krishna, *"Optical Loss and Lasing Characteristics of High-Quality-Factor AlGaAs Microdisk Resonators with Embedded Quantum Dots"*, Applied Physics Letters, Vol.86, pp.1-3, April 2005.
47. Data Sheet SLD323V, Sony, *"High Power 1W Laser Diode"*.
48. Y.Arakawa, and H.Sakaki, *"Multidimensional Quantum Well Laser and Temperature Dependence of its Threshold Current"*, Appl.Phys.Lett, Vol.40, pp.939-941, June 1982.
49. S. R. Chinn, P.S.Zory, A.R.Reisinger, *"A Model for GRIN-SCH-SQW Diode Laser"*, IEEE Journal of Quantum Electronics, Vol. 24, No.11, pp.2191-2214, November 1988.
50. Data Sheet, *"Laser Diode Driver and TEC Controller"*, Alphalas, Germany.
51. S. Blaaberg, P.Petersen, and B.Tromborg, *"Structure, Stability, and Spectra of Lateral Modes of a Broad-Area Semiconductor Laser"*, IEEE Journal of Quantum Electronics, Vol.43, No.11, pp.959-973, November 2007.

52. Y.Arakawa, and A.Yariv, *"Theory of Gain, Modulation Response, and Spectral Linewidth in ALGaAs Quantum Well Lasers"*, IEEE Journal of Quantum Electronics, Vol.QE-21, No.10, pp.1666-1647, October 1985.
53. A.Kurobe, H.Furuyama, S.Naritsuka, N.Sugiyama, Y.Kokubun, and M.Nakamura, *"Effects of Well Number, Cavity Length, and Facet Reflectivity on the Reduction of Threshold Currrent of GaAs/AlGaAs Multiquantum Well Lasers"*, IEEE Journal of Quantum Electronics, Vol. QE-24, No.4, pp.635-640, April 1988.
54. D. S. Gao, M.Kang, R.P.Bryan, and J.J. Coleman,*"Modeling of Quantum- Well Lasers for Computer -Aided Analysis of Optoelctronics Integrated Circuits"*, IEEE Journal of Quantum Electronics, Vol. 26, No. 7, pp.1206-1216, July 1990.
55. L.F. Feng, C.D.Wang, H.X.Cong, C.Y.Zhu, J.Wang, X.S.Xie, C.Z.Lu, and G.Y.Zhang, *"Sudden Change of Electrical Characteristics at Lasing Threshold of a Semiconductor Laser"*, IEEE Journal of Quantum Electronics, Vol. 43, No.6, pp.458-461, June 2007.
56. S.P. Cheng, F.Brillout, and P.Correc,*"Design of Quantum Well AlGaAs-GaAs Stripe Lasers for Minimization of Threshold Current-Application to Ridge Structures"*, IEEE Journal of Electronics, Vol.24, No. 12, pp.2433-2440, December 1988.
57. J. Piprek, P.Abraham, and J.E.Bowers, *"Cavity Length Effects on Internal Loss and Quantum Efficiency of Multiquantum- Well Lasers"*, IEEE Journal of Quantum Electronics, Vol. 5, No.3, pp.643-647, May/June 1999.
58. W.A .Paul, MC Ilory, A.Kurobe, Y.Uematsu, *"Analysis and Application of Theoretical Gain Curves to the Design of Multi-Quantum- Well Lasers"*, IEEE Journal of Quantum Electronics, Vol.QE-21, No.12, pp.1958-1963, December 1985.
59. A. Sugimura, *"Threshold Currents for AlGaAs Quantum Well Lasers"*, IEEE Journal of Quantum Electronics, Vol.QE-20, No.4, pp.336-343, April 1984.
60. S.Weisser, I.Esquivias, P.J.Tasker, J.D.Ralston, B.Romero, J.Rosenzweig, *"Impedance Characteristics of Quantum –Well Lasers"*, IEEE Photonics

Technology Letters, Vol.6, No., 12, pp.1421-1423, December 1994.

61. Laser Diodes, Internet Source.

62. B. Saint-Crico, F.Lozes-Dupuy, and G.Vassilieff, *"Well Depth Dependence of Gain and Threshold Current in GaAlAs Single Quantum Well Lasers"*, IEEE Journal of Quantum Electronics, Vol. QE-22, No.5, pp.625-630, May 1986.

63. P.A. Chen, C.Juang, and Y.Chang, *"Carrier-Induced Energy shift in GaAs/AlGaAs Multiple Quantum Well Laser Diodes"*, IEEE Journal of Quantum Electronics, Vol.29, No.10, pp.2607-2618, October 1993.

64. J.M.Pikal, C.S.Menoni, H.Temkin, P.Thiagarajan, and G.Y.Robinson, *"Carrier Lifetime and Recombination in Long-Wavelength Quantum-Well Lasers"*, IEEE Journal of Selected Topics in Quantum Electronics, Vol. 5, No.3, pp.613-619, May/June 1999.

65. T. Tsukada, and Y. Shima, *"Thermal Characteristics of Buried-Hetrostructure Injection Lasers"*, IEEE Journal of Quantum Electronics, Vol.QE-11, No.7, pp.494-498, July 1975.

66. W.P.Dumke, *"The Angular Beam Divergence in Double-Heterojunction Lasers With Very Thin active Regions"*, IEEE Journal of Quantum Electronics, Vol.QE-11, No.7, pp. 400-402, July 1975.

67. R. Muller, *"A Theoretical Study of the Dynamical Behavior of Single Quantum-Well Semiconductor Lasers"*, Vol.91, Optics Communication, pp.453-464, 1992.

68. E.Zielinski, H.Schweizer, S.Hsusser, R.Stuber, M.H.Pilkuhn, and G.Weimann, *"Systematics of Laser Operation in GaAs/AlGaAs Multiple Well Heterostructures"*, IEEE Journal of Quantum Electronics, Vol.QE-23, No.6, pp.969-975, June 1987.

69. D.Kasemset, C.Hong, N.B.Patel, and P.D.Dapkus, *"Graded Barrier Single Quantum Well Lasers-Theory and Experiment"*, IEEE Journal of Quantum Electronics, Vol. QE-19, No. 6, pp.1025-1030, 1983.

70. Y.Arakawa, and A.Yariv, *"Quantum Well Lasers- Gain, Spectra, Dynamics,* IEEE Journal of Quantum Electronics, Vol. QE-22, No.9, pp.1887-1899, September 1986.

71. W. Koechner, *"Solid-State Laser Engineering"*, Springer 1999.

72. **G.H.B.Thompson,** ***"Physics of Semiconductor Laser Devices"*****,** **John Wiley&Sons, 1980.**

73. **P. Weetman,** ***"Modeling Quantum Well Lasers"*****, Ph.D. Thesis, Waterloo, Ontario, Canada, 2002.**

74. **Paul Harrison,** ***"Quantum Wells, Wires, and Dots"*****, John Wiley and Sons, LTD, 2004.**

75. **W. Koechner,** ***"Solid-State Laser Engineering"*****, Springer 2006.**

76. **G.W. Taylor,** ***"A New Theoretical Approach for the Quantum Well Semiconductor Laser"*****, Prog. Quant. Electr. Vol.16, 1992.**

77. **M. Diom, Z.M.Li, R.F.Chatenoud, R.L.Williams, and S.Dick,** ***"A Study of the Temperature Sensitivity of GaAs-(Al,Ga)As Multiple Quantum-Well GRINSCH Lasers"*****, IEEE, Journal of Selected Topics in Quantum Electronics, Vol.1, No.2, pp.230-233, June 1995.**

78. **F.Gity, V.Ahmadi, M.Noshiravani,** ***"Numerical Analysis of Void-Induced Thermal effects on*** $GaAs/Al_xGa_{1-x}As$ ***High Power Single-Quantum-Well Laser Diodes"*****, Solid-State Electronics, Vol.50, pp.1767-1773, 2006.**

79. ***R.Ifflander, "Solid-State Lasers for Material Processing", Springer Series, 2001.***

80. **H.Wenzel,** ***B.Sumpf, G.Erbert, "High-Brightness Diode Lasers"*****, C.S.Physique, Vol.3, pp.649-661, 2003.**